RECONSTRUCTION OF THREE-DIMENSIONAL FLUX SHAPES FROM NODAL SOLUTIONS

by

José Félix Pérez Méndez-Castrillón

Ingeniero de Minas

Escuela Técnica Superior de Ingenieros
de Minas de Oviedo, Spain
(1981)

Submitted to the Department of
Nuclear Engineering
in Partial Fulfillment of the
Requirements for the
Degree of

NUCLEAR ENGINEER

and

MASTER OF SCIENCE

at the

MASSACHUSETTS INSTITUTE OF TECHNOLOGY

June, 1984

Signature of Author _____
Department of Nuclear Engineering
May, 1984

Certified by _____
Professor Allan F. Henry
Thesis Supervisor

Accepted by _____
Professor Allan F. Henry, Chairman
Departmental Graduate Committee
Department of Nuclear Engineering

RECONSTRUCTION OF THREE-DIMENSIONAL FLUX SHAPES FROM NODAL SOLUTIONS

by

José Félix Pérez Méndez-Castrillón

Submitted to the Department of Nuclear Engineering on May 11, 1984 in partial fulfillment of the requirements for the degrees of Nuclear Engineer and Master of Science.

ABSTRACT

The objective of this research is to develop an accurate and computationally efficient method (the Three-Dimensional Form Function Method) for reconstructing, from a nodal solution, the fine-mesh point flux and point power distribution for two- and three-dimensional reactor geometries.

The basic approximation of the Three-Dimensional Form Function Method is that within any reactor node, the reconstructed flux can be expressed as the product of a two-dimensional assembly function, which reflects the heterogeneous detailed geometry of the reactor, and a tri-quadratic polynomial function.

The assembly function is obtained from fine-mesh PDQ-7 color set calculations. The tri-quadratic polynomial function is chosen in such a way that the reconstructed flux reproduces the node-averaged fluxes from the nodal solution, and the reconstructed flux satisfies the multigroup neutron diffusion finite difference equations about node corner points, and, in an integral sense, along node lines.

Analysis of two- and three-dimensional benchmark PWR problems demonstrates that very accurate local fluxes can be obtained, especially for interior points (4 cm or more distant from the reactor axial surfaces), where the pointwise average power is determined with a maximum error (relative to a fine-mesh PDQ-7 calculation) of approximately two percent for points in the unrodded area and four percent for points in the rodded area. The computational efficiency of the Three-Dimensional Form Function Method is also shown to be about two orders of magnitude greater than for finite difference methods.

Thesis Supervisor: Allan F. Henry

Title: Professor of Nuclear Engineering

ACKNOWLEDGMENTS

The author would like to thank his thesis supervisor, Professor Allan F. Henry, for his invaluable assistance and support during the course of this investigation. His unflagging interest and willingness to argue and listen are deeply appreciated.

Thanks are also due to Professor Kent F. Hansen for serving as a reader for this thesis.

The author is also indebted to Mrs. Rachel Norton for her consulting help with certain programming techniques.

Grateful recognition is also extended to Dr. Donald Parsons for his help with CMS and QUANDRY. Additionally, the author would like to thank Northeast Utilities for the use of their computing facilities in obtaining several PDQ-7 reference solutions.

The author wishes to thank Mrs. Mary Bosco for her assistance in the preparation of this document. Her technical and highly professional skills are clearly demonstrated in this manuscript.

Finally, the author would like to thank all the Institutions that provided financial support during the course of this investigation. In particular, the author wishes to acknowledge the U.S.-Spanish Joint Committee for Cultural and Educational Affairs for their generous financial assistance.

TABLE OF CONTENTS

Page

LIST OF FIGURES

LIST OF TABLES

Chapter 1

INTRODUCTION

1.1 OVERVIEW

Finite difference methods are commonly used as a standard computational technique for calculation of the spatial power distribution required for the design and analysis of light water reactors. However, even with present-day high speed digital computers, finite difference methods are not capable of performing efficiently three-dimensional calculations for large water reactors. To this day, three-dimensional finite difference transient calculations remain prohibitively expensive and, thus, impractical for the routine analysis of thermal reactors.

In recent years, more sophisticated theoretical methods have been developed. In particular, nodal methods such as the Analytical Nodal Method incorporated in the computer code QUANDRY[1] and the nodal equivalence theory devised by Koebke[2] and later modified by Smith,[3] have been demonstrated to be at least two orders of magnitude more computationally efficient than finite difference schemes.[1] The computational efficiency of the nodal methods is a direct consequence of the large reduction in the number of unknowns that results when these unknowns are taken to be averaged quantities over relatively large nodal regions.

In many reactor calculations, global quantities such as k_{eff} and averaged assembly powers are of primary importance. In such a case, nodal methods become more attractive than finite difference methods.

However, several reactor studies, such as the determination of power peaking factors or thermal-hydraulic analysis of the hottest channels in an assembly, require the knowledge of detailed pin-cell powers. Nodal methods cannot be directly and efficiently applied to calculate this detailed information. Several methods to reconstruct, from nodal solutions, the fine-mesh flux and power, have been developed by Hoxie,[4] Finck[5] and Khalil.[6] However, all these methods are limited to two-dimensional reactor geometries.

The objective of this investigation is to develop an accurate and computationally efficient method to reconstruct, from a nodal solution, the fine-mesh point flux and point power distribution for two- and three-dimensional reactor geometries. In particular, these techniques will be tested in several benchmark PWR problems.

1.2 GLOBAL REACTOR ANALYSIS

The Boltzmann transport equation, a partial differential equation for the directional neutron flux density, governs the neutron population behavior inside nuclear reactors. Unfortunately, for realistic reactor configurations, an exact solution of the transport equation is prohibitively expensive, and thus, approximate methods, derived from the transport equation, have to be used. For light water reactors, the most widely used of these approximate methods is multigroup neutron diffusion theory. For this model, the static multigroup neutron diffusion equation, when cast in conventional matrix notation, can be written as:

$$- \underline{\nabla} \cdot [D(\underline{r})] \, \underline{\nabla} \cdot [\phi(\underline{r})] + [M(\underline{r})][\phi(\underline{r})] = 0 \qquad (1\text{-}1)$$

where

$$[M(\underline{r})] \equiv [\Sigma_T(\underline{r})] - \frac{1}{\lambda}[\chi][\nu\Sigma_f(\underline{r})]^T$$

and

$[\phi(\underline{r})]$ is a column vector of length the number of neutron groups, G, containing the neutron fluxes.

$[D(\underline{r})]$ is a diagonal $G \times G$ matrix containing the diffusion coefficients.

$[\Sigma_T(\underline{r})]$ is a $G \times G$ matrix containing the macroscopic total minus-scattering cross section.

$[\chi]$ is a column vector of length G containing the fission neutron spectrum.

$[\nu\Sigma_f(\underline{r})]$ is a column vector of length G containing the average number of neutrons, ν, emitted per fission times the macroscopic fission cross section, $\Sigma_f(\underline{r})$.

λ is the eigenvalue of the global static reactor problem.

In Ref. 7, the derivation of this equation from the transport equation is presented.

In this section, two schemes for solving the multigroup diffusion equation, Eq. 1-1, are briefly described. The first scheme is a finite difference method, and the second, a nodal method.

1.2.1 Finite Difference Methods

The corner-point-centered finite difference method, as incorporated into the PDQ-7[9] computer code, is commonly used to solve the multigroup diffusion equation, Eq. 1-1. In order to apply this method, it is first required to divide the reactor spatial domain into small mesh volumes,

called mesh cells. The diffusion equation, Eq. 1-1, is then integrated over each mesh cell. When applying this balance condition, it is assumed that the flux has a constant (average) value over each mesh cell, and that the partial derivatives at the mesh cell faces can be evaluated by the centered finite difference approximation. The application of this balance condition at every reactor mesh cell yields a system of coupled linear algebraic equations where the unknowns are the mesh cell averaged fluxes. The spatial coupling, for three-dimensional geometries, is to seven points. This system of equations can be solved by an iterative scheme in a digital computer. For a realistic three-dimensional reactor calculation, the number of mesh cells (i.e., the number of equations) can easily exceed one million. Even with present-day high speed computing machines, three-dimensional finite difference calculations are prohibitively expensive.

1.2.2 Nodal Methods

Nodal methods are another alternative to solve the multigroup neutron diffusion equation, Eq. 1-1. In order to derive the nodal equations, it is first necessary to partition the reactor spatial domain into relatively large rectangular right parallelepipeds, called nodes. Homogenized cross sections (usually flux weighted cross sections) must be found for each node by performing a series of local fine-mesh calculations. The multigroup diffusion equation, Eq. 1-1, is then integrated over each node volume. The unknowns of the resulting equation are the node volume averaged flux and node face averaged net currents. In order to solve this equation, an additional relationship between the node volume averaged flux and the node face averaged currents must be found. In the Analytical Nodal Method,

incorporated into the computer code QUANDRY,[1,3] such a relationship is determined, for a two-group model, by solving analytically, for each node and each direction, the differential equation which results when the diffusion equation, Eq. 1-1, is integrated over the other two transverse directions. In order to solve this coupling equation, the transverse leakage shape is approximated by a quadratic polynomial. A full derivation of the nodal and coupling equations used in the Analytical Nodal Method is presented in Ref. 1. The calculation of homogenized cross sections and discontinuity factors, input data for the QUANDRY code, is explained in Ref. 3.

The node volume-averaged fluxes and node face-averaged fluxes, which are the most detailed information output directly from QUANDRY, will be used, in the present investigation, for calculating the fine-mesh flux and fine-mesh power.

1.3 FLUX RECONSTRUCTION METHODS

In order to enlarge the scope of the nodal schemes, there are strong incentives to develop computationally efficient methods to calculate fine-mesh point fluxes from a global nodal solution.

One of the most successful flux reconstruction schemes for the analysis of two-dimensional PWR problems is the Bi-Quadratic Form Function Method. This method is based on the assumption that the fine-mesh point flux can be expressed as the product of an assembly function and a bi-quadratic polynomial. Hoxie[4] obtained the assembly function, for interior nodes, from PDQ-7 assembly calculations, and for nodes near the water reflector, from PDQ-7 "extended assembly calculations." The unknown polynomial coefficients

were determined by forcing the fine-mesh flux to match, approximately, the QUANDRY node face and node volume averaged fluxes. A "source free condition" was also imposed, about node corner points, to obtain a complete set of equations needed for the determination of the polynomial coefficients. Khalil[6] modified Hoxie's scheme by calculating the assembly function through color set calculations for the nodes near the water reflector, and by forcing the fine-mesh flux to match, exactly, the QUANDRY averaged fluxes. The "source free condition," employed by Hoxie and Khalil, required that no net source of neutrons existed in a small box surrounding each corner point in the limit as the size of this box approached zero. However, it can be shown that different choices of the shape of the box lead to different values for such a limit.

In the present investigation and for two-dimensional applications, it will be assumed that the fine-mesh point flux can be expressed as the product of an assembly function and a bi-quadratic polynomial. The assembly function will be obtained from color set calculations. The polynomial coefficients will be determined by forcing the fine-mesh flux to match, exactly, the QUANDRY averaged fluxes, and to satisfy, in a finite difference fashion, the diffusion equation, Eq. 1-1, over the mesh cell domain about node corner points.

For three-dimensional applications, the form function used will be a tri-quadratic polynomial with 27 unknown coefficients. As a consequence of the increase in the number of unknown coefficients, additional balance conditions will have to be imposed along node lines. This flux reconstruction scheme, called the "Three-Dimensional Form Function Method," will be fully described in Chapter 2.

1.4 SUMMARY AND OBJECTIVES

In this chapter, some of the methods most commonly used for the determination of the neutron flux distribution in light water reactors have been considered. In particular, finite difference methods such as that incorporated into the computer code PDQ-7 and the analytical nodal method incorporated into the computer code QUANDRY have been introduced. Finally, some of the schemes for reconstructing fine-mesh flux shapes from nodal solutions have been briefly summarized.

The objective of this study is to develop an accurate and computationally efficient method for reconstructing two- and three-dimensional fine-mesh flux shapes from nodal solutions. In Chapter 2, the derivation of the Three-Dimensional Form Function Method is presented. In Chapter 3, the accuracy and computational efficiency of the Three-Dimensional Form Function Method when applied to two- and three-dimensional PWR benchmark problems is discussed. Finally, a summary of this investigation and recommendations for future research are given in Chapter 4.

Chapter 2

DERIVATION OF THE THREE-DIMENSIONAL FORM FUNCTION METHOD FOR RECONSTRUCTING FLUX SHAPES FROM NODAL SOLUTIONS

2.1 INTRODUCTION

In this chapter, a method for reconstructing flux shapes from three-dimensional reactor geometries will be derived. This method will be capable of calculating fine-mesh, three-dimensional fluxes and thus the reactor point-power distribution.

Within any reactor node, the reconstructed flux will be expressed as the product of an assembly function and a tri-quadratic polynomial. The assembly function will be obtained by a series of local fine-mesh, two-dimensional criticality calculations. The coefficients of the tri-quadratic polynomial will be the node volume averaged flux, the 6 node face averaged fluxes, the 12 node line averaged fluxes and the 8 node corner point fluxes. The node volume averaged flux and the node face averaged fluxes will be obtained by a three-dimensional global nodal calculation. The node line averaged fluxes and the node corner point fluxes will be calculated by solving the system of linear equations resulting from forcing the reconstructed flux to satisfy the multigroup neutron diffusion equation about node corner points and, in an integral sense, along node lines.

2.2 DERIVATION OF THE THREE-DIMENSIONAL FORM FUNCTION METHOD

The problem is treated in Cartesian coordinates. The reactor spatial domain, $\mathcal{D}_R$, is first partitioned into large rectangular right parallelepipeds, called nodes. Each node is specified by the indices (i,j,k) corresponding to the parallelepiped's left rear lower corner point. The coordinates of this corner point are given by (x_i,y_j,z_k). The nodal spatial domain, $\mathcal{D}^{i,j,k}$, for node (i,j,k) is defined by

$$\mathcal{D}^{i,j,k} \equiv \begin{cases} x \in [x_i, x_{i+1}) \\ y \in [y_j, y_{j+1}) \\ z \in [z_k, z_{k+1}) \end{cases} \tag{2-1}$$

Note that the nodal spatial domain, $\mathcal{D}^{i,j,k}$, includes the three node faces that contain corner point (x_i,y_j,z_k), but it does not include the other three node faces. Thus, neighboring nodal spatial domains will not have common points; this is to say that

$$\mathcal{D}^{i,j,k} \cap \mathcal{D}^{\ell,m,n} = \mathcal{D}^{i,j,k} \cdot \delta_{\ell,m,n}$$

where

$$\delta^{i,j,k}_{\ell,m,n} = \begin{cases} 1 & \text{if} \quad (i,j,k) = (\ell,m,n) \\ 0 & \text{if} \quad (i,j,k) \neq (\ell,m,n) \end{cases}$$

The global reactor spatial domain, $\mathcal{D}_R$, is thus the union of all the nodal domains.

The basic assumption of the three-dimensional form function method is that within any nodal spatial domain, $\mathcal{D}^{i,j,k}$, and for neutron group g, the reconstructed flux, $\phi_g^{i,j,k}(x,y,z)$ can be expressed as the product of a two-dimensional assembly function, $\psi_g^{i,j,k}(x,y)$, and a tri-quadratic polynomial function, $P_g^{i,j,k}(x,y,z)$. Thus,

$$\phi_g^{i,j,k}(x,y,z) = \begin{cases} \psi_g^{i,j,k}(x,y) \cdot p_g^{i,j,k}(x,y,z) & \text{for} \quad (x,y,z) \in \mathcal{D}^{i,j,k} \\ 0 & \text{for} \quad (x,y,z) \notin \mathcal{D}^{i,j,k} \end{cases} \tag{2-2}$$

where

$\phi_g^{i,j,k}(x,y,z)$ ≡ reconstructed flux function for group g and node (i,j,k)

$\psi_g^{i,j,k}(x,y)$ ≡ assembly function for group g and node (i,j,k)

$p_g^{i,j,k}(x,y,z)$ ≡ tri-quadratic polynomial function for group g and node (i,j,k)

The reconstructed flux, $\phi_g(x,y,z)$, for group g and for the whole reactor spatial domain, $\mathcal{D}_R$, can be expressed as

$$\phi_g(x,y,z) = \sum_{i=1}^{i=I} \sum_{j=1}^{j=J} \sum_{k=1}^{k=K} \phi_g^{i,j,k}(x,y,z) \quad \text{for} \quad (x,y,z) \in \mathcal{D}_R \tag{2-3}$$

where I, J and K are the number of reactor nodes in the X, Y and Z directions.

Note that the reconstructed flux, $\phi_g(x,y,z)$, as defined by Equations 2-3, 2-2 and 2-1, will be a single-valued function; thus, there will be only one unique value for the reconstructed flux at any point (x,y,z) within the reactor spatial domain, $\mathcal{D}_R$.

The assembly function, $\psi_g^{i,j,k}(x,y)$, can be obtained by solving the multigroup neutron diffusion equation by a fine-mesh, two-dimensional assembly or color set criticality calculation with appropriate boundary conditions. Color sets are assembly-sized regions composed of four quadrants of four different assemblies; usually, a zero current boundary condition is a good choice for color set boundaries. Such fine-mesh

criticality calculations can be performed with existing finite difference computer codes like, for instance, PDQ-7.[9]

The polynomial function, $P_g^{i,j,k}(x,y,z)$, appearing in Eq. 2-2 can be written as

$$P_g^{i,j,k}(x,y,z) = \sum_{\ell=0}^{2} \sum_{m=0}^{2} \sum_{n=0}^{2} a_{g,\ell,m,n}^{i,j,k} \, X^{\ell} \cdot Y^{n} \cdot Z^{n} \qquad (2\text{-}4)$$

Since no separability is assumed, there are 27 independent polynomial coefficients, $a_{g,\ell,m,n}^{i,j,k}$, for each neutron group, g, and reactor node (i,j,k). Once these polynomial coefficients are obtained, the reconstructed flux, $\phi_g(x,y,z)$, can be easily computed by using Eqs. 2-4, 2-3 and 2-2. In order to determine such coefficients, it is required to impose, for each group and node, 27 conditions on the reconstructed flux, or, in other words, to set a system of 27 independent equations.

Seven independent equations can be obtained for each group and node by forcing the reconstructed flux, $\phi_g^{i,j,k}(x,y,z)$, when integrated over the node faces and the node volume, to reproduce the group nodal face-averaged fluxes, $\bar{\phi}_{g,s}^{i,j,k}$, (s = 1,...,6), and the group nodal averaged flux, $\bar{\bar{\phi}}_g^{i,j,k}$. These averaged nodal face-fluxes, $\bar{\phi}_{g,s}^{i,j,k}$ (s = 1,...,6), and the nodal volume averaged flux, $\bar{\bar{\phi}}_g^{i,j,k}$, can be obtained from a global three-dimensional nodal calculation.

An additional set of 20 independent equations for group and node can be obtained by forcing the reconstructed flux, $\phi_g(x,y,z)$, to satisfy the multigroup neutron diffusion equation about the 8 node corner points and, in an integral sense, along the 12 node lines connecting corner points. This system of 27 equations (per group and node) can be solved for the 27 unknown polynomial coefficients, and thus the reconstructed flux can be

evaluated by using Eqs. 2-4, 2-3 and 2-2.

The polynomial function, $P_g^{i,j,k}(x,y,z)$, appearing in Eq. 2-4 is an analytical function and thus continuous and with continuous partial derivatives within the node. However, the assembly function, $\psi_g^{i,j,k}(x,y)$, in Eq. 2-2, is usually obtained by solving the multigroup neutron diffusion equation by a finite difference approach; thus, it is neigher continuous nor differentiable within the node. In order to be mathematically consistent, it is convenient to treat the polynomial function, $P_g^{i,j,k}(x,y,z)$, as a piecewise flat function within mesh cubes, rather than as an analytical function. With this understanding, the reconstructed flux will be forced to satisfy the multigroup finite difference neutron diffusion equation, rather than the multigroup partial differential neutron diffusion equation.

2.2.1 Reproduction of the Nodal Solution

The condition that forces the reconstructed flux, $\phi_g^{i,j,k}(x,y,z)$, to reproduce the global nodal solution can be expressed by the following equations:

$$\begin{aligned} &\frac{1}{\Delta s_\alpha^{i,j,k}} \iint_{s_\alpha^{i,j,k}} \phi_g^{i,j,k}(x,y,z)\, ds = \bar{\bar{\phi}}_g(s_\alpha^{i,j,k}) \qquad (\alpha = 1, \ldots, 6) \\ &\frac{1}{\Delta v^{i,j,k}} \iiint_{v^{i,j,k}} \phi_g^{i,j,k}(x,y,z)\, dv = \bar{\bar{\bar{\phi}}}_g(v^{i,j,k}) \end{aligned} \tag{2-5}$$

where

$\Delta s_\alpha^{i,j,k}$ ≡ surface area α of node (i,j,k), where α is the index corresponding to each node face, α varies from 1 to 6,

$\Delta v^{i,j,k}$ ≡ volume of node (i,j,k),

$\phi_g^{i,j,k}(x,y,z)$ ≡ reconstructed flux for group g and node (i,j,k),

$\bar{\bar{\phi}}_g(S_\alpha^{i,j,k})$ ≡ nodal surface averaged flux for node face α, ($\alpha = 1,\ldots,6$) for node (i,j,k) obtained from a global nodal calculation,

$\bar{\bar{\bar{\phi}}}_g(V^{i,j,k})$ ≡ volume averaged flux for node (i,j,k) obtained by a global nodal calculation.

Rather than attempting to solve Eq. 2-5 simultaneously with the equations resulting from applying a neutron balance about node corner points and node lines, it is advantageous to rewrite the polynomial function, $p_g^{i,j,k}(x,y,z)$, defined by Eq. 2-4 in terms of the 8 unknown corner point fluxes, ϕ_{cg}, and the 12 unknown node line averaged fluxes, $\bar{\phi}_{Lg}$, and in terms of the 6 known face averaged nodal fluxes, $\bar{\bar{\phi}}_{g,u}^{i,j,k}$, and the known volume averaged nodal flux, $\bar{\bar{\bar{\phi}}}_g^{i,j,k}$. This can be accomplished by introducing an appropriate set of known numerical "integral coefficients," which depend on the node geometry and on the assembly function. By doing this, the general tri-quadratic polynomial, $P_g^{i,j,k}(x,y,z)$, given by Eq. 2-4, with 27 unknown coefficients, is transformed into an equivalent polynomial, $Q_g^{i,j,k}(x,y,z)$, with only 20 unknown coefficients. The reconstructed flux for group g and node (i,j,k) can be expressed in terms of $Q_g^{i,j,k}(x,y,z)$ as

$$\phi_g^{i,j,k}(x,y,z) = \begin{cases} \psi_g^{i,j,k}(x,y) \cdot Q_g^{i,j,k}(x,y,z) & \text{for } (x,y,z) \in \mathcal{D}^{i,j,k} \\ 0 & \text{for } (x,y,z) \notin \mathcal{D}^{i,j,k} \end{cases} \tag{2-6}$$

where the coefficients of $Q_g^{i,j,k}(x,y,z)$ are such that the reconstructed flux, $\phi_g^{i,j,k}(x,y,z)$, will reproduce the (still unknown) node corner point fluxes and known line averaged fluxes as well as the (known) face averaged and volume averaged nodal fluxes. When the polynomial $Q_g^{i,j,k}(x,y,z)$ is explicitly written in terms of the node corner point fluxes, ϕ_{cg}, and node averaged fluxes, $\bar{\phi}_{Lg}$, $\bar{\bar{\phi}}_{sg}$, $\bar{\bar{\bar{\phi}}}_g$, then Eq. 2-6 written in conventional matrix

form becomes

$$
\begin{aligned}
[\phi^{i,j,k}(x,y,z)] = {} & [C_1^{i,j,k}(x,y,z)][\phi_c^{i,j,k}] + [C_2^{i,j,k}(x,y,z)][\phi_c^{i+1,j,k}] \\
& + [C_3^{i,j,k}(x,y,z)][\phi_c^{i+1,j+1,k+1}] + [C_4^{i,j,k}(x,y,z)][\phi_c^{i,j+1,k}] \\
& + [C_5^{i,j,k}(x,y,z)][\phi_c^{i,j,k+1}] + [C_6^{i,j,k}(x,y,z)][\phi_c^{i+1,j,k+1}] \\
& + [C_7^{i,j,k}(x,y,z)][\phi_c^{i+1,j+1,k+1}] + [C_8^{i,j,k}(x,y,z)][\phi_c^{i,\ j+1,k+1}] \\
& + [S_1^{i,j,k}(x,y,z)][\bar{\phi}_x^{i,j,k}] + [S_2^{i,j,k}(x,y,z)][\bar{\phi}_x^{i,j+1,k}] \\
& + [S_3^{i,j,k}(x,y,z)][\bar{\phi}_y^{i+1,j,k}] + [S_4^{i,j,k}(x,y,z)][\bar{\phi}_y^{i,j,k}] \\
& + [S_5^{i,j,k}(x,y,z)][\bar{\phi}_x^{i,j,k+1}] + [S_6^{i,j,k}(x,y,z)][\bar{\phi}_x^{i,j+1,k+1}] \\
& + [S_7^{i,j,k}(x,y,z)][\bar{\phi}_y^{i+1,j,k+1}] + [S_8^{i,j,k}(x,y,z)][\bar{\phi}_y^{i,j,k+1}] \\
& + S_9^{i,j,k}(x,y,z)][\bar{\phi}_z^{i,j,k}] + S_{10}^{i,j,k}(x,y,z)][\bar{\phi}_z^{i+1,j,k}] \\
& + [S_{11}^{i,j,k}(x,y,z)][\bar{\phi}_z^{i+1,j+1,k}] + [S_{12}^{i,j,k}(x,y,z)][\bar{\phi}_z^{i,j+1,k}] \\
& + [V_1^{i,j,k}(x,y,z)][\bar{\bar{\phi}}_y^{i,j,k}] + [V_2^{i,j,k}(x,y,z)][\bar{\bar{\phi}}_y^{i,j+1,k}] \\
& + [V_3^{i,j,k}(x,y,z)][\bar{\bar{\phi}}_x^{i+1,j,k}] + [V_4^{i,j,k}(x,y,z)][\bar{\bar{\phi}}_x^{i,j,k}] \\
& + [V_5^{i,j,k}(x,y,z)][\bar{\bar{\phi}}_z^{i,j,k}] + [V_6^{i,j,k}(x,y,z)][\bar{\bar{\phi}}_z^{i,j,k+1}] \\
& + [W^{i,j,k}(x,y,z)][\bar{\bar{\bar{\phi}}}^{i,j,k}] \qquad \text{for} \quad (x,y,z) \in \mathcal{D}^{i,j,k}
\end{aligned}
\tag{2-7}
$$

$$
[\phi^{i,j,k}(x,y,z)] = [0] \qquad \text{for} \quad (x,y,z) \notin \mathcal{D}^{i,j,k}
$$

where

$[\phi_c^{i,j,k}]$ ≡ column vector of length equal to the number, G, of neutron groups containing the corner point fluxes at point (i,j,k),

$[\bar{\phi}_u^{i,j,k}]$ ≡ column vector of length G containing the line averaged fluxes for node line parallel to direction u (u = x,y,x),

$[\bar{\bar{\phi}}_u^{i,j,k}]$ ≡ column vector of length G containing the surface averaged fluxes for node face perpendicular to direction u (u = x,y,z),

$[\bar{\bar{\bar{\phi}}}^{i,j,k}]$ ≡ column vector of length G containing the volume averaged fluxes for node (i,j,k),

and the functions $[C^{i,j,k}(x,y,z)]$, $[S^{i,j,k}(x,y,z)]$, $[V^{i,j,k}(x,y,z)]$ and $[W^{i,j,k}(x,y,z)]$ are G × G diagonal matrices whose elements are defined in Appendix A. Figure 2-1 indicates the index notation for the corner point fluxes and node average fluxes for node (i,j,k).

2.2.2 Derivation of the Balance Equations about Corner Points

In order to derive the neutron balance equations about node corner points, it is first required to establish a three-dimensional, rectangular, fine-mesh grid over every reactor node. The projection of this mesh grid over horizontal planes (OXY planes) should be identical with the two-dimensional fine-mesh grid used for calculating the assembly function, $\psi^{i,j,k}(x,y)$. However, the mesh spacing corresponding to the Z direction can be arbitrarily chosen.

A mesh point is defined at the intersection of three fine-mesh grid lines. A mesh box is defined as the right parallelepiped whose vertexes are six neighboring fine-mesh points. A mesh cell is defined as the right parallelepiped centered in a mesh point whose sides are parallel to the coordinate plane; the mesh cell sides intersect the midpoints between the cell center and its nearest neighbors. Thus, every mesh cell contains portions of 8 different mesh boxes and vice versa. Figure 2-2 shows a

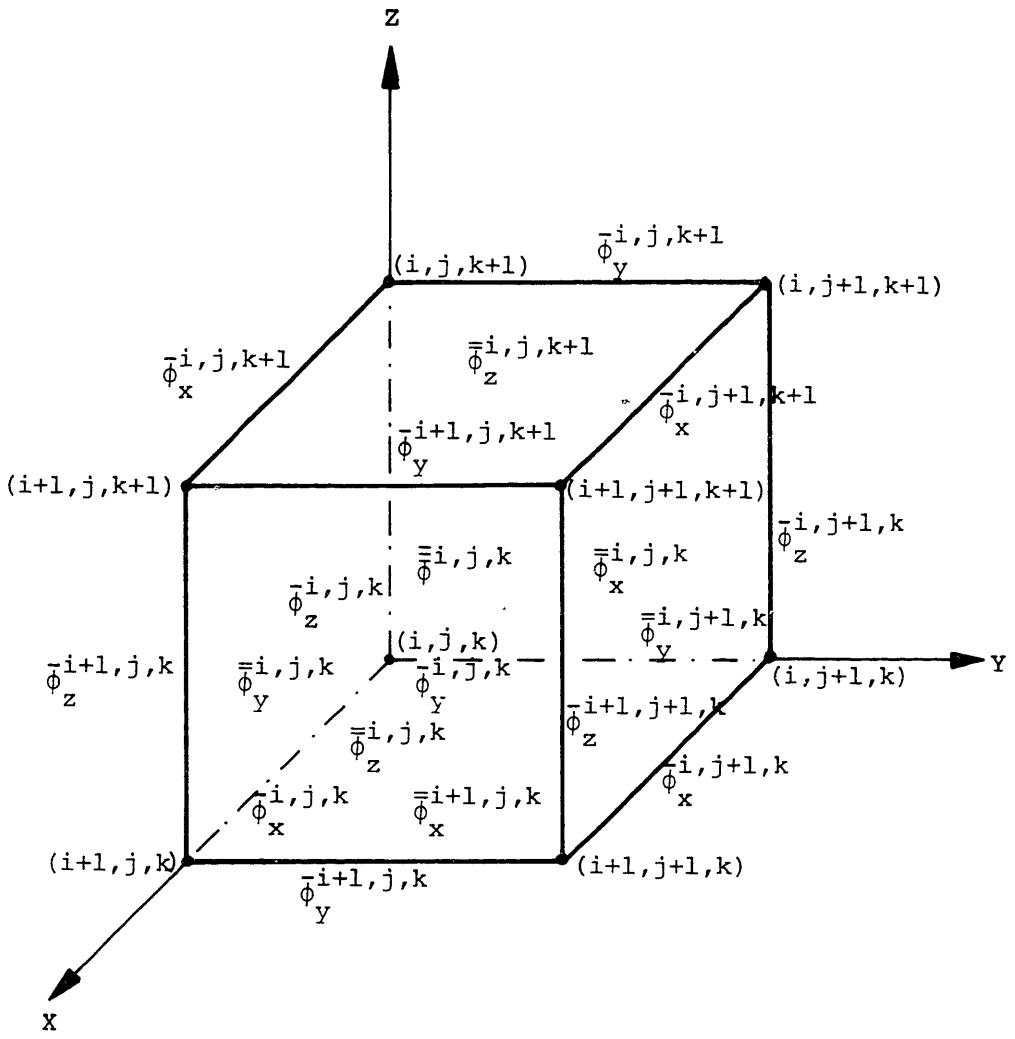

Fig. 2-1. Index notation for corner point fluxes and node averaged fluxes for node (i,j,k).

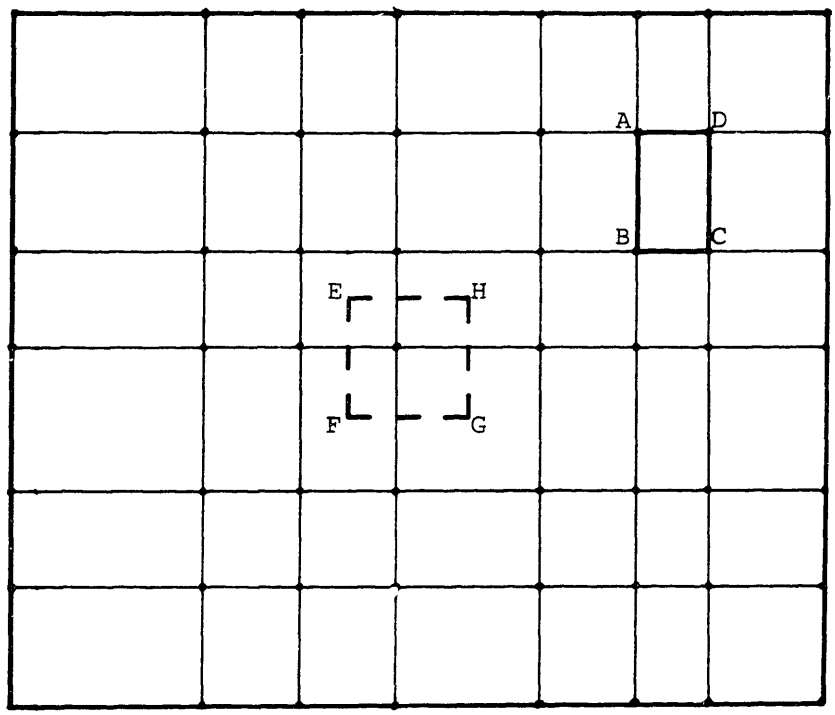

Fig. 2-2. Two-dimensional fine-mesh grid. Rectangle ABCD represents a generic 2-D mesh box. Rectangle EFGH represents a generic 2-D mesh cell.

two-dimensional, fine-mesh grid and a generic mesh box and mesh cell.

The neutron balance equation about node corner points is derived by integrating the multigroup neutron diffusion equation, Eq. 1-1, over the mesh cell about the node corner point. This integration is performed according to the mesh-point-centered finite difference scheme. In this scheme, the group flux, $\phi_g(x,y,z)$, is defined at mesh points and it is assumed to be constant within the mesh cell. The nuclear composition is assumed to be constant within each mesh box; thus, a mesh cell can contain up to 8 different nuclear compositions. The partial derivatives at the mesh cell faces are calculated by the centered finite difference approximation. The application of this mesh point balance condition about corner points yields the following equation:

$$[X_N^{i,j,k}][\phi_N^{i,j,k}] + [X_S^{i,j,k}][\phi_S^{i,j,k}] + [X_E^{i,j,k}][\phi_E^{i,j,k}] + [X_W^{i,j,k}][\phi_W^{i,j,k}] + [X_T^{i,j,k}][\phi_T^{i,j,k}] + [X_B^{i,j,k}][\phi_B^{i,j,k}] + [X_C^{i,j,k}][\phi_c^{i,j,k}] = [0] \tag{2-8}$$

where $[\phi_c^{i,j,k}]$ is a column vector of length G containing the corner point fluxes at point (i,j,k), and $[\phi_N^{i,j,k}]$, $[\phi_S^{i,j,k}]$, $[\phi_E^{i,j,k}]$, $[\phi_W^{i,j,k}]$, $[\phi_T^{i,j,k}]$ and $[\phi_B^{i,j,k}]$ are column vectors of length G containing the neutron fluxes at nearest neighbor fine-mesh points N, S, E, W, T, and B, which correspond to the north, south, east, west, top and bottom directions; they are shown in Fig. 2-3. Note that in this figure there may be many fine-mesh points between, for example, the nearest neighbor to corner point (i,j,k), and corner point (i+1,j,k). The coefficients $[X^{i,j,k}]$ are G × G matrices defined in Appendix B.

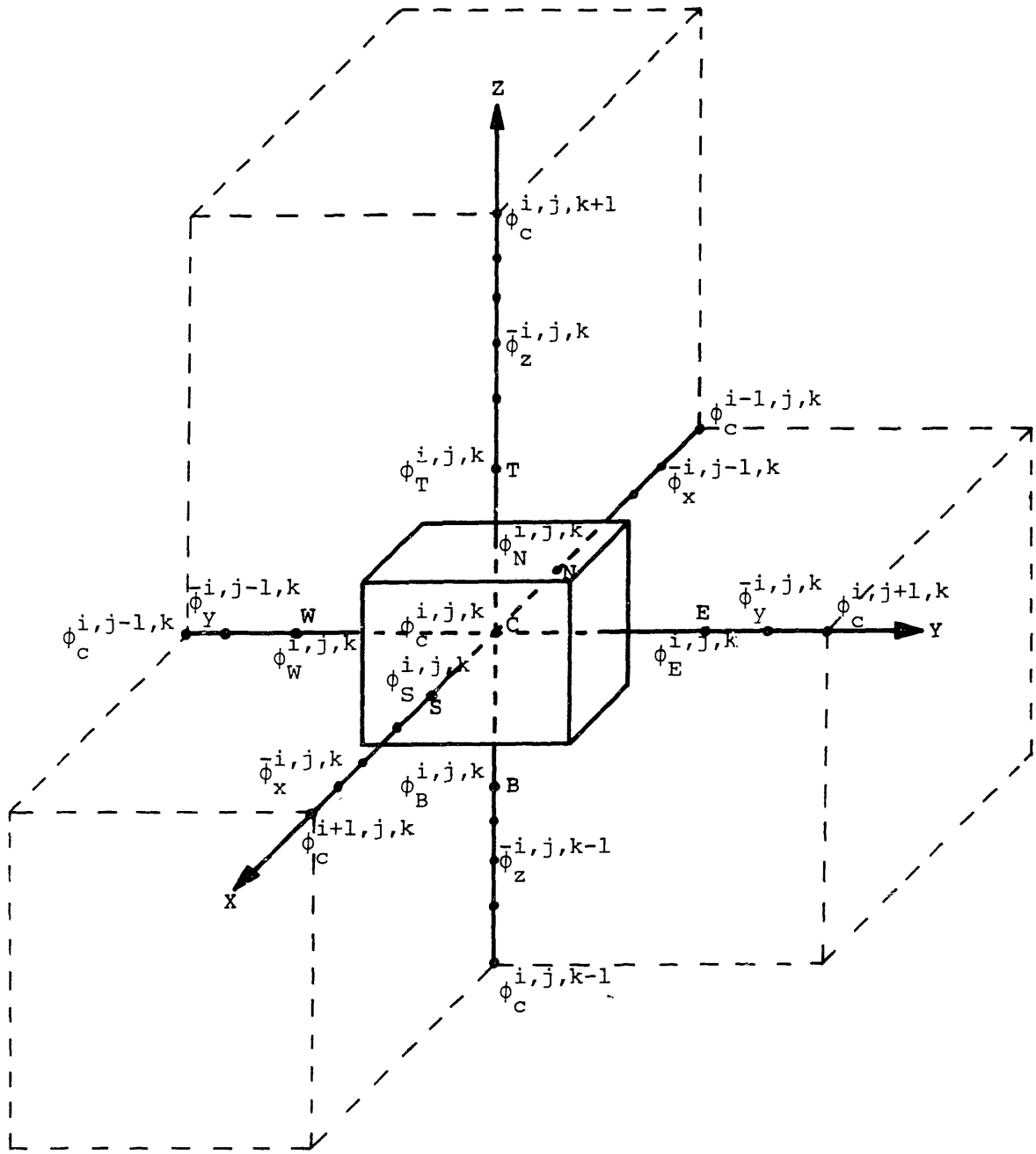

Fig. 2-3. Geometry and nomenclature for the corner point balance equation.

In order to obtain an equation involving only node corner point fluxes and node line averaged fluxes, it is required to eliminate from Eq. 2-8 the fine-mesh point fluxes $[\phi_N^{i,j,k}]$, $[\phi_S^{i,j,k}]$, $[\phi_E^{i,j,k}]$, $[\phi_W^{i,j,k}]$, $[\phi_T^{i,j,k}]$ and $[\phi_B^{i,j,k}]$ at nearest neighbor fine-mesh points in the north, south, east, west, top and bottom directions. This can be accomplished by using Eq. 2-7. Equation 2-7 simplifies for points along node lines; thus fine-mesh point fluxes along node lines can be expressed as a linear function which involves only three terms: the two node corner point fluxes at the ends of the node line and the averaged flux along that line. Thus, when fine-mesh point fluxes are eliminated from Eq. 2-8, the balance condition about corner points can be written as

$$
\begin{aligned}
&[P_N^{i,j,k}][\phi_c^{i-1,j,k}] + [P_S^{i,j,k}][\phi_c^{i+1,j,k}] + [P_E^{i,j,k}][\phi_c^{i,j+1,k}] \\
&\quad + [P_W^{i,j,k}][\phi_c^{i,j-1,k}] + [P_T^{i,j,k}][\phi_c^{i,j,k+1}] + [P_B^{i,j,k}][\phi_c^{i,j,k-1}] \\
&\quad + [P_C^{i,j,k}][\phi_c^{i,j,k}] + [\bar{P}_N^{i,j,k}][\bar{\phi}_x^{i-1,j,k}] + [\bar{P}_S^{i,j,k}][\bar{\phi}_x^{i,j,k}] \\
&\quad + [P_E^{i,j,k}][\bar{\phi}_y^{i,j,k}] + [\bar{P}_W^{i,j,k}][\bar{\phi}_y^{i,j-1,k}] + [\bar{P}_T^{i,j,k}][\bar{\phi}_z^{i,j,k}] \\
&\quad + [\bar{P}_B^{i,j,k}][\bar{\phi}_z^{i,j,k-1}] = [0] \qquad (2\text{-}9)
\end{aligned}
$$

where the corner point fluxes $[\phi_c]$ and the line averaged fluxes $[\bar{\phi}_u]$, $(u = x,y,z)$ are shown in Fig. 2-3, and the matrices $[P^{i,j,k}]$ and $[\bar{P}^{i,j,k}]$ are defined in Appendix B.

Equation 2-9 is the corner point balance equation which couples 7 corner point fluxes and 6 line averaged fluxes. A detailed derivation of Eq. 2-9 is presented in Appendix B.

2.2.3 Derivation of the Balance Equation along Node Lines

A line cell is defined as the parallelepiped that contains all mesh cells along a node line excluding the two mesh cells corresponding to the corner points that define such a node line. Figure 2-4 represents a two-dimensional line cell.

In order to derive the balance equation along node lines, it is necessary to integrate the multigroup neutron diffusion equation over the line cell about the node line. This integration is performed according to the mesh-point-centered finite difference scheme. The application of this balance condition along a node line parallel to the X axis yields to the following equation:

$$\sum_{\alpha=2}^{p-1} \Big\{ [R_{L,\alpha}^{i,j,k}][\phi_{L,\alpha}^{i,j,k}] + R_{E,\alpha}^{i,j,k}][\phi_{E,\alpha}^{i,j,k}] + [R_{W,\alpha}^{i,j,k}][\phi_{W,\alpha}^{i,j,k}] + [R_{T,\alpha}^{i,j,k}][\phi_{T,\alpha}^{i,j,k}] + [R_{B,\alpha}^{i,j,k}][\phi_{B,\alpha}^{i,j,k}] \Big\}$$
$$+ [R_{N}^{i,j,k}]\Big([\phi_{c}^{i,j,k}] - [\phi_{L,2}^{i,j,k}]\Big)$$
$$+ [R_{S}^{i,j,k}]\Big([\phi_{c}^{i+1,j,k}] - [\phi_{L,p-1}^{i,j,k}]\Big) = [0] \qquad (2\text{-}10)$$

where α is a dummy index referring to the fine-mesh points on the node line and the four, parallel, nearest neighbor lines. (In this notation, $[\phi_{L,1}^{i,j,k}]$ and $[\phi_{L,p}^{i,j,k}]$ would be the corner point fluxes $[\phi_{c}^{i,j,k}]$ and $[\phi_{c}^{i+1,j,k}]$.) $[\phi_{L,\alpha}^{i,j,k}]$, $[\phi_{E,\alpha}^{i,j,k}]$, $[\phi_{W,\alpha}^{i,j,k}]$, $[\phi_{T,\alpha}^{i,j,k}]$ and $[\phi_{B,\alpha}^{i,j,k}]$ are column vectors of length G containing the neutron fluxes at fine-mesh points L_α, E_α, W_α, T_α and B_α which are shown in Fig. 2-5. The matrices $[R^{i,j,k}]$ are defined in Appendix C.

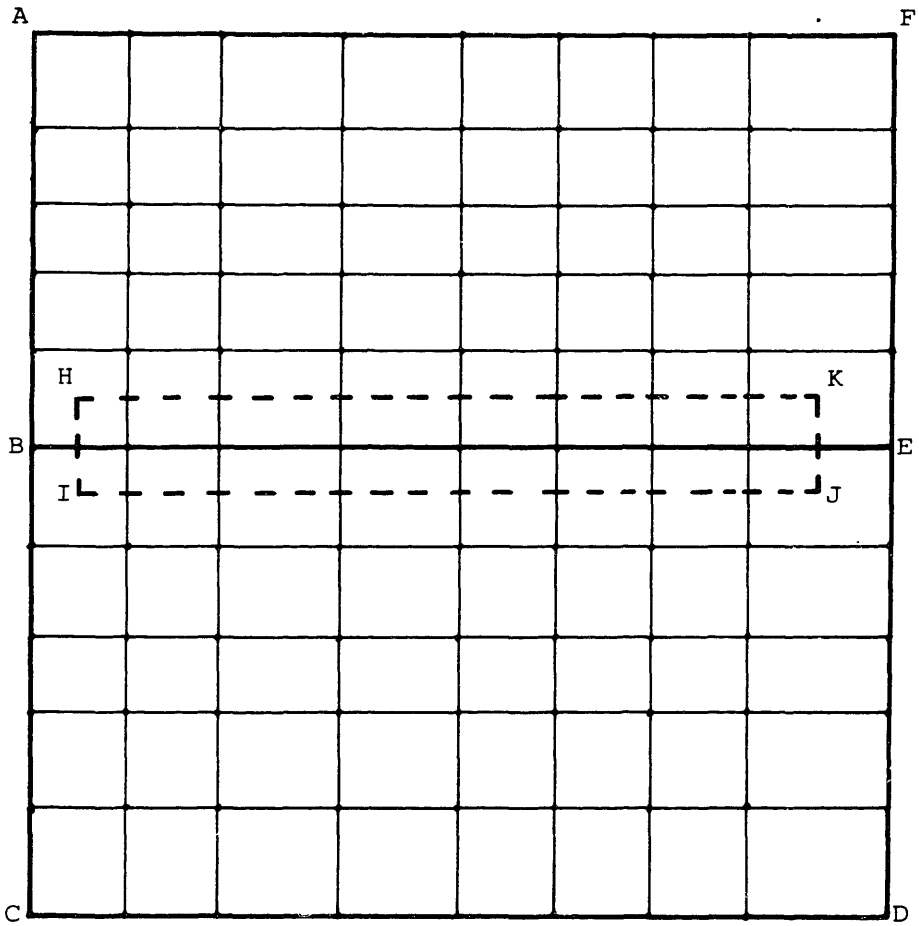

Fig. 2-4. Two-dimensional line cell.

Nodes ABEF and BCDE share the node line BE. Rectangle HIJK about node line BE is defined as a 2D-line cell.

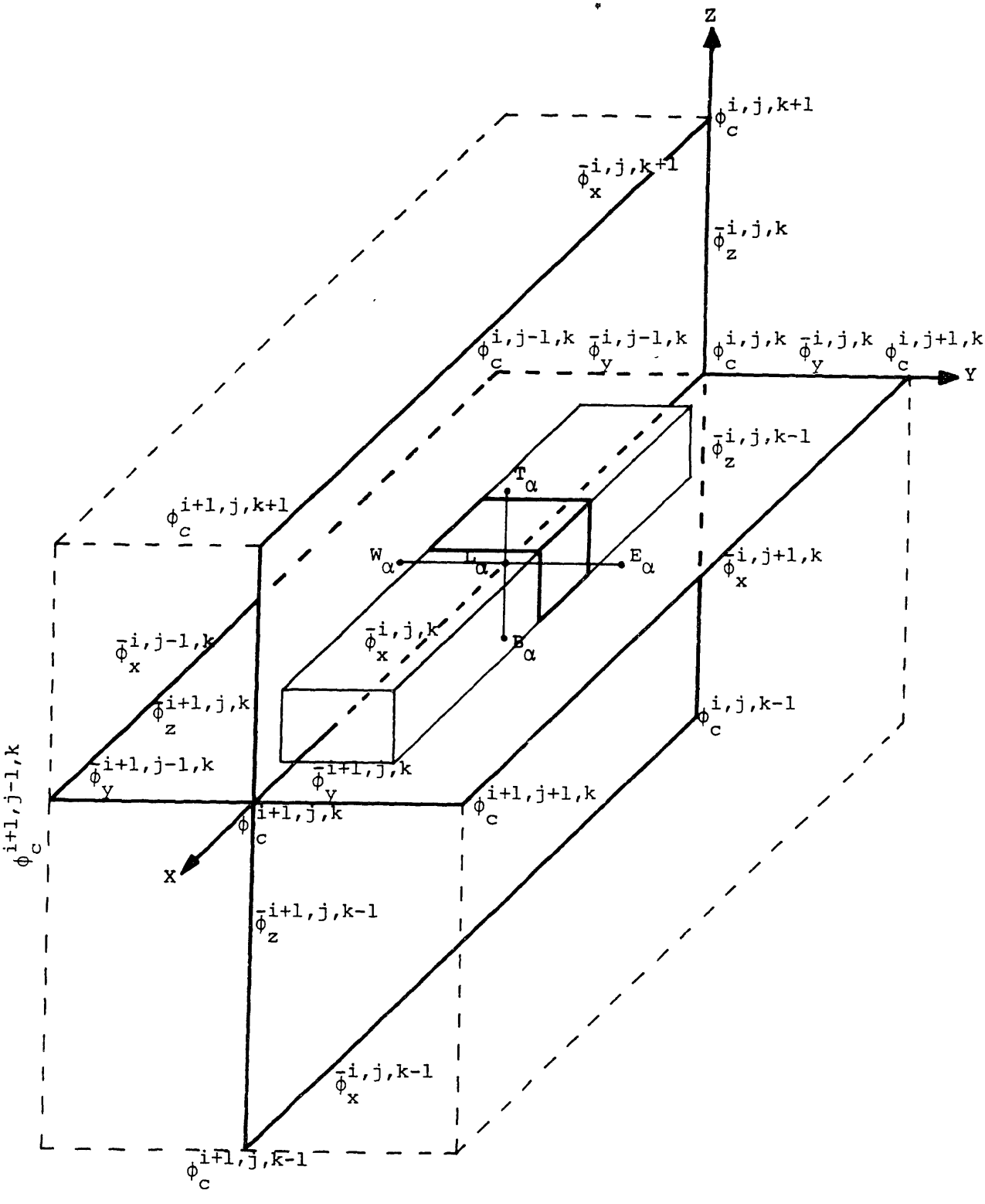

Fig. 2-5. Geometry and nomenclature for the node line balance equation.

An equation involving only corner point fluxes and averaged fluxes can be obtained by eliminating the fine-mesh point fluxes appearing in Eq. 2-10 by means of Eq. 2-7. Equation 2-7 simplifies for points along node faces. Thus, fine-mesh point fluxes along node faces can be expressed as a linear function involving only 9 terms: the 4 corner point fluxes, the 4 line averaged fluxes, and the face averaged flux corresponding to such a node face.

When these fine-mesh point fluxes are eliminated, the balance condition for node lines becomes:

$$
\begin{aligned}
&[A_{x,C}^{i,j,k}][\bar{\phi}_x^{i,j,k}] + [A_{x,T}^{i,j,k}][\bar{\phi}_x^{i,j,k+1}] + [A_{x,B}^{i,j,k}][\bar{\phi}_x^{i,j,k-1}] + [A_{x,E}^{i,j,k}][\bar{\phi}_x^{i,j+1,k}] \\
&\quad + [A_{x,W}^{i,j,k}][\bar{\phi}_x^{i,j-1,k}] + [N_{x,C}^{i,j,k}][\phi_c^{i,j,k}] + [N_{x,T}^{i,j,k}][\phi_c^{i,j,k+1}] \\
&\quad + [N_{x,B}^{i,j,k}][\phi_c^{i,j,k-1}] + [N_{x,E}^{i,j,k}][\phi_c^{i,j+1,k}] + [N_{x,W}^{i,j,k}][\phi_c^{i,j-1,k}] \\
&\quad + [S_{x,C}^{i,j,k}][\phi_c^{i+1,j,k}] + [S_{x,T}^{i,j,k}][\phi_c^{i+1,j,k+1}] + [S_{x,B}^{i,j,k}][\phi_c^{i+1,j,k-1}] \\
&\quad + [S_{x,E}^{i,j,k}][\phi_c^{i+1,j+1,k}] + [S_{x,W}^{i,j,k}][\phi_c^{i+1,j-1,k}] + [\bar{N}_{x,T}^{i,j,k}][\bar{\phi}_z^{i,j,k}] \\
&\quad + [\bar{N}_{x,B}^{i,j,k}][\bar{\phi}_z^{i,j,k-1}] + [\bar{N}_{x,E}^{i,j,k}][\bar{\phi}_y^{i,j,k}] + [\bar{N}_{x,W}^{i,j,k}][\bar{\phi}_y^{i,j-1,k}] \\
&\quad + [\bar{S}_{x,T}^{i,j,k}][\bar{\phi}_z^{i+1,j,k}] + [\bar{S}_{x,B}^{i,j,k}][\bar{\phi}_z^{i+1,j,k-1}] + [\bar{S}_{x,E}^{i,j,k}][\bar{\phi}_y^{i+1,j,k}] \\
&\quad + [\bar{S}_{x,W}^{i,j,k}][\bar{\phi}_y^{i+1,j-1,k}] = [R_x^{i,j,k}] \qquad (2\text{-}11)
\end{aligned}
$$

where the corner point fluxes $[\phi_c]$ and the line averaged fluxes $[\bar{\phi}_u]$, $(u = x,y,z)$ are shown in Fig. 2-5, and the matrices $[A_x^{i,j,k}]$, $[N_x^{i,j,k}]$, $[S_x^{i,j,k}]$, $[\bar{N}_x^{i,j,k}]$, $[\bar{S}_x^{i,j,k}]$ and $[R_x^{i,j,k}]$ are defined in Appendix C.

Equation 2-11 is the balance equation along a node line parallel to the X axis. This equation couples 10 node corner point fluxes and 13 line

averaged fluxes. Similar equations can be derived for the node lines parallel to the Y axis and to the Z axis, and are given in Appendix C.

2.3 A METHOD FOR SOLVING THE BALANCE EQUATIONS

A systematic method for obtaining all the equations required to calculate the node corner point fluxes and node line averaged fluxes for the whole reactor can be devised by formulating at any reactor corner point (i,j,k) the following balance equations:

1. Balance equation about corner point (i,j,k).
2. Balance equation along node line parallel to the X axis.
3. Balance equation along node line parallel to the Y axis.
4. Balance equation along node line parallel to the Z axis.

The implementation of these equations at all reactor node corner points will result in a system of coupled linear equations relating all node corner point fluxes and node line averaged fluxes. These equations, along with the appropriate boundary conditions applied at the reactor surface, uniquely determine the node corner point fluxes, $[\phi_c]$, and node line averaged fluxes $[\bar{\phi}_u]$, $(u = x,y,z)$ which are required for reconstructing the fine-mesh flux according to Eq. 2-7. Appendix D describes the implementation of the reactor surface boundary conditions.

Since the coupling is very strong and since all neutron groups are coupled, this system of equations needs to be solved simultaneously.

The Gauss-Seidel iterative method can be applied to solve such equations. In order to implement this iterative scheme, it is first necessary to provide a first guess for the corner point fluxes, $[\phi_c^{(0)}]$, and node line averaged fluxes, $[\bar{\phi}_u^{(0)}]$ $(u = x,y,z)$. This first guess can be interpolated from the global nodal solution.

Updated values for the corner point fluxes, $[\phi_c^{(p_1)}]$, can be obtained by performing p_1 Gauss-Seidel inner iterations to the corner point balance equation, Eq. 2-9; then using these updated values for the corner point fluxes, new values of the averaged fluxes for node lines parallel to the X axis, $[\bar{\phi}_x^{(x_1)}]$, can be obtained by performing x_1 Gauss-Seidel inner iterations to the balance equation along the node lines parallel to the X axis, Eq. 2-11. Similarly, y_1 and z_1 inner iterations can be performed for the balance equations corresponding to node lines parallel to the Y axis, Eq. C-7, and Z axis, Eq. C-8, to obtain updated node line averaged flux values, $[\bar{\phi}_y^{(y_1)}]$ and $[\bar{\phi}_z^{(z_1)}]$. Note that in this iterative scheme, as soon as a new value is obtained it replaces the old value.

Thus, after one outer iteration and p_1, x_1, y_1 and z_1 inner iterations, new values for the corner point fluxes, $[\phi_c^{(p_1)}]$, and node line averaged fluxes, $[\bar{\phi}_x^{(x_1)}]$, $[\bar{\phi}_y^{(y_1)}]$, $[\bar{\phi}_z^{(z_1)}]$ are available. This process is repeated until, after n outer iterations, convergence is reached.

In the problems for which this iterative scheme was tested, convergence occurred most rapidly when only one inner iteration ($p_i=x_i=y_i=z_i=1$) was performed for each i-outer iteration.

2.4 SUMMARY

In this chapter and related appendices, a scheme for reconstructing three-dimensional flux shapes from nodal solutions has been derived. This scheme is capable of determining fine-mesh, point-fluxes over the reactor geometry and thus the reactor point-power distribution when a global nodal solution is known and a series of two-dimensional, fine-mesh calculations are performed. The reconstructed flux will reproduce the

global nodal solution and will also satisfy the neutron-diffusion, finite-difference equations about node corner points and, in an integral sense, along node lines.

In Chapter 3, practical implementation of this flux reconstruction scheme will be discussed. In addition, applications to two- and three-dimensional benchmark problems will be presented.

Chapter 3

APPLICATIONS

3.1 INTRODUCTION

In Chapter 2, the Three-Dimensional Form Function Method for reconstructing flux shapes from nodal solutions was derived. In this chapter, results from application of the Form Function Method to two- and three-dimensional, two-group, reactor benchmark problems are presented.

In Section 2, the major computer codes required to calculate the fine-mesh flux and pointwise power are briefly summarized.

In Sections 3 and 4, the accuracy of the flux reconstruction scheme, when applied to two- and three-dimensional benchmark reactor problems is examined by comparing the node corner point fluxes predicted by this method with those obtained by a conventional finite difference method. Since the node face averaged fluxes and node volume averaged fluxes obtained by a nodal calculation are input data for reconstructing the fine-mesh flux, the accuracy of the nodal solution is also examined by comparing the averaged nodal power predicted by the nodal method to that obtained by a standard finite difference method.

In Section 5, several numerical considerations are presented. In particular, the computational efficiencies of the Form Function Method and Nodal Method are compared to that of a standard finite difference method.

3.2 COMPUTER CODES

All the numerical reference solutions were obtained using the PDQ-7 computer code. This code solves the two-group, corner-point-centered finite difference neutron diffusion equations.

The fine-mesh local criticality calculations for obtaining the assembly function, $\psi_g^{i,j,k}(x,y)$, appearing in Eq. 2-2, were also obtained using the PDQ-7 computer code.

The node face averaged fluxes, $\bar{\bar{\phi}}_u$ $(u = x,y,z)$, and node volume averaged fluxes, $\bar{\bar{\phi}}$, appearing in Eq. 2-7 were calculated using the Analytical Nodal Method incorporated into the QUANDRY computer code. The homogenized cross sections and discontinuity factors, input data for QUANDRY, were calculated by local criticality calculations using the PDQ-7 code.

The methods developed in Chapter 2 and related appendices have been incorporated into a computer code called REFLUX (Reconstruction of the Flux). This computer code solves two- and three-dimensional, two-group diffusion theory problems. REFLUX has been written in IBM FORTRAN IV computer language. The input data for REFLUX are the reactor geometry information, the reactor boundary conditions, the heterogeneous nuclear composition, the assembly function, the nodal face averaged fluxes and the nodal volume averaged fluxes. The code, first reads and processes the input data; then it evaluates the numerical coefficients P, Q, T, R, B appearing in the polynomial function and defined in Appendix A; then it calculates the coefficients appearing in the balance equations about node corner points and along node lines, Eqs. B-6, C-6, C-7, C-8; then it solves this system of balance equations by a Gauss-Seidel iterative scheme to obtain the node

corner point fluxes and node line averaged fluxes, and finally, it reconstructs the two-group, fine-mesh flux and the fine-mesh power density.

REFLUX is capable of handling nonuniform fine-mesh spacings and nonuniform nodes in the radial and axial directions, as well as irregular reactor geometries. The zero flux, zero current and albedo boundary conditions, described in Appendix D, can be imposed at the reactor surfaces. The diagonal symmetry option is also incorporated into the code.

3.3 TWO-DIMENSIONAL RESULTS: THE EPRI-9 AND EPRI-9R BENCHMARK PROBLEMS

In this section, results from the two-dimensional EPRI-9 and EPRI-9R benchmark reactor problems are presented. The EPRI-9 and EPRI-9R problems model the baffle and reflector regions of PWR's. The core configuration of both problems is similar, except for the presence of 4 control rod clusters in the EPRI-9R problem. The geometry and boundary conditions of both problems are described in Appendix E.

3.3.1 The Reference PDQ-7 Solution

For each benchmark problem, EPRI-9 and EPRI-9R, two numerical standard solutions were obtained using the PDQ-7 computer code. One standard solution was obtained with one mesh box per fuel cell (i.e., 1.4 cm mesh spacing); the other reference solution was obtained with four mesh boxes per fuel cell (i.e., 0.7 cm mesh spacing).

3.3.2 The Nodal QUANDRY Solution

The nodal calculations were performed using the QUANDRY computer code with four square nodes per fuel assembly (i.e., 10.5 cm node width).

The homogenized cross sections and discontinuity factors, input for the QUANDRY code, were obtained through fine-mesh, two-dimensional PDQ-7 assembly and color set calculations. The fine-mesh grid used for these fine-mesh calculations was consistent with the grid used to obtain the reference PDQ-7 solution.

For the EPRI-9 problem, color set calculations involving quarter assembly nodes and neighboring baffle reflector nodes (i.e., color sets A, B, C in Fig. 3-1) were used to determine the homogenized cross sections and discontinuity factors for the nodes on the reflector side of the core-baffle interface. For the fuel nodes, assembly calculations were used to determine the homogenized cross sections and discontinuity factors. Figure 3-2 shows the core layout for the EPRI-9 problem, indicating by "A" the nodes that were homogenized through assembly calculations and indicating by "CS" the nodes that were homogenized through color set calculations.

The values of k_{eff} and assembly power densities corresponding to the reference PDQ-7 solution with one mesh box per fuel cell (i.e., 1.4 cm mesh spacing) are compared in Fig. 3-4 to those values obtained by the nodal QUANDRY calculation. The maximum error obtained for assembly power density was 0.37%. A similar comparison is shown in Fig. 3-5. In this case, the reference solution and fine-mesh local criticality calculations were obtained with four mesh boxes per fuel cell (i.e., 0.7 cm mesh spacing); the maximum relative error in assembly power density was 0.54%.

When assembly calculations, as indicated in Fig. 3-2, were used for all interior nodes of the EPRI-9R problem, then the maximum errors obtained in assembly power density were 2.45% relative to a 1.4 cm mesh spacing, PDQ

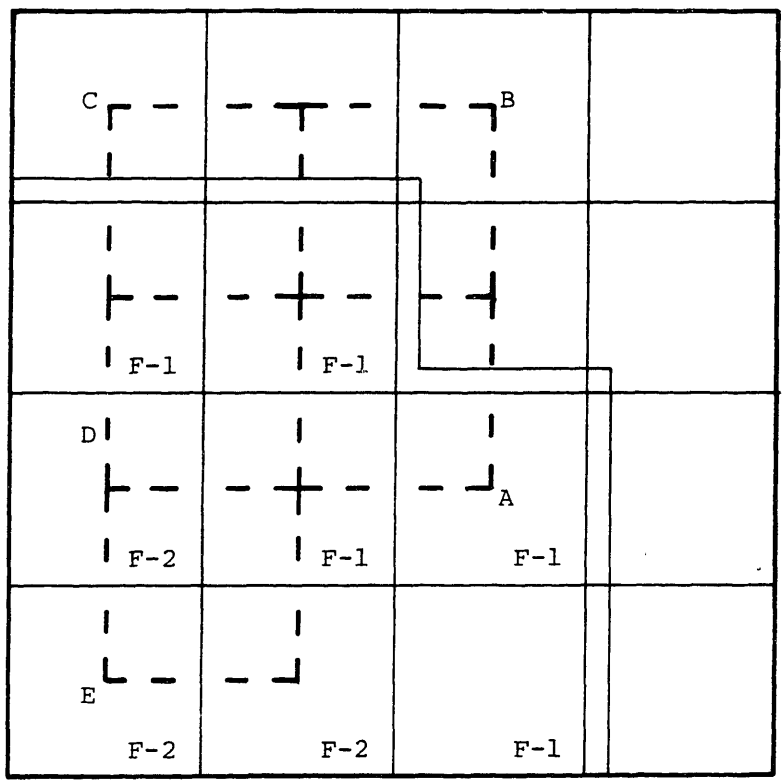

Fig. 3-1. Core layout for the EPRI-9 and EPRI-9R problem showing fuel assemblies F-1, F-2 and color sets A, B, C, D, E superimposed on the core layout using dashed lines.

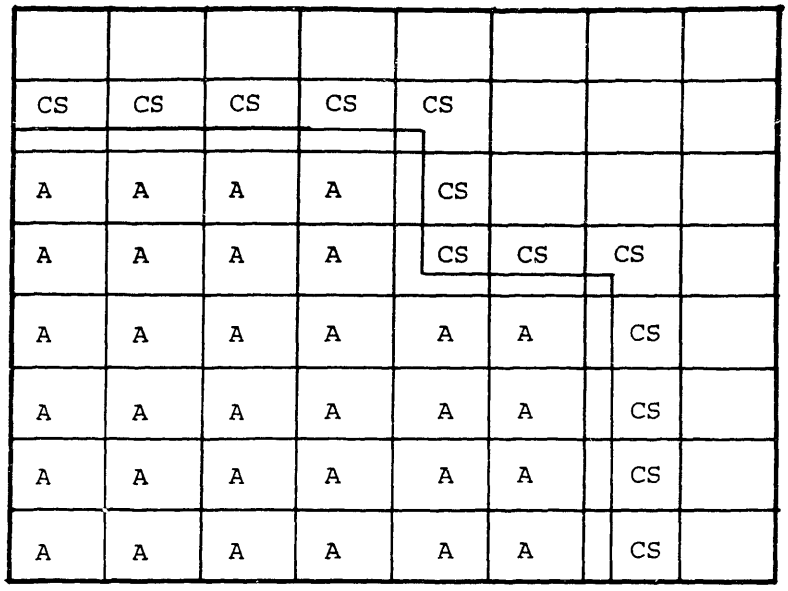

Fig. 3-2. Core layout for the EPRI-9 problem.
"A" = assembly calculation.
"CS" = color set calculation.

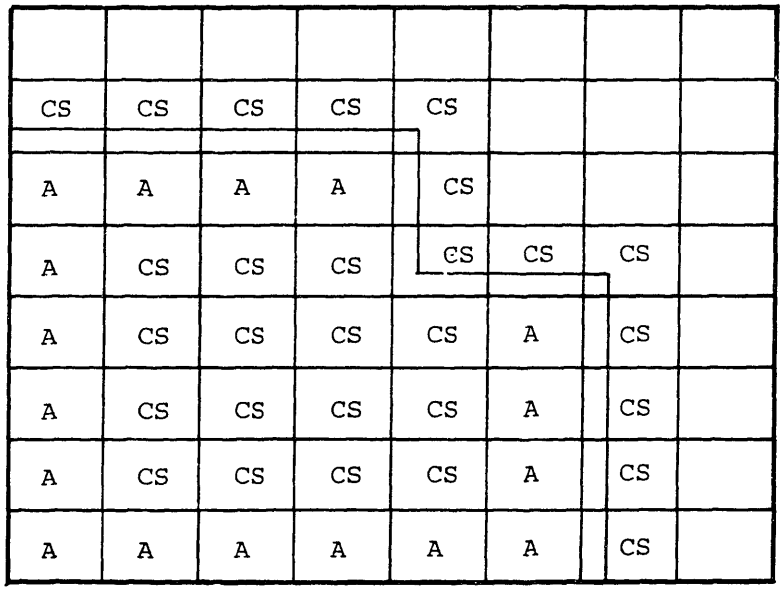

Fig. 3-3. Core layout for the EPRI-9R problem.

0.783290	0.561056	Reference 60 × 60 PDQ-7 solution
0.780462	0.559122	Nodal 8 × 8 QUANDRY
0.36%	0.34%	Relative error
1.12624	1.11673	
1.12884	1.11608	
-0.23%	0.058%	
1.33767		
1.34257		
-0.37%		

k_{eff} (PDQ) = 0.928993
k_{eff} (QUANDRY) = 0.928559
% Error = 0.047%

Fig. 3-4. QUANDRY assembly power errors for the EPRI-9 problem relative to a 60 × 60 PDQ-7 solution.

0.84794	0.60887	Reference 120 × 120 PDQ-7 solution
0.84461	0.60559	Nodal 8 × 8 QUANDRY
0.39%	0.54%	Relative error
1.2176	1.2067	
1.2206	1.2070	
-9.25%	-0.025%	
1.4445		
1.4514		
-0.48%		

k_{eff} (PDQ) = 0.9279977
k_{eff} (QUANDRY) = 0.9275608
% Error = 0.047%

Fig. 3-5. QUANDRY assembly power errors for the EPRI-9 problem relative to a 120 × 120 PDQ-7 solution.

solution. In order to obtain a more accurate nodal solution, it was necessary to use color set calculations for the rodded and neighboring nodes (i.e., color sets A, D, E in Fig. 3-1). Figure 3-3 shows the core nodal layout for calculating the homogenized cross sections and discontinuity factors for the EPRI-9R problem. Note that for the EPRI-9R problem, 7 fine-mesh criticality calculations were required (color sets A, B, C, D, E and assemblies F-1, F-2 in Fig. 3-1), whereas for the EPRI-9 problem, only 5 fine-mesh criticality calculations were required (color sets A, B, D and assemblies F-1, F-2 in Fig. 3-1). The values of k_{eff} and assembly power density predicted by QUANDRY for the EPRI-9R problem are compared in Fig. 3-6 to the 1.4 cm mesh spacing PDQ-7 solution; the maximum error obtained in assembly power density was 0.41%. A similar comparison, when a 0.7 cm mesh spacing was used, is shown in Fig. 3-7. In this case, the maximum relative error in assembly power density was 0.50%.

These results illustrate that for both problems, the EPRI-9 and EPRI-9R, the nodal QUANDRY solution matches quite closely the reference PDQ solution. It should be noticed that the accuracy of the nodal solution changes very little when the mesh spacing is reduced from 1.4 cm to 0.7 cm, provided that the reference solution, the homogenized cross sections and the discontinuity factors are all calculated with the same fine-mesh spacing.

For the unrodded problem, the use of local assembly calculations for the fuel regions is sufficient to obtain very accurate results; however, for the rodded problem it is necessary, in order to achieve equivalent accuracy, to use color set calculations for the rodded and neighboring nodes.

0.851147	0.465213	Reference 60 × 60 PDQ-7
0.847660	0.464506	Nodal 8 × 8 QUANDRY
0.41%	0.15%	Relative error

1.23241	0.620142		k_{eff} (PDQ) = 0.896628
1.23358	0.621190		k_{eff} (QUANDRY) = 0.8962065
-0.09%	-0.17%		% Error = 0.047%
1.67785			
1.68277			
-0.29%			

Fig. 3-6. QUANDRY assembly power errors for the EPRI-9R problem relative to a 60 × 60 PDQ-7 solution.

0.847910	0.472559	Reference 120 × 120 PDQ-7
0.843694	0.470866	Nodal 8 × 8 QUANDRY
0.50%	0.36%	Relative error

1.22547	0.650255		k_{eff} (PDQ) = 0.897297
1.22757	0.650485		k_{eff} (QUANDRY) = 0.896814
-0.17%	-0.035%		% Error = 0.054%
1.65342			
1.66076			
-0.44%			

Fig. 3-7. QUANDRY assembly power errors for the EPRI-9R problem relative to a 120 × 120 PDQ-7 solution.

Accordingly, in order to obscure as little as possible errors due to the reconstruction scheme, the homogenized cross sections and discontinuity factors for the rodded and neighboring nodes were based on color set calculations.

3.3.3 Flux Reconstruction Results

REFLUX has been applied, to reconstruct fine-mesh fluxes, for the EPRI-9 and EPRI-9R benchmark problems. The node face averaged fluxes and node volume averaged fluxes, input data for REFLUX, were obtained by the methods described in the previous section using the QUANDRY code. The assembly functions were obtained by performing zero-current color set calculations.

The node corner point fluxes predicted by REFLUX are compared, in Fig. 3-8, to those values obtained by the 1.4 cm mesh spacing PDQ-7 reference calculation. The maximum relative error for the thermal flux was 3.56%. A similar comparison, when a 0.7 cm mesh spacing was used, is shown in Fig. 3-10. In this case, the maximum relative error for the thermal corner point flux was 4.14%.

A similar study was carried out for the EPRI-9R problem. Figure 3-9 shows the relative errors in corner point fluxes when a 1.4 cm mesh spacing was used. The maximum relative error obtained in the thermal flux was 3.54% Figure 3-11 compares the corner point fluxes when a 0.7 cm mesh spacing was used; in this case, the maximum relative error obtained for the thermal flux was 4.58%.

For interior nodes, the maximum error in the thermal corner point flux was 0.63% in the EPRI-9 problem, and 1.31% in the EPRI-9R problem.

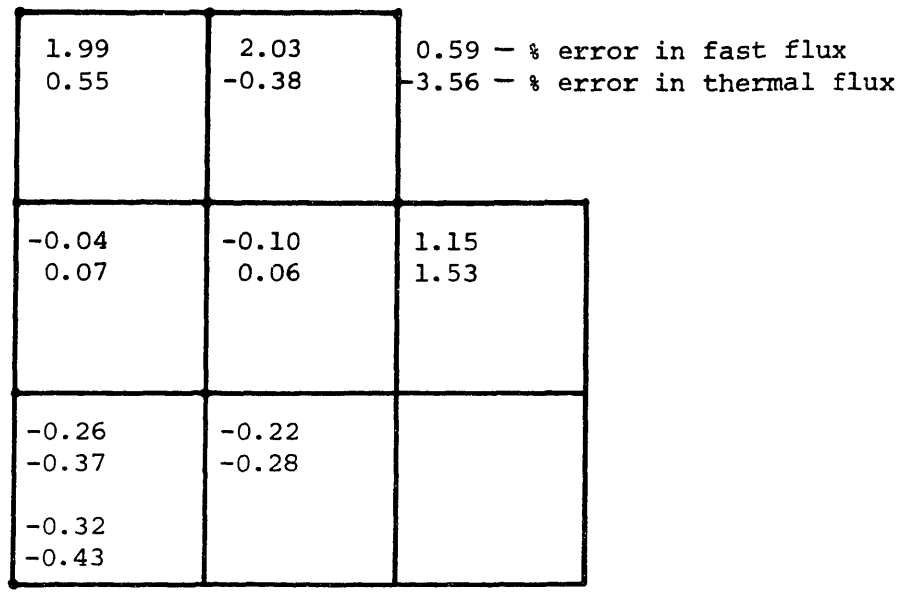

Fig. 3-8. Corner point flux errors for the EPRI-9 problem relative to a 60 × 60 PDQ-7 solution.

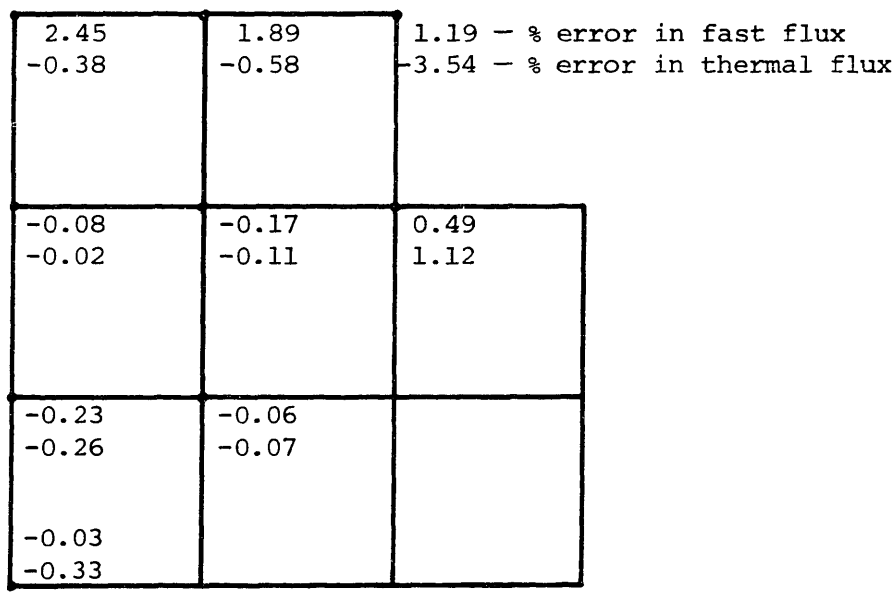

Fig. 3-9. Corner point flux errors for the EPRI-9R problem relative to a 60 × 60 PDQ-7 solution.

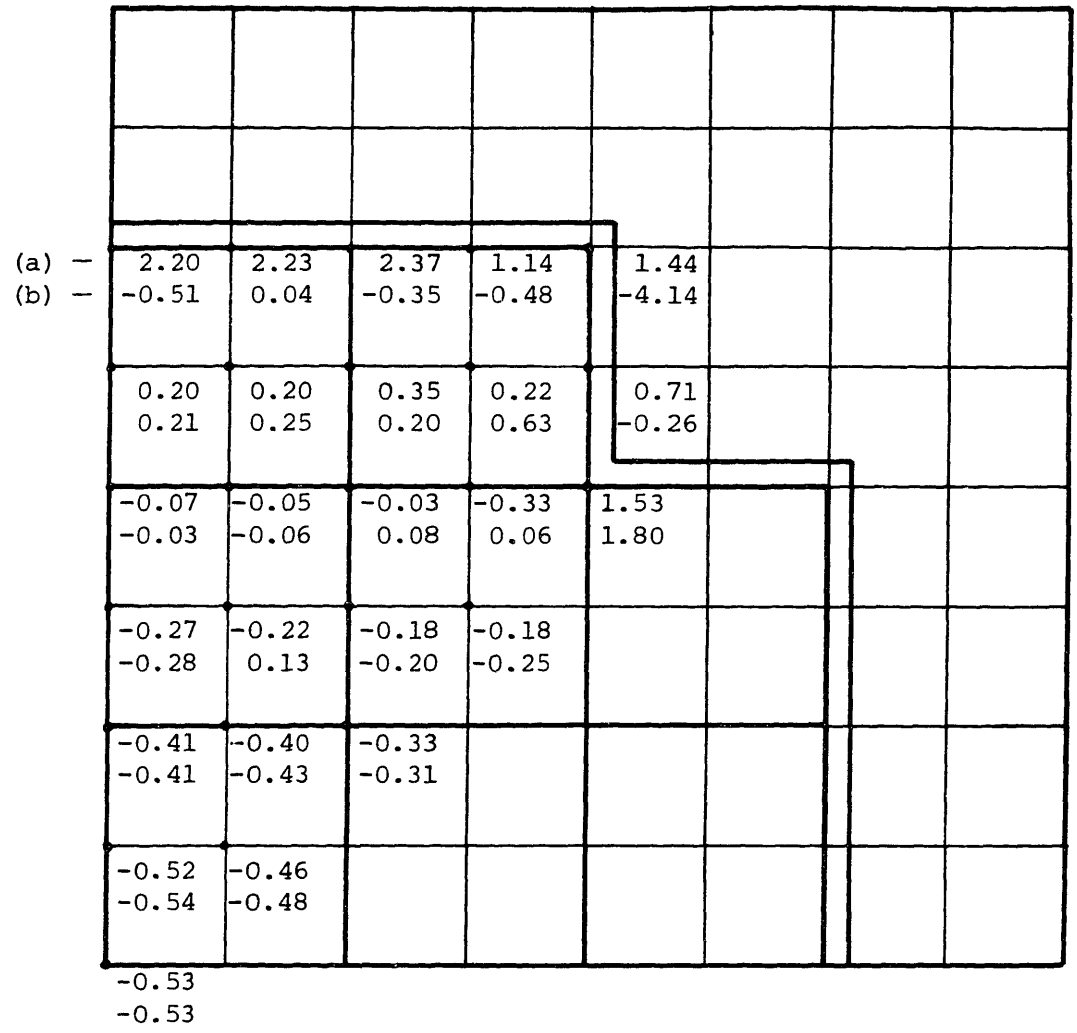

Fig. 3-10. Corner point flux errors for the EPRI-9 problem relative to a 120 × 120 PDQ-7 solution.

(a) = % error in fast flux

(b) = % error in thermal flux

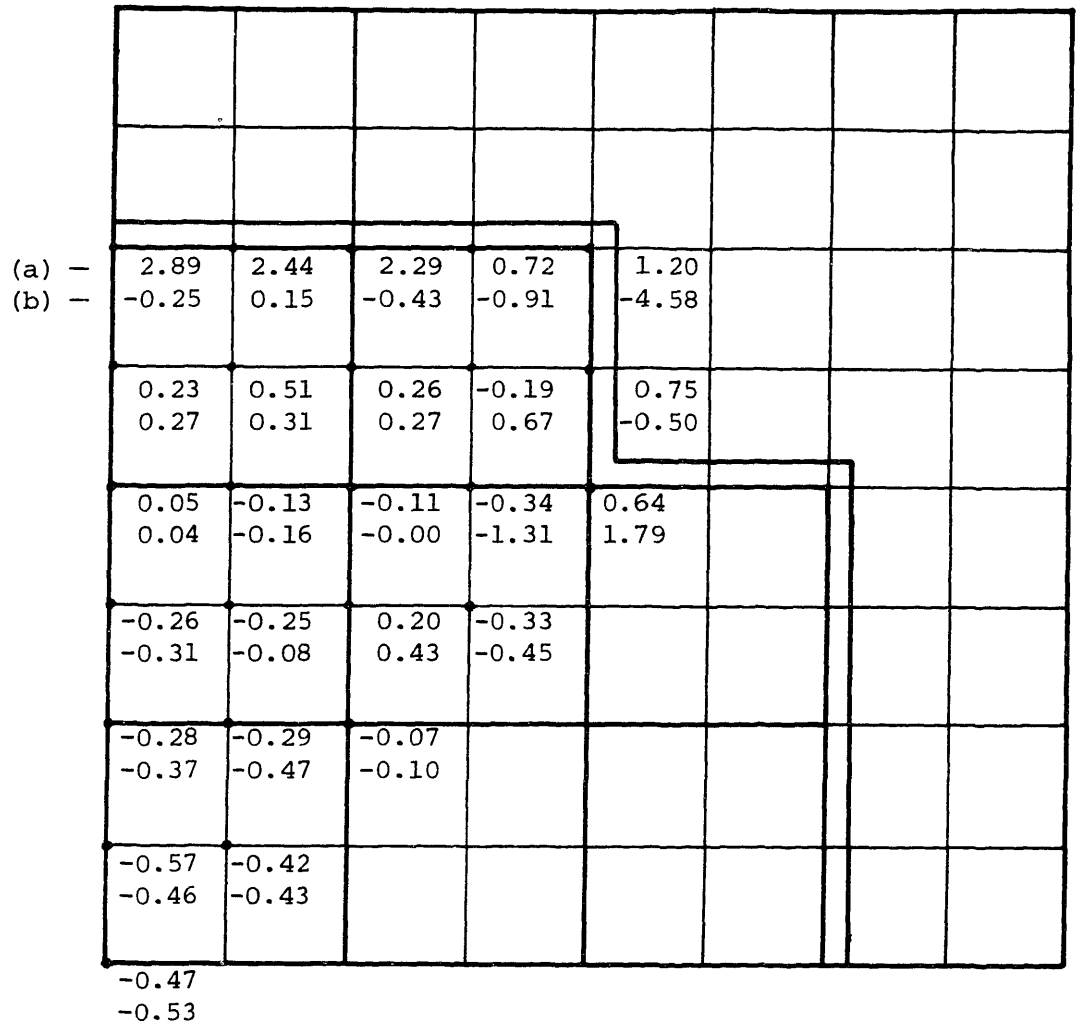

Fig. 3-11. Corner point flux errors for the EPRI-9R problem relative to a 120 × 120 PDQ-7 solution.

(a) = % error in fast flux

(b) = % error in thermal flux

These results illustrate that, for both problems and for interior nodes, REFLUX predicts very accurately corner point fluxes. The maximum relative errors obtained in the problems examined appeared at the core-baffle interface, where the assembly power is lower. It can also be noticed that the accuracy of the flux reconstruction scheme was barely altered when the PDQ mesh spacing was changed.

3.4 THREE-DIMENSIONAL RESULTS: THE 3-D-EPRI-9 BENCHMARK PROBLEM

In this section, results for the three-dimensional EPRI-9 benchmark problem are presented. The 3D-EPRI-9 problem is a three-dimensional PWR with four rod clusters partially inserted. The unrodded radial section is identical to that of the EPRI-9 problem, and the rodded radial section is identical to that of the EPRI-9R problem. The reactor geometry is described in Appendix E.

3.4.1 The Reference PDQ-7 Solution

For this problem, a numerical PDQ-7 reference solution was obtained from Northeast Utilities. A 1.4 cm square radial grid was employed to obtain the reference solution. The mesh grid used in the axial direction is shown in Table E-2. Albedo boundary conditions equivalent to an infinite water reflector were assumed for the top and bottom reactor axial surfaces; the albedo coefficients are given in Appendix E.

3.4.2 The Nodal QUANDRY Solution

The node-face-averaged fluxes and node-volume-averaged fluxes were calculated using the QUANDRY code with four nodes per fuel assembly in the

radial plane and six nodes in the axial direction. Figure 3-12 shows the axial nodal mesh layout. In order to reconstruct more accurately the point fluxes at mesh points near the water reflector, it was necessary to consider a smaller axial length for the nodes at the reactor axial surfaces. This fact will be discussed in the next section. The homogenized cross sections and discontinuity factors for the nodes in the unrodded region were evaluated from two-dimensional assembly and color set calculations, as is indicated in Fig. 3-2. For the nodes in the rodded region, the homogenized parameters were obtained according to the pattern shown in Fig. 3-3. Unity discontinuity factors were assumed for the axial direction.

The values of k_{eff} and nodal power density predicted by the QUANDRY solution are compared in Fig. 3-13 to those obtained by the PDQ-7 calculation. For simplicity, the 8×8 radial nodes have been collapsed to 4×4 nodes, and the 6 axial nodes to 4 nodes of 15.0 cm width. The maximum error obtained for nodal power density was 0.74%.

These results indicate that, for the 3D-EPRI-9 problem, the nodal solution is very accurate.

3.4.3 Flux Reconstruction Results

REFLUX has been applied, to reconstruct fine-mesh fluxes, to the 3D-EPRI-9 benchmark problem. The nodal averaged values were calculated, as was described in the previous section, using the QUANDRY code. The assembly functions were obtained by performing two-dimensional, zero-current, color set calculations.

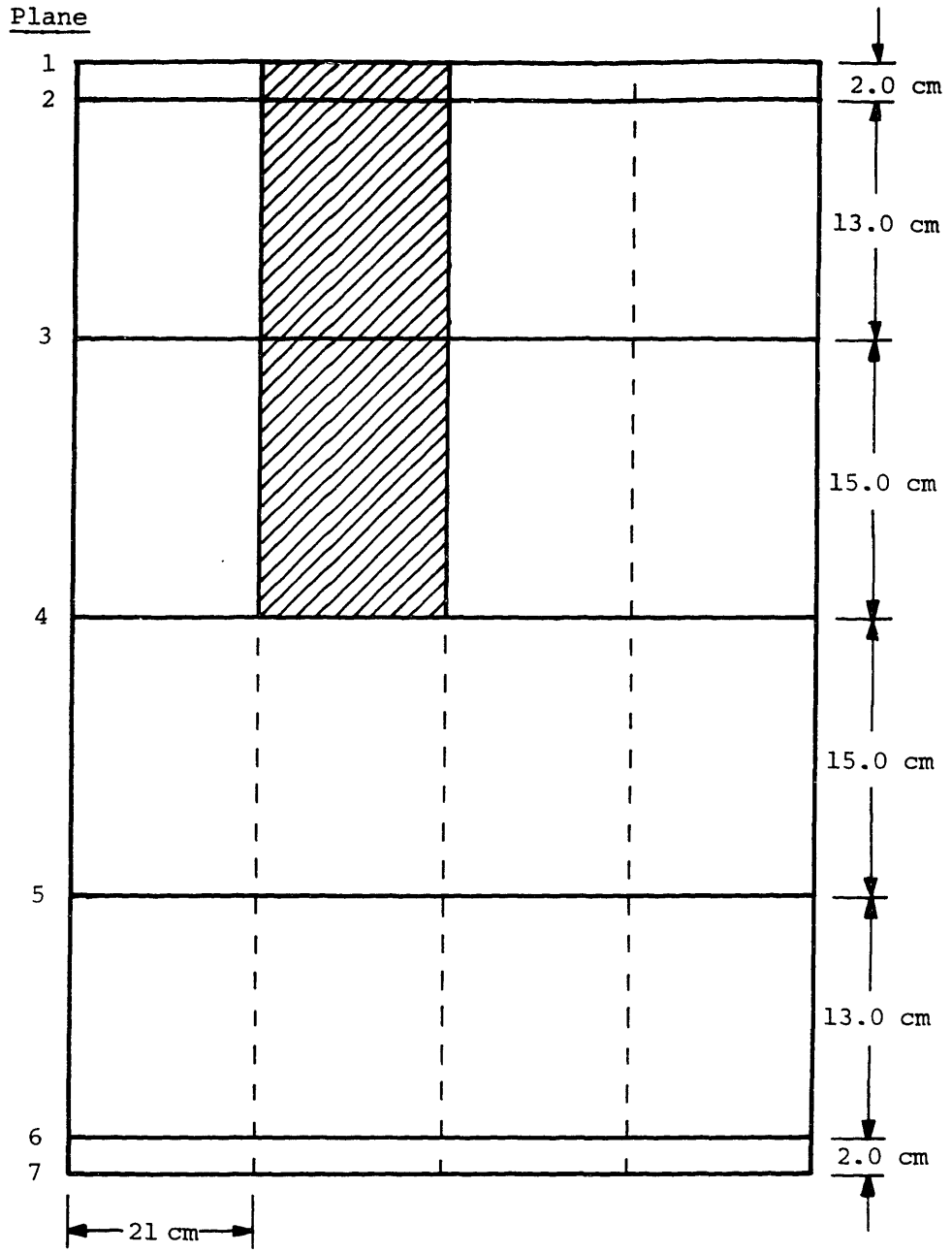

Fig. 3-12. Axial nodal layout for obtaining the QUANDRY solution for the 3D-EPRI-9 benchmark reactor problem.

k_{eff} (PDQ) = 0.841384
k_{eff} (QUANDRY) = 0.841122
} % Error = 0.031

Plane #1 (Top)

0.613296 0.609301 0.65%	0.350681 0.348580 0.60%	— (60×60)×34 PDQ — (8×8)×6 QUANDRY — % Error
0.845655 0.845404 0.03%	0.449983 0.451840 -0.41%	
1.10323 1.10564 -0.22%		

Plane #2 (Rodded)

0.975073 0.971221 0.40%	0.585999 0.584813 0.20%	
1.35980 1.36226 -0.18%	0.790343 0.796205 -0.74%	
1.74067 1.74683 -0.35%		

Plane #3

1.03365 1.02909 0.44%	0.676680 0.675426 0.19%	
1.46587 1.47024 -0.30%	1.30216 1.30966 -0.58%	
1.80615 1.81210 -0.33%		

Plane #4 (Bottom)

0.707906 0.703132 0.67%	0.484282 0.481506 0.57%	
1.00404 1.00561 -0.16%	0.975006 0.976120 -0.11%	
1.20881 1.21121 -0.20%		

Fig. 3-13. QUANDRY assembly power errors for the 3D-EPRI-9 problem relative to a (60 × 60) × 34 PDQ-7 solution.

When only four axial nodes of length 15.0 cm were considered, the maximum error obtained for the corner point thermal flux was 24.8% for a corner point located at the reactor axial surface in the core-baffle interface. For interior nodes, the maximum error obtained in the corner point thermal flux was 0.65%.

The presence of the top and bottom axial reflectors makes the thermal flux behave exponentially in the axial direction near the core-reflector interface; thus, for these points, a bi-quadratic shape is a poor approximation. If the axial length of the nodes near the axial reflector is reduced, the accuracy in estimating the reconstructed flux is improved. Thus, in order to obtain more accurate point fluxes at mesh points near the water reflector, nodes of 2.0 cm axial length were considered for the nodes adjacent to the reactor axial surfaces.

The node corner point fluxes predicted by REFLUX are compared in Figs. 3-14 and 3-15, with those values obtained from the reference calculation. The location of the radial planes shown in Figs. 3-14, 3-15 is given in Fig. 3-12. The maximum relative error for the thermal flux was 7.5% for a corner point located at the reactor axial surface in the core-baffle interface. For interior nodes, the maximum error obtained in the corner point thermal flux was 0.65%.

These results indicate that, for interior nodes, REFLUX predicts very accurately the corner point fluxes. However, for points near the reactor axial surfaces, the results are not very accurate. If the number of axial nodes near the axial reflectors is increased, the accuracy in estimating the reconstructed flux is improved. However, in many practical applications, very accurate values of the neutron flux at points near the axial water reflector, where the power is low, are not required.

Plane #1 (Top)

3.29 7.33	3.14 7.24	1.38 6.93
0.40 0.94	0.60 0.29	1.30 4.60
0.31 0.67 -0.05 0.48	0.79 0.13	

Plane #2 (Rodded)

3.26 5.54	2.92 5.35	2.38 5.29
0.62 -0.18	0.38 -0.53	1.21 3.94
0.25 0.40 0.10 -0.62	0.50 -0.65	

Plane #3 (Rodded)

3.19 -0.56	2.42 -0.92	2.05 -1.78
0.07 0.46	0.04 0.43	0.45 0.42
-0.32 -0.00 -0.03 -0.18	0.22 0.38	

Plane #4 (Rodded)

3.09 -0.23	2.78 -0.49	2.20 -3.09
0.00 0.15	-0.04 0.15	0.99 1.19
-0.15 -0.29 -0.24 -0.27	-0.23 0.03	

Fig. 3-14. Corner point flux errors for the 3D-EPRI-9 problem relative to a (60 × 60) × 34 PDQ-7 solution (Planes #1, 2, 3, 4).

Plane #5

2.72 -0.41	2.96 -0.46	2.86 -1.25
0.06 0.37	0.08 0.21	1.25 1.26
-0.16 0.15 0.25 0.02	-0.39 0.05	

Plane #6

3.26 5.57	3.38 5.65	2.11 5.80
0.16 0.04	0.46 -0.21	1.76 5.04
0.00 -0.54 -0.03 -0.60	-0.26 -0.64	

Plane #7 (Bottom)

3.35 7.50	3.34 7.44	2.07 7.43
0.78 0.90	0.84 0.93	2.11 5.57
0.21 0.47 0.24 0.57	-0.16 0.63	

Fig. 3-15. Corner point flux errors for the 3D-EPRI-9 problem relative to a (60 x 60) x 34 PDQ-7 solution (Planes #5, 6, 7).

3.4.4 Power Reconstruction Results

The pointwise averaged power was reconstructed along the fine-mesh points corresponding to axial mesh lines L_1, L_2, R_1, R_2, R_3, R_4. Axial mesh lines L_1, L_2 are located in the unrodded area; axial mesh lines R_1, R_2, R_3, R_4 are located in the rodded area. Figure 3-16 indicates the location of all these lines. The pointwise average power along mesh lines L_1, L_2 predicted by REFLUX is compared in Table 3-1 with the pointwise average power from the reference solution. Line L_1 is located in the baffle-core interface corresponding to radial fine-mesh point (15,0). Line L_2, located in the most interior node at radial mesh point (56,4), contains the mesh point where the pointwise average power is highest. Figure 3-17 contains a graphical representation of Table 3-1. Note that all power values are normalized so that the power per unit volume of the entire reactor is unity.

These results illustrate that for lines L_1, L_2 and mesh points corresponding to inside nodes, the reconstructed power reproduces quite closely the reference solution. In fact, for points more than 4 cm distant from the reactor axial surfaces, the maximum relative error in pointwise average power was 2.24% for mesh point in line L_1 and axial plane 25, and 1.95% for mesh point in line L_2 and axial plane 8. It is important to notice that the maximum reactor pointwise averaged power, which corresponds to the mesh points on line L_2 and axial planes 18 and 19, were predicted with a relative error of 0.42%. It can be observed in Fig. 3-17 that the reference averaged power density behaves exponentially within the last axial reactor node, whereas the reconstructed power has a quadratic polynomial shape within any reactor node. This is the reason

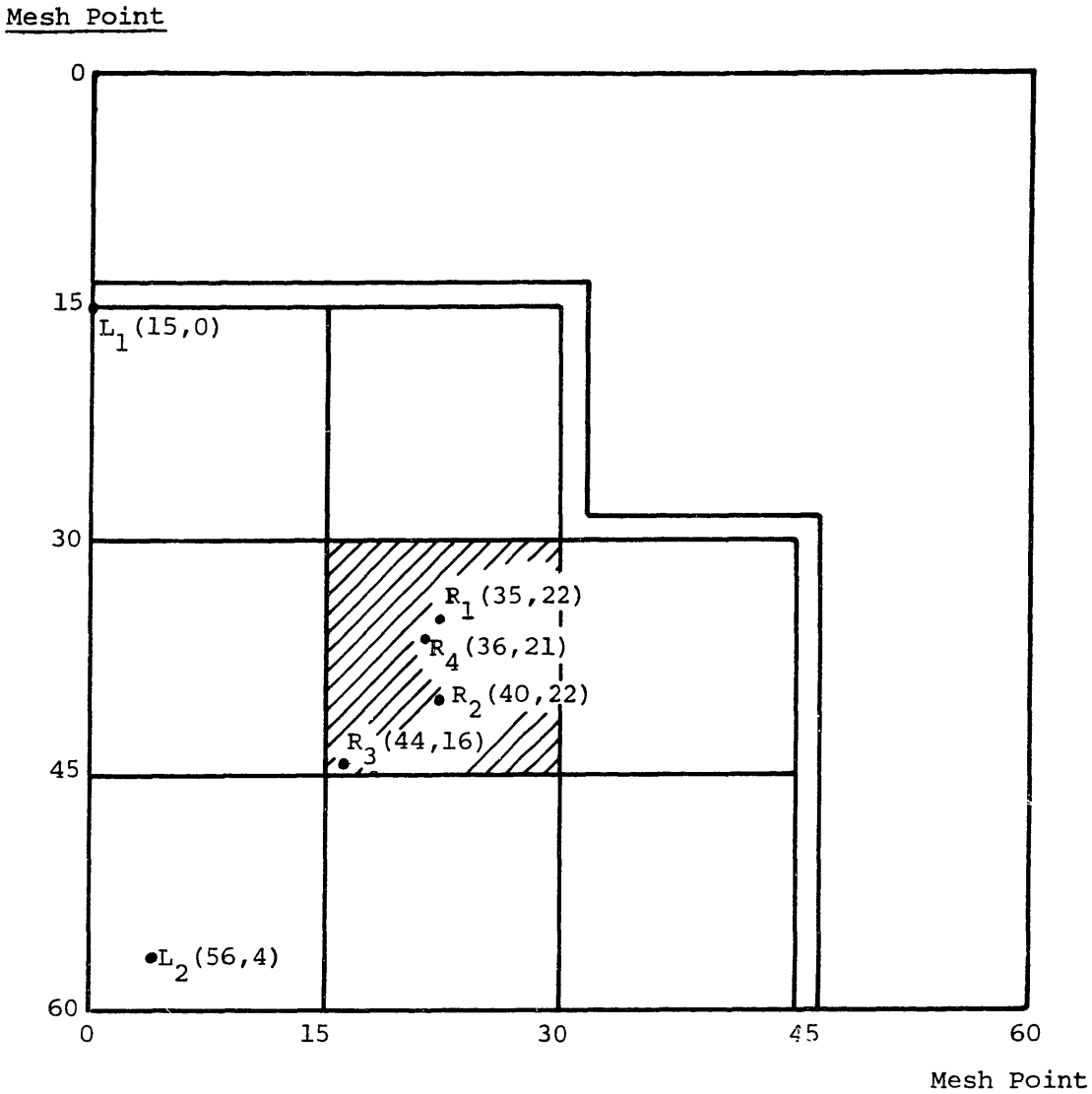

Fig. 3-16. Radial location of axial mesh lines L_1, L_2, R_1, R_2, R_3, R_4 where the pointwise power has been reconstructed.

Table 3-1. Pointwise average power for axial mesh lines L_1 and L_2

Node No.	Plane No.	Line L_1 (15,0)			Line L_2 (56,4)		
		PDQ	REFLUX	% Error	PDQ	REFLUX	% Error
	1	0.297	0.277	6.73	1.22	1.27	-4.09
1	2	0.259	0.238	8.10	1.13	1.17	-3.54
	3	0.233	0.212	9.01	1.08	1.11	-2.78
- - -	4	0.211	0.200	5.21	1.04	1.06	1.85
	5	0.217	0.221	-1.84	1.11	1.16	-4.5
	6	0.242	0.244	-0.83	1.25	1.27	-1.6
2	7	0.272	0.268	1.47	1.39	1.39	0.0
	8	0.300	0.294	2.00	1.54	1.51	1.95
	9	0.328	0.321	2.13	1.68	1.65	1.79
- - -	10	0.366	0.365	0.27	1.86	1.87	-0.54
	11	0.398	0.397	0.25	2.03	2.04	-0.49
	12	0.433	0.430	0.69	2.20	2.21	-0.45
3	13	0.446	0.443	0.67	2.26	2.27	-0.44
	14	0.456	0.453	0.66	2.31	2.32	-0.43
	15	0.463	0.461	0.43	2.34	2.35	-0.43
	16	0.466	0.464	0.46	2.35	2.36	-0.43
- - -	17	0.468	0.466	0.43	2.36	2.36	0.0
	18	0.468	0.466	0.43	2.36	2.37	-0.42
	19	0.468	0.466	0.43	2.36	2.37	-0.42
4	20	0.466	0.463	0.64	2.34	2.35	-0.43
	21	0.460	0.457	0.65	2.31	2.32	-0.43
	22	0.451	0.448	0.67	2.26	2.27	-0.44
	23	0.423	0.421	0.47	2.11	2.12	-0.47
- - -	24	0.394	0.392	0.51	1.96	1.97	-0.51
	25	0.357	0.349	2.24	1.78	1.75	1.69
	26	0.329	0.322	2.13	1.64	1.61	1.83
5	27	0.299	0.295	1.34	1.49	1.48	0.67
	28	0.269	0.270	-0.37	1.34	1.36	-1.49
	29	0.242	0.246	-1.65	1.20	1.25	-4.17
- - -	30	0.235	0.223	5.10	1.12	1.14	-1.79
	31	0.261	0.237	9.19	1.16	1.19	-2.59
	32	0.289	0.265	8.30	1.22	1.27	-4.10
	33	0.332	0.309	6.93	1.32	1.37	-3.79

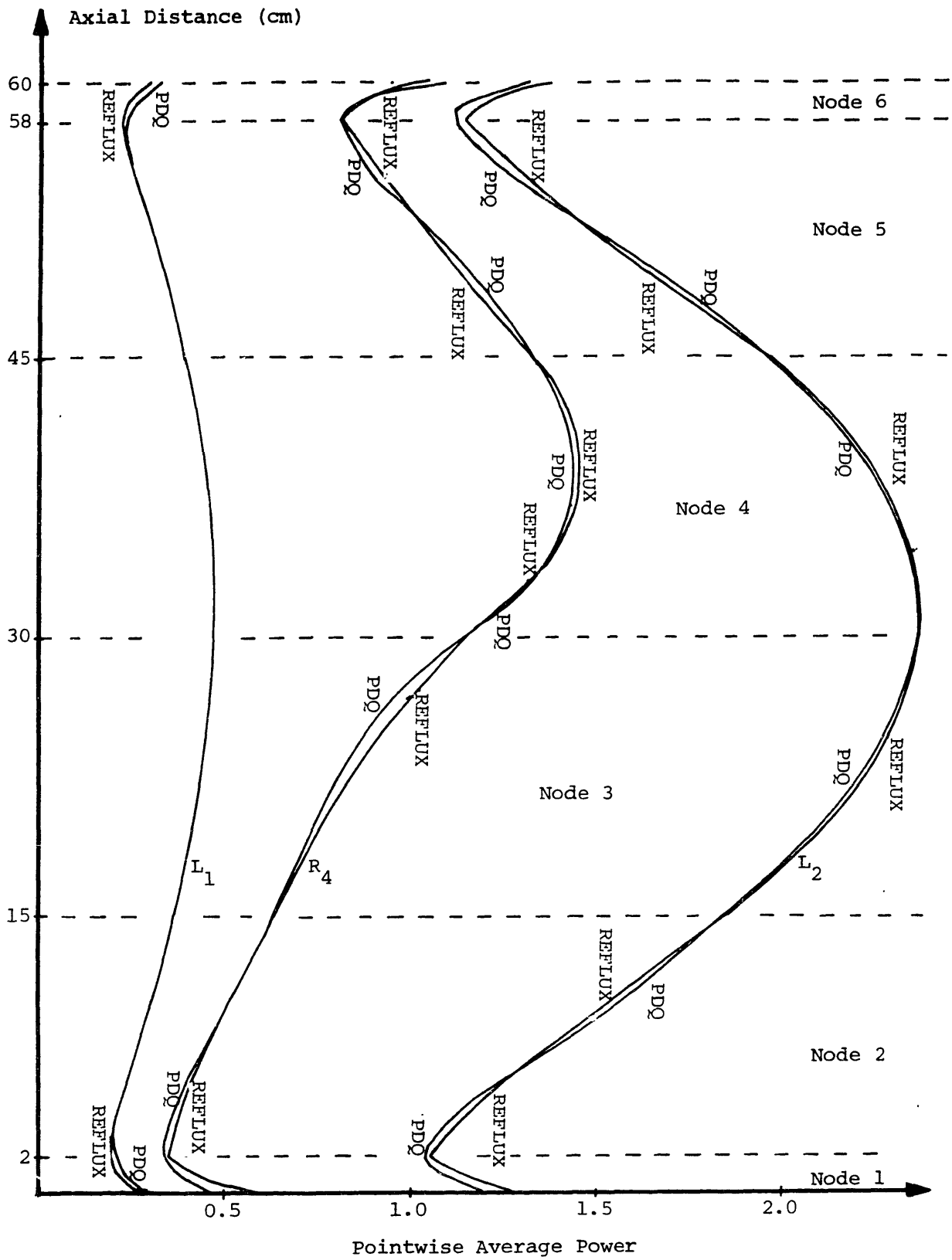

Fig. 3-17. Pointwise average power for axial mesh lines L_1, L_2, R_4.

why the reference pointwise average power is not very accurately predicted for the last axial reactor node of axial length 2.0 cm.

Axial mesh lines R_1, R_2, R_3, R_4 are located at radial mesh points (35,22), (40,22), (44,16), (36,21), respectively. These mesh lines pass through the control rod cluster. The presence of a control rod partially inserted causes the assembly function, $\psi^{i,j,k}(x,y)$, to be discontinuous in the Z direction at the control rod radial surface (axial plane 17 and shadowed node in Fig. 3-16). Thus, pointwise average powers at the control rod radial surface can be evaluated either with information from the nodes in the rodded area or with information from the nodes in the unrodded area. As a result, two different values of the pointwise average power are available for each mesh point at the control rod radial surface. When the pointwise average power was calculated using only the information from the nodes in the rodded area, relative errors of 8.3%, 8.8%, 6.6% and 15.8% were obtained for the axial mesh lines R_1, R_2, R_3, R_4 at the rod radial surface. Similar errors, but with opposite signs, were obtained for the same points, when the power was reconstructed using only the information from the nodes in the unrodded area. When an arithmetic average of the power predicted from both calculations was taken, for the points in axial mesh lines R_1, R_2, R_3, R_4 at the node radial surface, relative errors in pointwise averaged power of 1.85%, 1.60%, 2.76% and 0.00% were obtained for these points. Accordingly, a special normalization scheme, consistent with the overall reconstruction process, was developed for calculating pointwise average powers along axial mesh lines inside control rods partially inserted. This scheme is presented in Appendix F.

The pointwise average power along axial mesh lines R_1, R_2 is compared in Table 3-2 with that from the reference solution. Table 3-3 compares the same values for axial mesh lines R_3, R_4. Figure 3-17 contains a graphical representation of the pointwise average powers for axial mesh line R_4.

These results illustrate that the reconstructed power is predicted very accurately for mesh lines R_1, R_2, R_3, R_4 and mesh points corresponding to inside nodes. For points more than 4 cm distant from the reactor axial surfaces, the maximum relative errors in pointwise average power was 4.21%, 2.79%, 2.84% and 4.02% for axial mesh lines R_1, R_2, R_3, R_4. These results are very encouraging, in view of the fact that the reference pointwise average power does not behave like a quadratic function near the control rod tip. In fact, when a quadratic polynomial function was forced to reproduce exactly the reference fine-mesh powers at the end points of the node axial mesh line, and to reproduce exactly the reference mesh line average power, maximum errors of 2.54%, 1.11% and 3.02% were obtained for axial mesh lines R_2, R_3, R_4.

As it has been already discussed, maximum errors appear near the reactor axial surfaces, where the presence of a water reflector makes the power behave exponentially.

Table 3-2. Pointwise average power for axial mesh lines R_1 and R_2

Node No.	Plane No.	Line R_1 (35,22)			Line R_2 (40,22)		
		PDQ	REFLUX	% Error	PDQ	REFLUX	% Error
	1	0.447	0.527	-17.9	0.536	0.626	-16.8
1	2	0.390	0.441	-13.1	0.468	0.522	-11.5
	3	0.353	0.380	-7.65	0.424	0.449	-5.90
- - -	4	0.321	0.337	-4.98	0.385	0.401	-4.16
	5	0.337	0.363	-7.72	0.405	0.428	-5.68
	6	0.381	0.395	-3.67	0.456	0.463	-1.54
2	7	0.430	0.432	-0.47	0.514	0.507	1.36
	8	0.479	0.475	0.84	0.573	0.557	2.79
	9	0.528	0.523	0.95	0.630	0.616	2.22
- - -	10	0.599	0.606	-1.17	0.714	0.719	-0.70
	11	0.669	0.676	-1.05	0.794	0.791	0.38
	12	0.764	0.786	-2.88	0.901	0.911	-1.11
3	13	0.817	0.847	-3.67	0.959	0.980	-2.19
	14	0.878	0.915	-4.21	1.03	1.06	-2.91
	15	0.959	0.986	-2.82	1.12	1.14	-1.79
	16	1.01	1.02	-0.99	1.18	1.18	0.00
- - -	17	1.08	1.06	1.85	1.25	1.23	1.60
	18	1.15	1.12	2.61	1.33	1.30	2.26
	19	1.21	1.18	2.48	1.39	1.36	2.16
4	20	1.28	1.26	1.56	1.45	1.46	-0.69
	21	1.33	1.32	0.75	1.52	1.53	-0.66
	22	1.34	1.36	1.49	1.54	1.56	-1.30
	23	1.31	1.34	-2.29	1.50	1.54	-2.67
- - -	24	1.25	1.26	-0.80	1.42	1.43	-0.70
	25	1.15	1.13	1.74	1.31	1.29	1.53
	26	1.07	1.05	1.87	1.22	1.20	1.64
5	27	0.984	0.975	0.91	1.11	1.11	0.00
	28	0.890	0.904	-1.57	1.01	1.03	-1.98
	29	0.803	0.836	-4.11	0.907	0.950	-4.74
- - -	30	0.767	0.772	-0.65	0.865	0.875	-1.16
	31	0.824	0.816	0.97	0.929	0.926	0.32
6	32	0.892	0.884	0.90	1.01	1.01	0.00
	33	0.999	0.985	1.40	1.13	1.12	0.88

Table 3-3. Pointwise average power for axial mesh lines R_3 and R_4

Node No.	Plane No.	Line R_3 (44,16)			Line R_4 (36,21)		
		PDQ	REFLUX	% Error	PDQ	REFLUX	% Error
	1	0.905	0.925	-2.21	0.475	0.591	-24.4
1	2	0.806	0.813	-0.87	0.414	0.478	-15.5
	3	0.743	0.737	0.81	0.374	0.401	-7.21
- - -	4	0.691	0.695	-0.58	0.339	0.356	-5.01
	5	0.715	0.760	-6.29	0.356	0.382	-7.30
	6	0.820	0.832	-1.46	0.402	0.414	-2.99
2	7	0.920	0.911	0.98	0.454	0.452	0.44
	8	1.02	0.997	2.25	0.506	0.498	1.58
	9	1.12	1.09	2.68	0.557	0.549	1.44
- - -	10	1.25	1.25	0.00	0.632	0.639	-1.11
	11	1.38	1.35	2.17	0.705	0.698	0.99
	12	1.52	1.51	0.66	0.803	0.809	-0.75
3	13	1.59	1.59	0.00	0.858	0.879	-2.45
	14	1.65	1.68	-1.82	0.921	0.958	-4.02
	15	1.72	1.76	-2.33	1.01	1.05	-3.96
	16	1.76	1.81	-2.84	1.07	1.09	-1.87
- - -	17	1.81	1.86	-2.76	1.14	1.14	0.00
	18	1.85	1.88	-1.62	1.22	1.21	0.82
	19	1.89	1.90	-0.53	1.29	1.26	2.33
4	20	1.93	1.93	0.00	1.37	1.35	1.46
	21	1.94	1.94	0.00	1.41	1.41	0.00
	22	1.93	1.93	0.00	1.43	1.45	-1.40
	23	1.84	1.84	0.00	1.40	1.43	-2.14
- - -	24	1.73	1.73	0.00	1.33	1.34	-0.75
	25	1.58	1.55	1.90	1.22	1.20	1.64
	26	1.46	1.44	1.37	1.14	1.12	1.75
5	27	1.34	1.33	0.75	1.04	1.04	0.00
	28	1.20	1.23	-2.5	0.944	0.961	-1.80
	29	1.08	1.13	-4.63	0.851	0.887	-4.23
- - -	30	1.03	1.03	0.0	0.812	0.818	-0.74
	31	1.10	1.07	2.73	0.872	0.865	0.80
6	32	1.18	1.16	1.69	0.943	0.937	0.64
	33	1.32	1.28	3.03	1.09	1.04	4.59

3.5 NUMERICAL CONSIDERATIONS

In this section, the computational efficiency of the REFLUX computer code, for the EPRI-9 and 3D-EPRI-9 benchmark reactor problems, is examined.

Table 3-4 contains the total CPU time consumed by QUANDRY and REFLUX when applied to the EPRI-9 and 3D-EPRI-9 benchmark problems. The total CPU time is calculated from the point at which input data have been read, to the point at which solution editing begins. The execution times spent in the major computational processes have also been included in this table. However, the execution time consumed in generating the homogenized cross sections and discontinuity factors, input data for the QUANDRY, has been excluded. The total execution time for REFLUX is the CPU time consumed from the point at which all data have been read to the point at which the corner point fluxes and node line averaged fluxes have been calculated. The total REFLUX execution time does not include the time involved in obtaining the assembly function, input data for the code, nor the time spent in computing, by applying Eq. 2-7, the pointwise reconstructed flux and pointwise power at every reactor fine-mesh point.

All computations were performed on an IBM 3033N computer. QUANDRY was compiled under the IBM compiler with an optimization level of two. REFLUX was compiled with no optimization.

Table 3-4 also contains the number of unknowns, the number of outer Gauss-Seidel iterations and the convergency level reached in solving the REFLUX equations. In all the benchmark problems analyzed, it was verified that convergency occurred most rapidly when one inner iteration for the corner point balance equations and one for the node line balance equations was performed for every outer iteration.

Table 3-4. Execution times and numerical considerations for the EPRI-9 and 3D-EPRI-9 problems.

	PROBLEM NAME	EPRI-9	EPRI-9	3D-EPRI-9	3D-EPRI-9
	NODAL LAYOUT	8 × 8	8 × 8	8 × 8 × 4	8 × 8 × 6
CODE	FINE MESH SPACING	1.4 cm	0.7 cm	1.4 cm	1.4 cm
QUANDRY	1. EXECUTION TIMES (CPU-sec)				
	1.1. Initializations	0.01	0.01	0.01	0.01
	1.2. Geometry Processing	0.87	0.90	1.29	1.34
	1.3. Matrix Coefficients	0.09	0.09	0.56	0.87
	1.4. Iterations	1.13	1.09	5.96	10.14
	1.5. Total Execution Time	2.10	2.09	7.82	12.36
REFLUX	2. NUMERICAL CONSIDERATIONS				
	2.1. Number of Unknowns	36	36	644	916
	2.2. # of Outer Iterations	6	7	10	20
	2.3. Convergence	6.26E-05	3.63E-05	6.69E-05	7.00E-05
	3. EXECUTION TIMES (CPU-sec)				
	3.1. Initializations	0.01	0.01	0.10	0.15
	3.2. Polynomial Coefficients	0.02	0.03	0.12	0.12
	3.3. Balance Eqs. Coefs.	0.03	0.04	2.51	3.40
	3.4. Iterations	0.02	0.02	0.97	2.76
	3.5. Total Execution Time	0.08	0.10	3.70	6.43
Q + R	4. QUANDRY + REFLUX (CPU-sec)				
	4.1. Execution Time	2.18	2.19	11.52	18.79*

*The total execution time for calculating the (60 × 60) × 34 mesh point PDQ-7 reference solution was 96.69 minutes in an IBM 3033 computer.

At present, the preparation of the QUANDRY and REFLUX input data must be done by hand; thus the manpower requirements to obtain the REFLUX solution are substantial. Machine CPU execution time in preparing the input data is, however, small. For the 3D-EPRI-9 problem, the CPU execution time to obtain the assembly function and homogenized cross sections from PDQ-7 local criticality calculations was about 20 seconds, and about 15 seconds to obtain the discontinuity factors. 12.36 seconds were required to run QUANDRY and 6.43 seconds to obtain the corner point fluxes and node line averaged fluxes, and about 10 seconds to edit, for every reactor mesh point, the pointwise flux and pointwise power. Thus, for the 3D-EPRI-9 problem, a total CPU execution time of about one minute was required to generate the input data, and to reconstruct the fine-mesh flux and power.

The total execution time for generating the $(60 \times 60) \times 34$ mesh point PDQ-7 reference solution in an IBM 3033N computer was 96.69 minutes. A finer $(120 \times 120) \times 34$ mesh point PDQ-7 reference solution could not be obtained with an IBM 3033N without exceeding the computer storage capacity.

When 4 axial nodes of length 15 cm were considered for the 3D-EPRI-9 problem, only 10 outer iterations were required to solve the REFLUX equations; however, when the top and bottom axial nodes were divided into two nodes of lengths 2 cm and 13 cm (see Fig. 3-12), 20 iterations were necessary to solve those equations, and the CPU execution time for the QUANDRY run increased from 7.82 seconds to 12.36 seconds, and for the REFLUX run from 3.70 seconds to 6.43 seconds. These results can be explained by the fact that when the reactor nodes have very different dimensions, the properties of the QUANDRY and REFLUX matrices that guarantee successful convergence are worsened.

For the two-dimensional EPRI-9 problem, the reduction of the mesh spacing from 1.4 cm to 0.7 cm increased the execution time consumed in calculating the corner point fluxes by an insignificant amount.

3.6 SUMMARY

In this chapter, results of two- and three-dimensional benchmark reactor problems were presented. The Form Function Method was shown to be quite accurate and efficient for reconstructing the reactor pointwise flux and pointwise power when a nodal solution is known. It was also shown that the Form Function Method requires solving significantly fewer equations than does the conventional finite difference method to achieve the same order of accuracy. The reconstruction scheme was also demonstrated to be computationally about two orders of magnitude faster than finite difference methods.

Chapter 4

SUMMARY AND CONCLUSIONS

4.1 OVERVIEW OF THE INVESTIGATION

The objective of this research was to develop a computationally efficient method to calculate, from nodal output, the fine-mesh three-dimensional neutron flux and, thus, the reactor pointwise power distribution.

In Chapter 2, the Three-Dimensional Form Function Method for reconstructing flux shapes from nodal solutions was derived. This method was based on the assumption that, for each neutron group and within any reactor node, the fine-mesh flux can be expressed as the product of an assembly function and a tri-quadratic polynomial function. The assembly function was obtained by a series of local fine-mesh two-dimensional criticality calculations. The polynomial coefficients were determined by forcing the fine-mesh flux to reproduce the global nodal solution and to satisfy the neutron diffusion finite difference equations about node corner points and, in an integral sense, along node lines. The implementation of these conditions at all reactor nodes provides a system of balance equations written in terms of node corner point fluxes and node line averaged fluxes. The resulting spatial coupling is to 24 node lines and 16 corner points. An iterative solution technique was developed for the solution of the balance equations.

In Chapter 3, the results of two- and three-dimensional applications to several reactor benchmark problems were presented. The reconstruction

scheme was shown to be very accurate, especially for interior points, where the pointwise average power was determined with a maximum error of approximately two percent for axial mesh lines in the unrodded region and four percent for axial mesh lines in the rodded region. In particular, the power in the hottest point of the 3D-EPRI-9 benchmark problem, was determined with an error of 0.42%. The Three-Dimensional Form Function Method, incorporated into the REFLUX computer code, was also shown to be about two orders of magnitude computationally faster than conventional finite difference methods.

Thus, the method developed in this investigation for calculating pointwise fluxes and pointwise powers has been shown to be a very attractive alternative to the finite difference method for the performance of fuel management studies, thermal hydraulic analysis, and many other calculations needed to assess the safety, reliability and economic performance of nuclear LWR's.

4.2 RECOMMENDATIONS FOR FUTURE RESEARCH

During the course of this research, many interesting topics have not been investigated. This section contains a brief description of these potential research areas.

4.2.1 The Assembly Function

4.2.1.1 Quarter Core PDQ-7 Calculations

In the present analysis, the assembly function introduced in Eq. 2-2 was, in all problems, obtained through two-dimensional PDQ-7 color set calculations. However, for the analysis of three-dimensional reactor

problems, two-dimensional quarter reactor core PDQ-7 calculations could be carried out to obtain more accurate results. The computational effort required to perform a two-dimensional quarter core calculation is considerably smaller than that required to perform a three-dimensional PDQ-7 reactor calculation. Thus, even if these quarter core calculations were employed, the reconstruction scheme would still be more computationally efficient than conventional finite difference methods.

4.2.1.2 Assembly Function Normalization along Node Lines

When the assembly function is obtained through color set or assembly calculations, two different shapes are available for the two sides (i.e., the + and - sides) of the node faces that share different color sets. In order to avoid the complexity of dealing with different shapes in the present investigation, one of two neighboring color set node face shapes was chosen according to Eqs. 2-1 and 2-2. However, another approach to obtain a single node face shape would be to define a normalized average of the two neighboring color set node face shapes. In particular, the normalization scheme for the discontinuities in axial direction, described in Appendix F, could be easily applied for discontinuities in the radial direction. It would be interesting to investigate the accuracy of various normalization schemes that could be employed for this purpose.

4.2.1.3 Albedo Boundary Condition for Color Set Calculations

It has been verified by Parsons,[8] that when color set calculations with an analytical albedo boundary condition, rather than a zero-current boundary condition, were applied to calculate the assembly function

required for the reconstruction scheme described in Ref. 6, more accurate corner point fluxes were obtained.

If such a scheme is applied to the reconstruction scheme presented in this thesis, presumedly, an increase in accuracy would also be achieved.

4.2.2 The Axial Reflector Problem

In the study of the 3D-EPRI-9 problem, it has been shown that maximum errors in pointwise flux and power occurred in points near the top and bottom water reflector. In this section, several methods for obtaining better results in this region are briefly described. The first two methods presented imply modification of the assembly function; the third method implies modification of the form function.

4.2.2.1 Three-Dimensional Color Set Calculations

In order to develop a computationally efficient flux reconstruction method, it was assumed for the present investigation that the assembly function had no z dependence. However, this method could easily be generalized to encompass z-dependent assembly functions. The assembly functions would be evaluated by three-dimensional color set calculations. The number of three-dimensional color sets would be limited to the nodes at the reactor axial surfaces, and the number of axial mesh points taken for these color sets would be reduced to a minimum.

The use of three-dimensional color sets would lead to increased accuracy, but it would decrease the computational efficiency of the method.

4.2.2.2 Axial Discontinuity Functions

A scheme to improve the accuracy of the pointwise flux and power at points near the axial reflectors could be developed by multiplying the assembly function, $\psi(x,y)$, by a function in the variable z, f(z). This function should be determined by one- or two-dimensional axial criticality calculations (i.e., axial color sets).

It would be also interesting to investigate other methods involving discontinuity factors that multiply corner point fluxes, node line averaged fluxes, or node face averaged fluxes.

4.2.2.3 Form Function Modification

The tri-quadratic polynomial corresponding to nodes at the reactor axial surfaces could be partially or totally modified to include analytical functions (i.e., sines, cosines, ...) or expansions of those functions with unknown parameters. These parameters could be obtained by methods similar to those employed to obtain the polynomial coefficients.

However, this approach would require significant modification of the scheme developed in this thesis.

4.2.3 The Problem with Control Rods Partially Inserted

The presence of a control rod partially inserted in the core causes the assembly function, and thus the reconstructed flux, to be discontinuous in the axial direction at the control rod radial face. This fact may result in large errors in the prediction of fine-mesh fluxes and powers near the control rod tip. A normalization scheme was introduced in Appendix F to deal with this discontinuity problem. This normalization

scheme was very accurate in all cases examined. However, it has not been extensively tested, and it would be interesting to test such a scheme for other problems.

4.2.4 The Computer Code

4.2.4.1 Storage Requirements

If the flux reconstruction method developed in this thesis is applied to large three-dimensional LWR configurations, special consideration must be given to computer storage requirements. Input/Output schemes for shuffling data into and out of the computer code might be required, and perhaps other computational methods will be necessary to handle these problems efficiently.

4.2.4.2 Code Automatization

At present, the preparation of the QUANDRY and REFLUX input data must be done by hand or by means of other codes; thus, manpower requirements to obtain the REFLUX solution are substantial. The overall process could be automated in such a way that the nodal solution and the pointwise flux and power could be directly obtained from the heterogeneous nuclear composition and reactor geometry, as is done in the PDQ-7 computer code.

4.2.5 An Iterative Scheme

Node face averaged currents can be calculated from the fine-mesh reconstructed flux. If these currents, when compared to a reference PDQ-7 solution, are more accurate than those obtained by a nodal method, then an iterative scheme could be devised that, if successful, would improve the

nodal solution and the reconstructed flux. In order to apply this scheme, first, the pointwise flux would be obtained from a REFLUX calculation. From this pointwise flux, node face averaged currents could be calculated. The reconstructed pointwise flux and node face averaged currents could be used to evaluate new homogenized cross sections and discontinuity factors (input data for QUANDRY) and a new nodal solution (input data for REFLUX) could be calculated. By inputting the QUANDRY solution to REFLUX, an updated pointwise flux would be obtained. The process could be repeated until convergence is reached.

REFERENCES

1. KORD S. SMITH, "An Analytical Nodal Method for Solving the Two-Group, Multidimensional, Static and Transient Neutron Diffusion Equation," N.E. Thesis, Department of Nuclear Engineering, M.I.T., Cambridge, MA, March 1979.

2. K. KOEBKE, "A New Approach to Homogenization and Group Condensation," Paper presented at IAEA Technical Committee Meeting on Homogenization Methods in Reactor Physics, Lugano, Switzerland, November 1978.

3. KORD S. SMITH, "Spatial Homogenization Methods for Light Water Reactor Analysis," Ph.D. Thesis, Department of Nuclear Engineering, M.I.T., Cambridge, MA, June 1980.

4. CHRISTOPHER L. HOXIE, "Applications of Nodal Equivalence Theory to the Neutronic Analysis of PWR's," Ph.D. Thesis, Department of Nuclear Engineering, M.I.T., Cambridge, MA, June 1982.

5. PHILIPPE J. FINCK, "Homogenization and Dehomogenization Schemes for BWR Assemblies," Ph.D. Thesis, Department of Nuclear Engineering, M.I.T., Cambridge, MA, January 1983.

6. HUSSEIN S. KHALIL, "The Applications of Nodal Methods to PWR Analysis," Ph.D. Thesis, Department of Nuclear Engineering, M.I.T., Cambridge, MA, January 1983.

7. ALLAN F. HENRY, Nuclear Reactor Analysis, M.I.T. Press, Cambridge, MA, 1975.

8. DONALD K. PARSONS, "The Replacement of Reflectors and Baffles in Nodal Calculations by Albedo Boundary Conditions," Ph.D. Thesis, Department of Nuclear Engineering, M.I.T., Cambridge, MA, February 1984.

9. W. R. CALDWELL, "PDQ-7 Reference Manual," WAPD-TM-678, Bettis Atomic Power Laboratory, 1967.

Appendix A

POLYNOMIAL FUNCTION AND INTEGRAL COEFFICIENTS

The reconstructed flux, $\phi_g^{i,j,k}(x,y,z)$, for group g and node (i,j,k) can be expressed in terms of the nodal corner point fluxes, ϕ_{cg}, and the nodal averaged fluxes, $\bar{\phi}_{ug}$, $\bar{\bar{\phi}}_{ug}$, $\bar{\bar{\bar{\phi}}}_g$, (u = x, y, z).

$$\begin{aligned}
\phi_g^{i,j,k}(x,y,z) = {} & C_{g1}^{i,j,k}(x,y,z)\cdot\phi_{cg}^{i,j,k} + C_{g2}^{i,j,k}(x,y,z)\cdot\phi_{cg}^{i+1,j,k} \\
& + C_{g3}^{i,j,k}(x,y,z)\cdot\phi_{cg}^{i+1,j+1,k} + C_{g4}^{i,j,k}(x,y,z)\cdot\phi_{cg}^{i,j+1,k} \\
& + C_{g5}^{i,j,k}(x,y,z)\cdot\phi_{cg}^{i,j,k+1} + C_{g6}^{i,j,k}(x,y,z)\cdot\phi_{cg}^{i+1,j,k+1} \\
& + C_{g7}^{i,j,k}(x,y,z)\cdot\phi_{cg}^{i+1,j+1,k+1} + C_{g8}^{i,j,k}(x,y,z)\cdot\phi_{cg}^{i,j+1,k+1} \\
& + S_{g1}^{i,j,k}(x,y,z)\cdot\bar{\phi}_{xg}^{i,j,k} + S_{g2}^{i,j,k}(x,y,z)\cdot\bar{\phi}_{xg}^{i,j+1,k} \\
& + S_{g3}^{i,j,k}(x,y,z)\cdot\bar{\phi}_{yg}^{i+1,j,k} + S_{g4}^{i,j,k}(x,y,z)\cdot\bar{\phi}_{yg}^{i,j,k} \\
& + S_{g5}^{i,j,k}(x,y,z)\cdot\bar{\phi}_{xg}^{i,j,k+1} + S_{g6}^{i,j,k}(x,y,z)\cdot\bar{\phi}_{xg}^{i,j+1,k+1} \\
& + S_{g7}^{i,j,k}(x,y,z)\cdot\bar{\phi}_{yg}^{i+1,j,k+1} + S_{g8}^{i,j,k}(x,y,z)\cdot\bar{\phi}_{yg}^{i,j,k+1} \\
& + S_{g9}^{i,j,k}(x,y,z)\cdot\bar{\phi}_{zg}^{i,j,k} + S_{g10}^{i,j,k}(x,y,z)\cdot\bar{\phi}_{zg}^{i+1,j,k} \\
& + S_{g11}^{i,j,k}(x,y,z)\cdot\bar{\phi}_{zg}^{i+1,j+1,k} + S_{g12}^{i,j,k}(x,y,z)\cdot\bar{\phi}_{zg}^{i,j+1,k} \\
& + V_{g1}^{i,j,k}(x,y,z)\cdot\bar{\bar{\phi}}_{yg}^{i,j,k} + V_{g2}^{i,j,k}(x,y,z)\cdot\bar{\bar{\phi}}_{yg}^{i,j+1,k} \\
& + V_{g3}^{i,j,k}(x,y,z)\cdot\bar{\bar{\phi}}_{xg}^{i+1,j,k} + V_{g4}^{i,j,k}(x,y,z)\cdot\bar{\bar{\phi}}_{xg}^{i,j,k} +
\end{aligned}$$

(continued)

$$+ V_{g5}^{i,j,k}(x,y,z)\cdot\bar{\bar{\phi}}_{zg}^{i,j,k} + V_{g6}^{i,j,k}(x,y,z)\cdot\bar{\bar{\phi}}_{zg}^{i,j,k+1}$$

$$+ W_{g}^{i,j,k}(x,y,z)\cdot\bar{\bar{\bar{\phi}}}_{g}^{i,j,k} \qquad \text{(A-1)}$$

where

$\phi_{cg}^{i,j,k}$ ≡ corner point flux for group g and point (i,j,k)

$\bar{\phi}_{ug}^{i,j,k}$ ≡ line averaged flux for group g and node line parallel to direction u (u = x,y,z)

$\bar{\bar{\phi}}_{ug}^{i,j,k}$ ≡ surface averaged flux for group g and node face perpendicular to direction u (u = x,y,z)

$\bar{\bar{\bar{\phi}}}_{g}^{i,j,k}$ ≡ volume averaged flux for group g and node (i,j,k)

and the functions C, S, V and W are defined by the following expressions:

$$C_{g1}^{i,j,k}(x,y,z) \equiv \frac{\psi_g^{i,j,k}(x,y)}{\psi_g^{i,j,k}\left(\frac{-h_x}{2},\frac{-h_y}{2}\right)}\left\{\left[P_{g1}^{i,j,k}\left(x^2-\frac{h_x^2}{4}\right)-\frac{x}{h_x}+0.5\right]\right.$$

$$\cdot\left[Q_{g1}^{i,j,k}\left(y^2-\frac{h_y^2}{4}\right)-\frac{y}{h_y}+0.5\right]+T_{g1}^{i,j,k}\left(x^2-\frac{h_x^2}{4}\right)\left(y^2-\frac{h_y^2}{4}\right)\Bigg\}$$

$$\cdot\left\{P_5^k\left(z^2-\frac{h_z^2}{4}\right)-\frac{z}{h_z}+0.5\right\}$$

$$C_{g2}^{i,j,k}(x,y,z) \equiv \frac{\psi_g^{i,j,k}(x,y)}{\psi_g^{i,j,k}\left(\frac{h_x}{2},\frac{-h_y}{2}\right)}\left\{\left[P_{g4}^{i,j,k}\left(x^2-\frac{h_x^2}{4}\right)+\frac{x}{h_x}+0.5\right]\right.$$

$$\cdot\left[Q_{g4}^{i,j,k}\left(y^2-\frac{h_y^2}{4}\right)-\frac{y}{h_y}+0.5\right]+T_{g4}^{i,j,k}\left(x^2-\frac{h_x^2}{4}\right)\left(y^2-\frac{h_y^2}{4}\right)\Bigg\}$$

$$\cdot\left\{P_5^k\left(z^2-\frac{h_z^2}{4}\right)-\frac{z}{h_z}+0.5\right\}$$

$$C_{g3}^{i,j,k}(x,y,z) \equiv \frac{\psi_g^{i,j,k}(x,y)}{\psi_g^{i,j,k}\left(\frac{h_x}{2},\frac{h_y}{2}\right)}\left\{\left[P_{g3}^{i,j,k}\left(x^2-\frac{h_x^2}{4}\right)+\frac{x}{h_x}+0.5\right]\right.$$

$$\cdot\left[Q_{g3}^{i,j,k}\left(y^2-\frac{h_y^2}{4}\right)+\frac{y}{h_y}+0.5\right]+T_{g3}^{i,j,k}\left(x^2-\frac{h_x^2}{4}\right)\left(y^2-\frac{h_y^2}{4}\right)\Big\}$$

$$\cdot\left\{P_5^k\left(z^2-\frac{h_z^2}{4}\right)-\frac{z}{h_z}+0.5\right\}$$

$$C_{g4}^{i,j,k}(x,y,z) \equiv \frac{\psi_g^{i,j,k}(x,y)}{\psi_g^{i,j,k}\left(\frac{-h_x}{2},\frac{h_y}{2}\right)}\left\{\left[P_{g2}^{i,j,k}\left(x^2-\frac{h_x^2}{4}\right)-\frac{x}{h_x}+0.5\right]\right.$$

$$\cdot\left[Q_{g2}^{i,j,k}\left(y^2-\frac{h_y^2}{4}\right)+\frac{y}{h_y}+0.5\right]+T_{g2}^{i,j,k}\left(x^2-\frac{h_x^2}{4}\right)\left(y^2-\frac{h_y^2}{4}\right)\Big\}$$

$$\cdot\left\{P_5^k\left(z^2-\frac{h_z^2}{4}\right)-\frac{z}{h_z}+0.5\right\}$$

$$C_{g5}^{i,j,k}(x,y,z) \equiv \frac{\psi_g^{i,j,k}(x,y)}{\psi_g^{i,j,k}\left(\frac{-h_x}{2},\frac{-h_y}{2}\right)}\left\{\left[P_{g1}^{i,j,k}\left(x^2-\frac{h_x^2}{4}\right)-\frac{x}{h_x}+0.5\right]\right.$$

$$\cdot\left[Q_{g1}^{i,j,k}\left(y^2-\frac{h_y^2}{4}\right)-\frac{y}{h_y}+0.5\right]+T_{g1}^{i,j,k}\left(x^2-\frac{h_x^2}{4}\right)\left(y^2-\frac{h_y^2}{4}\right)\Big\}$$

$$\cdot\left\{Q_5^k\left(z^2-\frac{h_z^2}{4}\right)+\frac{z}{h_z}+0.5\right\}$$

$$C_{g6}^{i,j,k}(x,y,z) \equiv \frac{\psi_g^{i,j,k}(x,y)}{\psi_g^{i,j,k}\left(\frac{h_x}{2},\frac{-h_y}{2}\right)}\left\{\left[P_{g4}^{i,j,k}\left(x^2-\frac{h_x^2}{4}\right)+\frac{x}{h_x}+0.5\right]\right.$$

$$\cdot\left[Q_{g4}^{i,j,k}\left(y^2-\frac{h_y^2}{4}\right)-\frac{y}{h_y}+0.5\right]+T_{g4}^{i,j,k}\left(x^2-\frac{h_x^2}{4}\right)\left(y^2-\frac{h_y^2}{4}\right)\Big\}$$

$$\cdot\left\{Q_5^k\left(z^2-\frac{h_z^2}{4}\right)+\frac{z}{h_z}+0.5\right\}$$

$$C_{g7}^{i,j,k}(x,y,z) \equiv \frac{\psi_g^{i,j,k}}{\psi_g^{i,j,k}\left(\frac{h_x}{2},\frac{h_y}{2}\right)} \left\{\left[p_{g3}^{i,j,k}\left(x^2-\frac{h_x^2}{4}\right)+\frac{x}{h_x}+0.5\right]\right.$$

$$\cdot\left[Q_{g3}^{i,j,k}\left(y^2-\frac{h_y^2}{y}\right)+\frac{y}{h_y}+0.5\right]+T_{g3}^{i,j,k}\left(x^2-\frac{h_x^2}{4}\right)\left(y^2-\frac{h_y^2}{4}\right)\Bigg\}$$

$$\cdot\left\{Q_5^k\left(z^2-\frac{h_z^2}{4}\right)+\frac{z}{h_z}+0.5\right\}$$

$$C_{g8}^{i,j,k}(x,y,z) \equiv \frac{\psi_g^{i,j,k}(x,y)}{\psi_g^{i,j,k}\left(-\frac{h_x}{2},\frac{h_y}{2}\right)} \left\{\left[p_{g2}^{i,j,k}\left(x^2-\frac{h_x^2}{4}\right)-\frac{x}{h_x}+0.5\right]\right.$$

$$\cdot\left[Q_{g2}^{i,j,k}\left(y^2-\frac{h_y^2}{4}\right)+\frac{y}{h_y}+0.5\right]+T_{g2}^{i,j,k}\left(x^2-\frac{h_x^2}{4}\right)\left(y^2-\frac{h_y^2}{4}\right)\Bigg\}$$

$$\cdot\left\{Q_5^k\left(z^2-\frac{h_z^2}{4}\right)+\frac{z}{h_z}+0.5\right\}$$

$$S_{g1}^{i,j,k}(x,y,z) \equiv \frac{\psi_g^{i,j,k}(x,y)\left[B_{g2}^{i,j,k}\left(y^2-\frac{h_y^2}{4}\right)-\frac{y}{h_y}+0.5\right]\left[x^2-\frac{h_x^2}{4}\right]\left[P_5^k\left(z^2-\frac{h_z^2}{4}\right)-\frac{z}{h_z}+0.5\right]h_x}{\int_{-h_x/2}^{h_x/2}\left(x^2-\frac{h_x^2}{4}\right)\psi_g^{i,j,k}\left(x,\frac{-h_y}{2}\right)dx}$$

$$S_{g2}^{i,j,k}(x,y,z) \equiv \frac{\psi_g^{i,j,k}(x,y)\left[B_{g1}^{i,j,k}\left(y^2-\frac{h_y^2}{4}\right)+\frac{y}{h_y}+0.5\right]\left[x^2-\frac{h_x^2}{4}\right]\left[P_5^k\left(z^2-\frac{h_z^2}{4}\right)-\frac{z}{h_z}+0.5\right]h_x}{\int_{-h_x/2}^{h_x/2}\left(x^2-\frac{h_x^2}{4}\right)\psi_g^{i,j,k}\left(x,\frac{h_y}{2}\right)dx}$$

$$S_{g3}^{i,j,k}(x,y,z) \equiv \frac{\psi_g^{i,j,k}(x,y)\left[R_{g2}^{i,j,k}\left(x^2-\frac{h_x^2}{4}\right)+\frac{x}{h_x}+0.5\right]\left[y^2-\frac{h_y^2}{4}\right]\left[P_5^k\left(z^2-\frac{h_z^2}{4}\right)-\frac{z}{h_z}+0.5\right]h_y}{\int_{-h_y/2}^{h_y/2}\left(y^2-\frac{h_y^2}{4}\right)\psi_g^{i,j,k}\left(\frac{h_x}{2},y\right)dy}$$

$$S_{g4}^{i,j,k}(x,y,z) \equiv \frac{\psi_g^{i,j,k}(x,y)\left[R_{g1}^{i,j,k}\left(x^2-\frac{h_x^2}{4}\right)-\frac{x}{h_x}+0.5\right]\left[y^2-\frac{h_y^2}{4}\right]\left[P_5^k\left(z^2-\frac{h_z^2}{4}\right)-\frac{z}{h_z}+0.5\right]h_y}{\int_{-h_y/2}^{h_y/2}\left(y^2-\frac{h_y^2}{4}\right)\psi_g^{i,j,k}\left(\frac{-h_x}{2},y\right)dy}$$

$$S_{g5}^{i,j,k}(x,y,z) \equiv \frac{\psi_g^{i,j,k}(x,y)\left[B_{g2}^{i,j,k}\left(y^2-\frac{h_y^2}{4}\right)-\frac{y}{h_y}+0.5\right]\left[x^2-\frac{h_x^2}{4}\right]\left[Q_5^k\left(z^2-\frac{h_z^2}{4}\right)+\frac{z}{h_z}+0.5\right]h_x}{\int_{-h_x/2}^{h_x/2}\left(x^2-\frac{h_x^2}{4}\right)\psi_g^{i,j,k}\left(x,\frac{-h_y}{2}\right)dx}$$

$$S_{g6}^{i,j,k}(x,y,z) \equiv \frac{\psi_g^{i,j,k}(x,y)\left[B_{g1}^{i,j,k}\left(y^2-\frac{h_y^2}{4}\right)+\frac{y}{h_y}+0.5\right]\left[x^2-\frac{h_x^2}{4}\right]\left[Q_5^k\left(z^2-\frac{h_z^2}{4}\right)+\frac{z}{h_z}+0.5\right]h_x}{\int_{-h_x/2}^{h_x/2}\left(x^2-\frac{h_x^2}{4}\right)\psi_g^{i,j,k}\left(x,\frac{h_y}{2}\right)dx}$$

$$S_{g7}^{i,j,k}(x,y,z) \equiv \frac{\psi_g^{i,j,k}(x,y)\left[B_{g2}^{i,j,k}\left(x^2-\frac{h_x^2}{4}\right)+\frac{x}{h_x}+0.5\right]\left[y^2-\frac{h_y^2}{4}\right]\left[Q_5^k\left(z^2-\frac{h_z^2}{4}\right)+\frac{z}{h_z}+0.5\right]h_y}{\int_{-h_y/2}^{h_y/2}\left(y^2-\frac{h_y^2}{4}\right)\psi_g^{i,j,k}\left(\frac{h_x}{2},y\right)dy}$$

$$S_{g8}^{i,j,k}(x,y,z) \equiv \frac{\psi_g^{i,j,k}(x,y)\left[R_{g1}^{i,j,k}\left(x^2-\frac{h_x^2}{4}\right)-\frac{x}{h_x}+0.5\right]\left[y^2-\frac{h_y^2}{4}\right]\left[Q_5^k\left(z^2-\frac{h_z^2}{4}\right)+\frac{z}{h_z}+0.5\right]h_y}{\int_{-h_y/2}^{h_y/2}\left(y^2-\frac{h_y^2}{4}\right)\psi_g^{i,j,k}\left(\frac{-h_x}{2},y\right)dy}$$

$$S_{g9}^{i,j,k}(x,y,z) \equiv \frac{\psi_g^{i,j,k}(x,y)\left\{\left[P_{g1}^{i,j,k}\left(x^2-\frac{h_x^2}{4}\right)-\frac{x}{h_x}+0.5\right]\left[Q_{g1}^{i,j,k}\left(y^2-\frac{h_y^2}{4}\right)-\frac{y}{h_y}+0.5\right]+T_{g1}^{i,j,k}\left(x^2-\frac{h_x^2}{4}\right)\left(y^2-\frac{h_y^2}{4}\right)\right\}\left\{z^2-\frac{h_z^2}{4}\right\}h_z}{\psi_g^{i,j,k}\left(\frac{-h_x}{2},\frac{-h_y}{2}\right)\int_{-h_z/2}^{h_z/2}\left(z^2-\frac{h_z^2}{4}\right)dz}$$

$$S_{g10}^{i,j,k}(x,y,z) \equiv \frac{\psi_g^{i,j,k}(x,y)\left\{\left[P_{g4}^{i,j,k}\left(x^2-\frac{h_x^2}{4}\right)+\frac{x}{h_x}+0.5\right]\left[Q_{g4}^{i,j,k}\left(y^2-\frac{h_y^2}{4}\right)-\frac{y}{h_y}+0.5\right]+T_{g4}^{i,j,k}\left(x^2-\frac{h_x^2}{4}\right)\left(y^2-\frac{h_y^2}{4}\right)\right\}\left\{z^2-\frac{h_z^2}{4}\right\}h_z}{\psi_g^{i,j,k}\left(\frac{h_x}{2},\frac{-h_y}{2}\right)\int_{-h_z/2}^{h_z/2}\left(z^2-\frac{h_z^2}{4}\right)dz}$$

$$S_{g11}^{i,j,k}(x,y,z) \equiv \frac{\psi_g^{i,j,k}(x,y)\left\{\left[P_{g3}^{i,j,k}\left(x^2-\frac{h_x^2}{4}\right)+\frac{x}{h_x}+0.5\right]\left[Q_{g3}^{i,j,k}\left(y^2-\frac{h_y^2}{4}\right)+\frac{y}{h_y}+0.5\right]+T_{g3}^{i,j,k}\left(x^2-\frac{h_x^2}{4}\right)\left(y^2-\frac{h_y}{4}\right)\right\}\left\{z^2-\frac{h_z^2}{4}\right\}h_z}{\psi_g^{i,j,k}\left(\frac{h_x}{2},\frac{h_y}{2}\right)\int_{-h_z/2}^{h_z/2}\left(z^2-\frac{h_z^2}{4}\right)dz}$$

$$S_{g12}^{i,j,k}(x,y,z) \equiv \frac{\psi_g^{i,j,k}(x,y)\left\{\left[P_{g2}^{i,j,k}\left(x^2-\frac{h_x^2}{4}\right)-\frac{x}{h_z}+0.5\right]\left[Q_{g2}^{i,j,k}\left(y^2-\frac{h_y^2}{4}\right)+\frac{y}{h_y}+0.5\right]+T_{g2}^{i,j,k}\left(x^2-\frac{h_x^2}{4}\right)\left(y^2-\frac{h_y^2}{4}\right)\left\{z^2-\frac{h_z^2}{4}\right\}h_z}{\psi_g^{i,j,k}\left(\frac{-h_x}{2},\frac{h_y}{2}\right)\int_{-h_z/2}^{h_z/2}\left(z^2-\frac{h_z^2}{4}\right)dz}$$

$$V_{g1}^{i,j,k}(x,y,z) \equiv \frac{\psi_g^{i,j,k}(x,y)\left[B_{g2}^{i,j,k}\left(y^2-\frac{h_y^2}{4}\right)-\frac{y}{h_y}+0.5\right]\left[x^2-\frac{h_x^2}{4}\right]\left[z^2-\frac{h_z^2}{4}\right]h_x h_z}{\int_{-h_x/2}^{h_x/2}\psi_g^{i,j,k}\left(x,\frac{-h_y}{2}\right)\left(x^2-\frac{h_x^2}{4}\right)dx\int_{-h_z/2}^{h_z/2}\left(z^2-\frac{h_z^2}{4}\right)dz}$$

$$V_{g2}^{i,j,k}(x,y,z) \equiv \frac{\psi_g^{i,j,k}(x,y)\left[B_{g1}^{i,j,k}\left(y^2-\frac{h_y^2}{4}\right)+\frac{y}{h_y}+0.5\right]\left[x^2-\frac{h_x^2}{4}\right]\left[z^2-\frac{h_z^2}{4}\right]h_x h_z}{\int_{-h_x/2}^{h_x/2}\psi_g^{i,j,k}\left(x,\frac{h_y}{2}\right)\left(x^2-\frac{h_x^2}{4}\right)dx\int_{-h_z/2}^{h_z/2}\left(z^2-\frac{h_z^2}{4}\right)dz}$$

$$V_{g3}^{i,j,k}(x,y,z) \equiv \frac{\psi_g^{i,j,k}(x,y)\left[R_{g2}^{i,j,k}\left(x^2-\frac{h_x^2}{4}\right)+\frac{x}{h_x}+0.5\right]\left[y^2-\frac{h_y^2}{4}\right]\left[z^2-\frac{h_z^2}{4}\right]h_y h_z}{\int_{-h_y/2}^{h_y/2}\psi_g^{i,j,k}\left(\frac{h_x}{2},y\right)\left(y^2-\frac{h_y^2}{4}\right)dy\int_{-h_z/2}^{h_z/2}\left(z^2-\frac{h_z^2}{4}\right)dz}$$

$$V_{g4}^{i,j,k}(x,y,z) \equiv \frac{\psi_g^{i,j,k}(x,y)\left[R_{g1}^{i,j,k}\left(x^2-\frac{h_x^2}{4}\right)-\frac{x}{h_x}+0.5\right]\left[y^2-\frac{h_y^2}{4}\right]\left[z^2-\frac{h_z^2}{4}\right]h_y h_z}{\int_{-h_y/2}^{h_y/2}\psi_g^{i,j,k}\left(\frac{-h_x}{2},y\right)\left(y^2-\frac{h_y^2}{4}\right)dy\int_{-h_z/2}^{h_z/2}\left(z^2-\frac{h_z^2}{4}\right)dz}$$

$$V_{g5}^{i,j,k}(x,y,z) \equiv \frac{\psi_g^{i,j,k}(x,y)\left[x^2-\frac{h_x^2}{4}\right]\left[y^2-\frac{h_y^2}{4}\right]\left[P_5^k\left(z^2-\frac{h_z^2}{4}\right)-\frac{z}{h_z}+0.5\right]h_x h_y}{\int_{-h_x/2}^{h_x/2}dx\int_{-h_y/2}^{h_y/2}\psi_g^{i,j,k}(x,y)\left[x^2-\frac{h_x^2}{4}\right]\left[y^2-\frac{h_y^2}{4}\right]dy}$$

$$V_{g6}^{i,j,k}(x,y,z) \equiv \frac{\psi_g^{i,j,k}(x,y)\left[x^2-\frac{h_x^2}{4}\right]\left[y^2-\frac{h_y^2}{4}\right]\left[Q_5^k\left(z^2-\frac{h_z^2}{4}\right)+\frac{z}{h_z}+0.5\right]h_x h_y}{\int_{-h_x/2}^{h_x/2}dx\int_{-h_y/2}^{h_y/2}\psi_g^{i,j,k}(x,y)\left[x^2-\frac{h_x^2}{4}\right]\left[y^2-\frac{h_y^2}{4}\right]dy}$$

$$W_g^{i,j,k}(x,y,z) \equiv \frac{\psi_g^{i,j,k}(x,y)\left[x^2-\frac{h_x^2}{4}\right]\left[y^2-\frac{h_y^2}{4}\right]\left[z^2-\frac{h_z^2}{4}\right] h_x h_y h_z}{\int_{-h_x/2}^{h_x/2} dx \int_{-h_y/2}^{h_y/2} \psi_g^{i,j,k}(x,y)\left[x^2-\frac{h_x^2}{4}\right]\left[y^2-\frac{h_y^2}{4}\right] dy \int_{-h_z/2}^{h_z/2}\left(z^2-\frac{h_z^2}{4}\right) dz}$$

where

x,y,z = coordinates of a generic point inside node (i,j,k) with respect to a Cartesian coordinate system with its origin at the node center,

$h_x \equiv h_x^i$ = length of node (i,j,k) in the X direction,

$h_y \equiv h_y^j$ = length of node (i,j,k) in the Y direction,

$h_z \equiv h_z^k$ = length of node (i,j,k) in the Z direction,

$\psi_g^{i,j,k}(x,y)$ two-dimensional assembly function for neutron group g and node (i,j,k) obtained through a fine-mesh criticality calculation,

and the numerical coefficients P, Q, T, R and B are defined as:

$$P_{g1}^{i,j,k} \equiv \frac{\int_{-h_x/2}^{h_x/2}\left(x-\frac{h_x}{2}\right)\psi_g^{i,j,k}\left(x,\frac{-h_y}{2}\right) dx}{h_x \int_{-h_x/2}^{h_x/2}\left(x^2-\frac{h_x^2}{4}\right)\psi_g^{i,j,k}\left(x,\frac{-h_y}{2}\right) dx}$$

$$P_{g2}^{i,j,k} \equiv \frac{\int_{-h_x/2}^{h_x/2}\left(x-\frac{h_x}{2}\right)\psi_g^{i,j,k}\left(x,\frac{h_y}{2}\right) dx}{h_x \int_{-h_x/2}^{h_x/2}\left(x^2-\frac{h_x^2}{4}\right)\psi_g^{i,j,k}\left(x,\frac{h_y}{2}\right) dx}$$

$$p_{g3}^{i,j,k} \equiv - \frac{\int_{-h_x/2}^{h_x/2} \left(x + \frac{h_x}{2}\right) \psi_g^{i,j,k}\left(x, \frac{h_y}{2}\right) dx}{h_x \int_{-h_x/2}^{h_x/2} \left(x^2 - \frac{h_x^2}{4}\right) \psi_g^{i,j,k}\left(x, \frac{h_y}{2}\right) dx}$$

$$p_{g4}^{i,j,k} \equiv - \frac{\int_{-h_x/2}^{h_x/2} \left(x + \frac{h_x}{2}\right) \psi_g^{i,j,k}\left(x, \frac{-h_y}{2}\right) dx}{h_x \int_{-h_x/2}^{h_x/2} \left(x^2 - \frac{h_x^2}{4}\right) \psi_g^{i,j,k}\left(x, \frac{-h_y}{2}\right) dx}$$

$$Q_{g1}^{i,j,k} \equiv \frac{\int_{-h_y/2}^{h_y/2} \left(y - \frac{h_y}{2}\right) \psi_g^{i,j,k}\left(\frac{-h_x}{2}, y\right) dy}{h_y \int_{-h_y/2}^{h_y/2} \left(y^2 - \frac{h_y^2}{4}\right) \psi_g^{i,j,k}\left(\frac{-h_x}{2}, y\right) dy}$$

$$Q_{g2}^{i,j,k} \equiv - \frac{\int_{-h_y/2}^{h_y/2} \left(y + \frac{h_y}{2}\right) \psi_g^{i,j,k}\left(\frac{-h_x}{2}, y\right) dy}{h_y \int_{-h_y/2}^{h_y/2} \left(y^2 - \frac{h_y^2}{4}\right) \psi_g^{i,j,k}\left(\frac{-h_x}{2}, y\right) dy}$$

$$Q_{g3}^{i,j,k} \equiv - \frac{\int_{-h_y/2}^{h_y/2} \left(y + \frac{h_y}{2}\right) \psi_g^{i,j,k}\left(\frac{h_x}{2}, y\right) dy}{h_y \int_{-h_y/2}^{h_y/2} \left(y^2 - \frac{h_y^2}{4}\right) \psi_g^{i,j,k}\left(\frac{h_x}{2}, y\right) dy}$$

$$Q_{g4}^{i,j,k} \equiv \frac{\int_{-h_y/2}^{h_y/2} \left(y - \frac{h_y}{2}\right) \psi_g^{i,j,k}\left(\frac{h_x}{2}, y\right) dy}{h_y \int_{-h_y/2}^{h_y/2} \left(y^2 - \frac{h_y^2}{4}\right) \psi_g^{i,j,k}\left(\frac{h_x}{2}, y\right) dy}$$

$$T_{g1}^{i,j,k} \equiv - \frac{\int_{-h_x/2}^{h_x/2} dx \int_{-h_y/2}^{h_y/2} \psi_g^{i,j,k}(x,y)\left[P_{g1}^{i,j,k}\left(x^2 - \frac{h_x^2}{4}\right) - \frac{x}{h_x} + 0.5\right]\left[Q_{g1}^{i,j,k}\left(y^2 - \frac{h_y^2}{4}\right) - \frac{y}{h_y} + 0.5\right] dy}{\int_{-h_x/2}^{h_x/2} dx \int_{-h_y/2}^{h_y/2} \psi_g^{i,j,k}(x,y)\left[x^2 - \frac{h_x^2}{4}\right]\left[y^2 - \frac{h_y^2}{4}\right] dy}$$

$$T_{g2}^{i,j,k} \equiv - \frac{\int_{-h_x/2}^{h_x/2} dx \int_{-h_y/2}^{h_y/2} \psi_g^{i,j,k}(x,y)\left[P_{g2}^{i,j,k}\left(x^2 - \frac{h_x^2}{4}\right) - \frac{x}{h_x} + 0.5\right]\left[Q_{g2}^{i,j,k}\left(y^2 - \frac{h_y^2}{4}\right) + \frac{y}{h_y} + 0.5\right] dy}{\int_{-h_x/2}^{h_x/2} dx \int_{-h_y/2}^{h_y/2} \psi_g^{i,j,k}(x,y)\left[x^2 - \frac{h_x^2}{4}\right]\left[y^2 - \frac{h_y^2}{4}\right] dy}$$

$$T_{g3}^{i,j,k} \equiv - \frac{\int_{-h_x/2}^{h_x/2} dx \int_{-h_y/2}^{h_y/2} \psi_g^{i,j,k}(x,y)\left[P_{g3}^{i,j,k}\left(x^2 - \frac{h_x^2}{4}\right) + \frac{x}{h_x} + 0.5\right]\left[Q_{g3}^{i,j,k}\left(y^2 - \frac{h_y^2}{4}\right) + \frac{y}{h_y} + 0.5\right] dy}{\int_{-h_x/2}^{h_x/2} dx \int_{-h_y/2}^{h_y/2} \psi_g^{i,j,k}(x,y)\left[x^2 - \frac{h_x^2}{4}\right]\left[y^2 - \frac{h_y^2}{4}\right] dy}$$

$$T_{g4}^{i,j,k} \equiv - \frac{\int_{-h_x/2}^{h_x/2} dx \int_{-h_y/2}^{h_y/2} \psi_g^{i,j,k}(x,y)\left[P_{g4}^{i,j,k}\left(x^2 - \frac{h_x^2}{4}\right) + \frac{x}{h_x} + 0.5\right]\left[Q_{g4}^{i,j,k}\left(y^2 - \frac{h_y^2}{4}\right) - \frac{y}{h_y} + 0.5\right] dy}{\int_{-h_x/2}^{h_x/2} dx \int_{-h_y/2}^{h_y/2} \psi_g^{i,j,k}(x,y)\left[x^2 - \frac{h_x^2}{4}\right]\left[y^2 - \frac{h_y^2}{4}\right] dy}$$

$$R_{g1}^{i,j,k} \equiv \frac{\int_{-h_x/2}^{h_x/2} dx \int_{-h_y/2}^{h_y/2} \left(x - \frac{h_x}{2}\right)\left(y^2 - \frac{h_y^2}{4}\right) \psi_g^{i,j,k}(x,y)\, dy}{h_x \int_{-h_x/2}^{h_x/2} dx \int_{-h_y/2}^{h_y/2} \left(x^2 - \frac{h_x^2}{4}\right)\left(y^2 - \frac{h_y^2}{4}\right) \psi_g^{i,j,k}(x,y)\, dy}$$

$$R_{g2}^{i,j,k} \equiv -\frac{\int_{-h_x/2}^{h_x/2} dx \int_{-h_y/2}^{h_y/2} \left(x + \frac{h_x}{2}\right)\left(y^2 - \frac{h_y^2}{4}\right) \psi_g^{i,j,k}(x,y)\, dy}{h_x \int_{-h_x/2}^{h_x/2} dx \int_{-h_y/2}^{h_y/2} \left(x^2 - \frac{h_x^2}{4}\right)\left(y^2 - \frac{h_y^2}{4}\right) \psi_g^{i,j,k}(x,y)\, dy}$$

$$B_{g1}^{i,j,k} \equiv -\frac{\int_{-h_x/2}^{h_x/2} dx \int_{-h_y/2}^{h_y/2} dy \left(y + \frac{h_y}{2}\right)\left(x^2 - \frac{h_x^2}{4}\right) \psi_g^{i,j,k}(x,y)dy}{h_y \int_{-h_x/2}^{h_x/2} dx \int_{-h_y/2}^{h_y/2} \left(x^2 - \frac{h_x^2}{4}\right)\left(y^2 - \frac{h_y^2}{4}\right) \psi_g^{i,j,k}(x,y)\, dy}$$

$$P_5^k \equiv \frac{\int_{-h_z/2}^{h_z/2} \left(z - \frac{h_z}{2}\right) dz}{h_z \int_{-h_z/2}^{h_z/2} \left(z^2 - \frac{h_z^2}{4}\right) dz}$$

$$Q_5^k \equiv -\frac{\int_{-h_z/2}^{h_z/2} \left(z + \frac{h_z}{2}\right) dz}{h_z \int_{-h_z/2}^{h_z/2} \left(z^2 - \frac{h_z^2}{4}\right) dz}$$

where all the integrations are performed numerically.

From these definitions one can verify that the reconstructed flux, $\phi_g^{i,j,k}(x,y,z)$, reproduces the following values:

1. The corner point fluxes

$$\phi_g^{i,j,k}\left(\frac{-h_x}{2}, \frac{-h_y}{2}, \frac{-h_z}{2}\right) = \phi_{cg}^{i,j,k}$$

$$\phi_g^{i,j,k}\left(\frac{h_x}{2}, \frac{-h_y}{2}, \frac{-h_z}{2}\right) = \phi_{cg}^{i+1,j,k}$$

$$\phi_g^{i,j,k}\left(\frac{h_x}{2}, \frac{h_y}{2}, \frac{-h_z}{2}\right) = \phi_{cg}^{i+1,j+1,k}$$

$$\phi_{cg}^{i,j,k}\left(\frac{-h_x}{2}, \frac{h_y}{2}, \frac{-h_z}{2}\right) = \phi_{cg}^{i,j+1,k}$$

$$\phi_{cg}^{i,j,k}\left(\frac{-h_x}{2}, \frac{-h_y}{2}, \frac{h_z}{2}\right) = \phi_{cg}^{i,j,k+1}$$

$$\phi_{cg}^{i,j,k}\left(\frac{h_x}{2}, \frac{-h_y}{2}, \frac{h_z}{2}\right) = \phi_{cg}^{i+1,j,k+1}$$

$$\phi_{cg}^{i,j,k}\left(\frac{h_x}{2}, \frac{h_y}{2}, \frac{h_z}{2}\right) = \phi_{cg}^{i+1,j+1,k+1}$$

$$\phi_{cg}^{i,j,k}\left(\frac{-h_x}{2}, \frac{h_y}{2}, \frac{h_z}{2}\right) = \phi_{cg}^{i,j+1,k+1}$$

2. The line averaged fluxes, when $\phi_g^{i,j,k}(x,y,z)$ is integrated along node lines

$$\frac{1}{h_x}\int_{-h_x/2}^{h_x/2} \phi_g^{i,j,k}\left(x, \frac{-h_y}{2}, \frac{-h_z}{2}\right) dx = \bar{\phi}_{xg}^{i,j,k}$$

$$\frac{1}{h_x}\int_{-h_x/2}^{h_x/2} \phi_g^{i,j,k}\left(x, \frac{h_y}{2}, \frac{-h_z}{2}\right) dx = \bar{\phi}_{xg}^{i,j+1,k}$$

$$\frac{1}{h_x}\int_{-h_x/2}^{h_x/2} \phi_g^{i,j,k}\left(x, \frac{-h_y}{2}, \frac{h_z}{2}\right) dx = \bar{\phi}_{xg}^{i,j,k+1}$$

$$\frac{1}{h_x}\int_{-h_x/2}^{h_x/2} \phi_g^{i,j,k}\left(x, \frac{h_y}{2}, \frac{h_z}{2}\right) dx = \bar{\phi}_{xg}^{i,j+1,k+1}$$

$$\frac{1}{h_y}\int_{-h_y/2}^{h_y/2} \phi_g^{i,j,k}\left(\frac{-h_x}{2}, y, \frac{-h_z}{2}\right) dy = \bar{\phi}_{yg}^{i,j,k}$$

$$\frac{1}{h_y}\int_{-h_y/2}^{h_y/2} \phi_g^{i,j,k}\left(\frac{h_x}{2}, y, \frac{-h_z}{2}\right) dy = \bar{\phi}_{yg}^{i+1,j,k}$$

$$\frac{1}{h_y}\int_{-h_y/2}^{h_y/2} \phi_g^{i,j,k}\left(\frac{-h_x}{2}, y, \frac{h_z}{2}\right) dy = \bar{\phi}_{yg}^{i,j,k+1}$$

$$\frac{1}{h_y}\int_{-h_y/2}^{h_y/2} \phi_g^{i,j,k}\left(\frac{h_x}{2}, y, \frac{h_z}{2}\right) dy = \bar{\phi}_{yg}^{i+1,j,k+1}$$

$$\frac{1}{h_z}\int_{-h_z/2}^{h_z/2} \phi_g^{i,j,k}\left(\frac{-h_x}{2}, \frac{-h_y}{2}, z\right) dz = \bar{\phi}_{zg}^{i,j,k}$$

$$\frac{1}{h_z}\int_{-h_z/2}^{h_z/2} \phi_g^{i,j,k}\left(\frac{h_x}{2}, \frac{-h_y}{2}, z\right) dz = \bar{\phi}_{zg}^{i+1,j,k}$$

$$\frac{1}{h_z}\int_{-h_z/2}^{h_z/2} \phi_g^{i,j,k}\left(\frac{h_x}{2}, \frac{h_y}{2}, z\right) dz = \bar{\phi}_{zg}^{i+1,j+1,k}$$

$$\frac{1}{h_z}\int_{-h_z/2}^{h_z/2} \phi_g^{i,j,k}\left(\frac{-h_x}{2}, \frac{h_y}{2}, z\right) dz = \bar{\phi}_{zg}^{i,j+1,k}$$

3. The nodal surface averaged fluxes, when $\phi_g^{i,j,k}(x,y,z)$ is integrated over the node faces

$$\frac{1}{h_x h_z}\int_{-h_z/2}^{h_z/2} dz \int_{-h_x/2}^{h_x/2} \phi_g^{i,j,k}\left(x, \frac{-h_y}{2}, z\right) dx = \bar{\bar{\phi}}_{yg}^{i,j,k}$$

$$\frac{1}{h_x h_z}\int_{-h_z/2}^{h_z/2} dz \int_{-h_x/2}^{h_x/2} \phi_g^{i,j,k}\left(x, \frac{h_y}{2}, z\right) dx = \bar{\bar{\phi}}_{yg}^{i+1,j,k}$$

$$\frac{1}{h_y h_z}\int_{-h_z/2}^{h_z/2} dz \int_{-h_y/2}^{h_y/2} \phi_g^{i,j,k}\left(\frac{-h_x}{2}, y, z\right) dx = \bar{\bar{\phi}}_{xg}^{i,j,k}$$

$$\frac{1}{h_y h_z}\int_{-h_z/2}^{h_z/2} dz \int_{-h_y/2}^{h_y/2} \phi_g^{i,j,k}\left(\frac{h_x}{2}, y, z\right) dx = \bar{\bar{\phi}}_{xg}^{i,j+1,k}$$

$$\frac{1}{h_x h_y}\int_{-h_x/2}^{h_x/2} dx \int_{-h_y/2}^{h_y/2} \phi_g^{i,j,k}\left(x, y, \frac{-h_z}{2}\right) dz = \bar{\bar{\phi}}_{zg}^{i,j,k}$$

$$\frac{1}{h_x h_y}\int_{-h_x/2}^{h_x/2} dx \int_{-h_y/2}^{h_y/2} \phi_g^{i,j,k}\left(x, y, \frac{h_z}{2}\right) dz = \bar{\bar{\phi}}_{zg}^{i,j,k+1}$$

4. The nodal volume averaged flux, when $\phi_g^{i,j,k}(x,y,z)$ is integrated over the node volume

$$\frac{1}{h_x h_y h_z}\int_{-h_x/2}^{h_x/2} dx \int_{-h_y/2}^{h_y/2} dy \int_{-h_z/2}^{h_z/2} \phi_g^{i,j,k}(x,y,z)\, dz = \bar{\bar{\bar{\phi}}}_g^{i,j,k}$$

Appendix B

DERIVATION OF THE BALANCE EQUATION ABOUT CORNER POINTS

In order to derive the corner point balance equation for corner point (i,j,k), it is first required to integrate the multigroup neutron diffusion equation, Eq. 1-1, over the mesh cell volume, v_c, about corner point (i,j,k); thus,

$$\int_{v_c} - \underline{\nabla} \cdot [D(\underline{r})]\, \underline{\nabla} \cdot [\phi(\underline{r})]\, dv + \int_{v_c} [M(\underline{r})][\phi(\underline{r})]\, dv = [0] \qquad \text{(B-1)}$$

Applying Gauss's theorem and calculating the partial derivatives at the mesh cell faces by the centered finite difference approximation yields for the first term in Eq. B-1:

$$- \int_{S_c} [D(\underline{r})]\underline{\nabla}[\phi(\underline{r})] \cdot \underline{n}\ ds = - \left\{ \int_{S_N} [D(\underline{r})] \frac{[\phi_N^{i,j,k}] - [\phi_c^{i,j,k}]}{h_N} ds \right.$$

$$+ \int_{S_S} [D(\underline{r})] \frac{[\phi_S^{i,j,k}] - [\phi_c^{i,j,k}]}{h_S} ds + \int_{S_E} [D(\underline{r})] \frac{[\phi_E^{i,j,k}] - [\phi_c^{i,j,k}]}{h_E} ds$$

$$+ \int_{S_W} [D(\underline{r})] \frac{[\phi_W^{i,j,k}] - [\phi_c^{i,j,k}]}{h_W} ds + \int_{S_T} [D(\underline{r})] \frac{[\phi_T^{i,j,k}] - [\phi_c^{i,j,k}]}{h_T} ds$$

$$\left. + \int_{S_B} [D(\underline{r})] \frac{[\phi_B^{i,j,k}] - [\phi_c^{i,j,k}]}{h_B} ds \right\}$$

$$\equiv [X_N^{i,j,k}][\phi_N^{i,j,k}] + [X_S^{i,j,k}][\phi_S^{i,j,k}] + [X_E^{i,j,k}][\phi_E^{i,j,k}] + [X_W^{i,j,k}][\phi_W^{i,j,k}]$$

$$+ [X_T^{i,j,k}][\phi_T^{i,j,k}] + [X_B^{i,j,k}][\phi_B^{i,j,k}] + [X_0^{i,j,k}][\phi_c^{i,j,k}] \qquad \text{(B-2)}$$

where $[\phi_c^{i,j,k}]$ is a column vector of length G containing the corner point fluxes at point (i,j,k). $[\phi_N^{i,j,k}]$, $[\phi_S^{i,j,k}]$, $[\phi_E^{i,j,k}]$, $[\phi_W^{i,j,k}]$, $[\phi_T^{i,j,k}]$, $[\phi_B^{i,j,k}]$ are column vectors of length G containing the neutron fluxes at fine mesh points N, S, E, W, T, and B. These fine-mesh points correspond to the north, south, east, west, top and bottom directions as shown in Fig. B-1.

S_c is the total mesh cell surface.

S_N, S_S, S_E, S_W, S_T, S_B are the mesh cell faces corresponding to the north, south, east, west, top and bottom directions.

h_N, h_S, h_E, h_W, h_T, h_B are the mesh distances between the mesh cell center and its nearest neighbors to the north, south, east, west, top and bottom (see Fig. B-1).

Finally, the coefficients $[X^{i,j,k}]$ are G × G diagonal matrices defined by the following expressions:

$$[X_N^{i,j,k}] \equiv -\frac{1}{h_N}\int_{S_N}[D(\underline{r})]\,ds$$

$$[X_S^{i,j,k}] \equiv -\frac{1}{h_S}\int_{S_S}[D(\underline{r})]\,ds$$

$$[X_E^{i,j,k}] \equiv -\frac{1}{h_E}\int_{S_E}[D(\underline{r})]\,ds$$

$$[X_W^{i,j,k}] \equiv -\frac{1}{h_W}\int_{S_W}[D(\underline{r})]\,ds$$

$$[X_T^{i,j,k}] \equiv -\frac{1}{h_T}\int_{S_T}[D(\underline{r})]\,ds$$

$$[X_B^{i,j,k}] \equiv -\frac{1}{h_B}\int_{S_B}[D(\underline{r})]\,ds$$

$$[X_0^{i,j,k}] \equiv -\left\{[X_N^{i,j,k}] + [X_S^{i,j,k}] + [X_E^{i,j,k}] + [X_W^{i,j,k}] + [X_T^{i,j,k}] + [X_B^{i,j,k}]\right\}$$

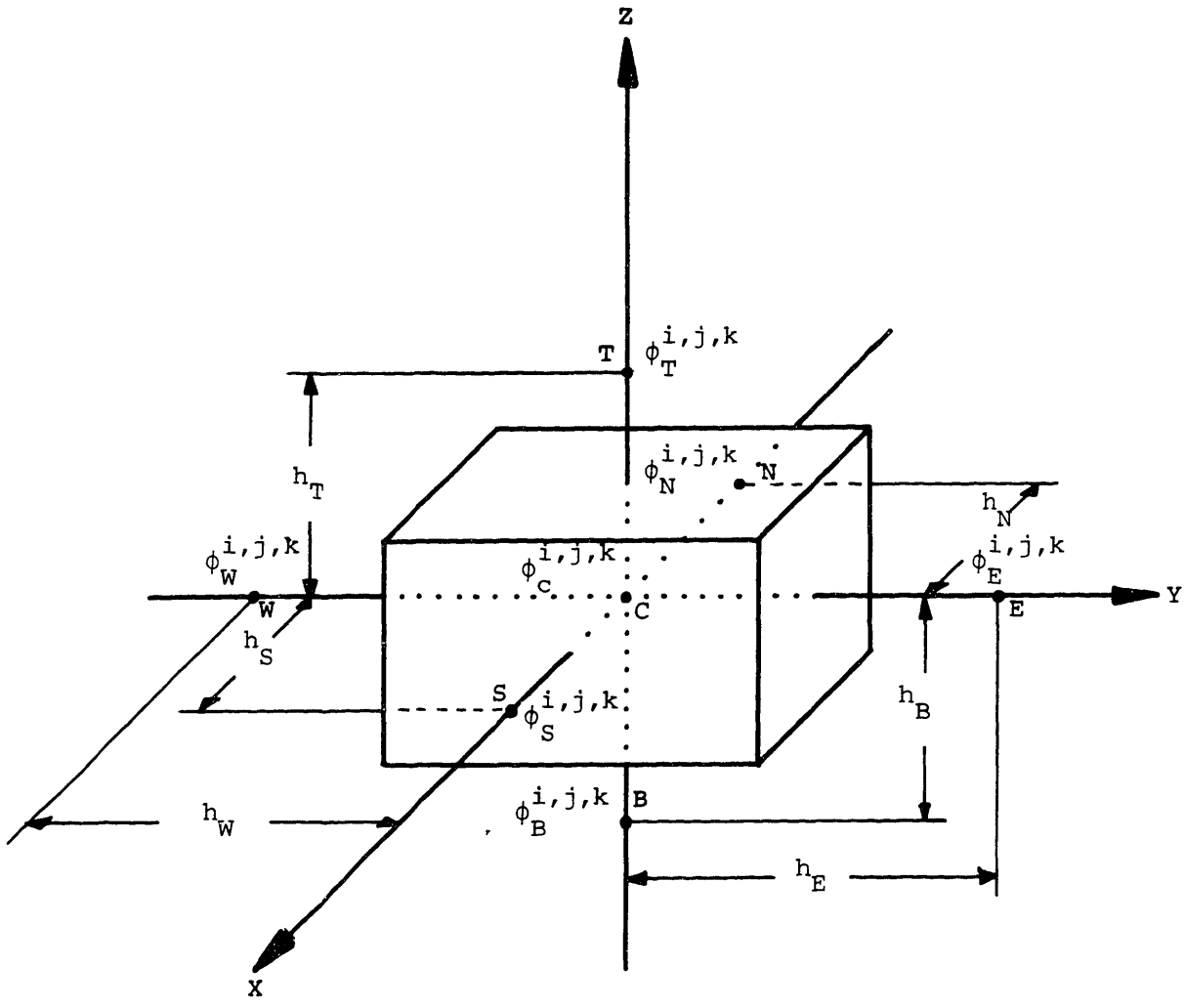

Fig. B-1. Geometry and nomenclature for the balance equation about corner points.

The second term in Eq. B-1 can be written as:

$$\left\{\int_{V_c} [M(\underline{r})]dv\right\}[\phi_c^{i,j,k}] = V_c[\bar{M}^{i,j,k}][\phi_c^{i,j,k}] \tag{B-3}$$

where

V_c is the mesh cell volume and

$$[\bar{M}^{i,j,k}] \equiv \frac{1}{V_c}\int_{V_c} [M(\underline{r})]dv$$

Introducing expressions given by Eqs. B-2 and B-3 into Eq. B-1, the balance condition becomes

$$[X_N^{i,j,k}][\phi_N^{i,j,k}] + [X_S^{i,j,k}][\phi_S^{i,j,k}] + [X_E^{i,j,k}][\phi_E^{i,j,k}]$$
$$+ [X_W^{i,j,k}][\phi_W^{i,j,k}] + [X_T^{i,j,k}][\phi_T^{i,j,k}] + [X_B^{i,j,k}][\phi_B^{i,j,k}]$$
$$+ [X_C^{i,j,k}][\phi_c^{i,j,k}] = [0] \tag{B-4}$$

where

$$[X_C^{i,j,k}] \equiv [X_0^{i,j,k}] + V_c[\bar{M}^{i,j,k}]$$

Equation B-4 is the mesh-point-centered finite difference equation for corner point (i,j,k). This equation was directly derived from the multigroup, neutron diffusion equation.

In order to obtain an equation involving only node corner point fluxes and line averaged fluxes, it is necessary to eliminate from Eq. B-4 the fine-mesh point fluxes corresponding to points N, S, E, W, T and B. This can be accomplished by using Eq. 2-7. For points along node lines, Eq. 2-7 simplifies; thus, fine-mesh point fluxes along node lines can be expressed as a linear function of the two corner point fluxes and the averaged flux along that line. Thus,

$$[\phi_N^{i,j,k}] \equiv [C_{1,N}^{i-1,j,k}][\phi_c^{i-1,j,k}] + [C_{2,N}^{i-1,j,k}][\phi_c^{i,j,k}] + [S_{1,N}^{i-1,j,k}][\bar{\phi}_x^{i-1,j,k}]$$

$$[\phi_S^{i,j,k}] \equiv [C_{1,S}^{i,j,k}][\phi_c^{i,j,k}] + [C_{2,S}^{i,j,k}][\phi_c^{i+1,j,k}] + [S_{1,S}^{i,j,k}][\bar{\phi}_x^{i,j,k}]$$

$$[\phi_E^{i,j,k}] \equiv [C_{1,E}^{i,j,k}][\phi_c^{i,j,k}] + [C_{4,E}^{i,j,k}][\phi_c^{i,j+1,k}] + [S_{4,E}^{i,j,k}][\bar{\phi}_y^{i,j,k}]$$

$$[\phi_W^{i,j,k}] \equiv [C_{1,W}^{i,j-1,k}][\phi_c^{i,j-1,k}] + [C_{4,W}^{i,j-1,k}][\phi_c^{i,j,k}] + [S_{4,W}^{i,j-1,k}][\bar{\phi}_y^{i,j-1,k}]$$

$$[\phi_T^{i,j,k}] \equiv [C_{1,T}^{i,j,k}][\phi_c^{i,j,k}] + [C_{5,T}^{i,j,k}][\phi_c^{i,j,k+1}] + [S_{9,T}^{i,j,k}][\bar{\phi}_z^{i,j,k}]$$

$$[\phi_B^{i,j,k}] \equiv [C_{1,B}^{i,j,k-1}][\phi_c^{i,j,k-1}] + [C_{5,B}^{i,j,k-1}][\phi_c^{i,j,k}] + [S_{9,B}^{i,j,k-1}][\bar{\phi}_z^{i,j,k-1}] \qquad \text{(B-5)}$$

The coefficients $[C_{n,p}]$, $(n = 1,2,4,5)$ and $[S_{m,p}]$, $(m = 1,4,9)$ are $G \times G$ diagonal matrices whose elements are the functions $C_n(x,y,z)$ and $S_m(x,y,z)$ defined in Appendix A and particularized for fine-mesh points p, $(p = N, S, E, W, T, B)$. The coordinates of the points p, with respect to a Cartesian coordinate system with its origin at the node center, are given by

$$N \equiv \left(\frac{h_x^{i-1}}{2} - h_N, \frac{-h_y^j}{2}, \frac{-h_z^k}{2}\right)$$

$$S \equiv \left(\frac{-h_x^i}{2} + h_s, \frac{-h_y^j}{2}, \frac{-h_z^k}{2}\right)$$

$$E \equiv \left(\frac{-h_x^i}{2}, \frac{-h_y^j}{2} + h_E, \frac{-h_z^k}{2}\right)$$

$$W \equiv \left(\frac{-h_x^i}{2}, \frac{h_y^{j-1}}{2} - h_W, \frac{-h_z^k}{2}\right)$$

$$T \equiv \left(\frac{-h_x^i}{2}, \frac{-h_y^j}{2}, \frac{-h_z^k}{2} + h_T\right)$$

$$B \equiv \left(\frac{-h_x^i}{2}, \frac{-h_y^j}{2}, \frac{h_z^{k-1}}{2} + h_B\right)$$

where

h_x^i = length of node (i,j,k) in the X direction

h_y^j = length of node (i,j,k) in the Y direction

h_z^k = length of node (i,j,k) in the Z direction

For example,

$$[C_{1,N}^{i-1,j,k}] \equiv \left[C_1^{i-1,j,k}\left(\frac{h_x^{i-1}}{2} - h_N, \frac{-h_y^j}{2}, \frac{-h_z^k}{2}\right)\right]$$

$$[S_{4,W}^{i,j-1,k}] \equiv \left[S_{4,W}^{i,j-1,k}\left(\frac{-h_x^i}{2}, \frac{h_y^{j-1}}{2} - h_W, \frac{-h_z^k}{2}\right)\right]$$

Introducing the relations given in Eq. B-5 into Eq. B-4, the following equation is obtained:

$$\begin{aligned}
&[P_N^{i,j,k}][\phi_c^{i-1,j,k}] + [P_S^{i,j,k}][\phi_c^{i+1,j,k}] + [P_E^{i,j,k}][\phi_c^{i,j+1,k}] \\
&+ [P_W^{i,j,k}][\phi_c^{i,j-1,k}] + [P_T^{i,j,k}][\phi_c^{i,j,k+1}] + [P_B^{i,j,k}][\phi_c^{i,j,k-1}] \\
&+ [P_C^{i,j,k}][\phi_c^{i,j,k}] + [\bar{P}_N^{i,j,k}][\bar{\phi}_x^{i-1,j,k}] + [\bar{P}_S^{i,j,k}][\bar{\phi}_x^{i,j,k}] \\
&+ [\bar{P}_E^{i,j,k}][\bar{\phi}_y^{i,j,k}] + [\bar{P}_W^{i,j,k}][\bar{\phi}_y^{i,j-1,k}] + [\bar{P}_T^{i,j,k}][\bar{\phi}_z^{i,j,k}] \\
&+ [\bar{P}_B^{i,j,k}][\bar{\phi}_z^{i,j,k-1}] = [0] \qquad \text{(B-6)}
\end{aligned}$$

where

$$[P_N^{i,j,k}] \equiv [X_N^{i,j,k}][C_{1,N}^{i-1,j,k}]$$

$$[P_S^{i,j,k}] \equiv [X_S^{i,j,k}][C_{2,S}^{i,j,k}]$$

$$[P_E^{i,j,k}] \equiv [X_E^{i,j,k}][C_{4,E}^{i,j,k}]$$

$$[P_W^{i,j,k}] \equiv [X_W^{i,j,k}][C_{1,W}^{i,j-1,k}]$$

$$[P_T^{i,j,k}] \equiv [X_T^{i,j,k}][C_{5,T}^{i,j,k}]$$

$$[P_B^{i,j,k}] \equiv [X_B^{i,j,k}][C_{1,B}^{i,j,k-1}]$$

$$[P_C^{i,j,k}] \equiv [X_N^{i,j,k}][C_{2,N}^{i-1,j,k}] + [X_S^{i,j,k}][C_{1,S}^{i,j,k}] + [X_E^{i,j,k}][C_{1,E}^{i,j,k}]$$
$$+ [X_W^{i,j,k}][C_{4,W}^{i,j-1,k}] + [X_T^{i,j,k}][C_{1,T}^{i,j,k}]$$
$$+ [X_B^{i,j,k}][C_{5,B}^{i,j,k-1}] + [X_C^{i,j,k}]$$

$$[\bar{P}_N^{i,j,k}] \equiv [X_N^{i,j,k}][S_{1,N}^{i-1,j,k}]$$

$$[\bar{P}_S^{i,j,k}] \equiv [X_S^{i,j,k}][S_{1,S}^{i,j,k}]$$

$$[\bar{P}_E^{i,j,k}] \equiv [X_E^{i,j,k}][S_{4,E}^{i,j,k}]$$

$$[\bar{P}_W^{i,j,k}] \equiv [X_W^{i,j,k}][S_{4,W}^{i,j-1,k}]$$

$$[\bar{P}_T^{i,j,k}] \equiv [X_T^{i,j,k}][S_{9,T}^{i,j,k}]$$

$$[\bar{P}_B^{i,j,k}] \equiv [X_B^{i,j,k}][S_{9,B}^{i,j,k-1}]$$

Equation B-6 is the corner point balance equation which couples 7 corner point fluxes, $[\phi_c]$, and 6 node line averaged fluxes, $[\bar{\phi}_u]$, (u = x, y, z).

Appendix C

DERIVATION OF THE BALANCE EQUATION ALONG NODE LINES

The balance equation along node lines can be derived by integrating the multigroup neutron diffusion equation, Eq. 1-1, over the volume, v_L, of the line cell about node line L. Application of this balance condition along a node line parallel to the X axis yields to the following equation:

$$\int_{v_L} -\underline{\nabla} \cdot [D(\underline{r})]\underline{\nabla}[\phi(\underline{r})]dv + \int_{v_L} [M(\underline{r})][\phi(\underline{r})]dv = [0] \qquad (C\text{-}1)$$

Applying Gauss's theorem and calculating the partial derivatives at the mesh cell faces by the centered finite difference approximation yields for the first term in Eq. C-1:

$$- \int_{S_L} [D(\underline{r})]\underline{\nabla}[\phi(\underline{r})] \cdot \underline{n}\, ds = - \sum_{\alpha=2}^{p-1} \left\{ \int_{S_{E,\alpha}} [D(\underline{r})] \frac{\left[\phi_{E,\alpha}^{i,j,k}\right] - \left[\phi_{L,\alpha}^{i,j,k}\right]}{h_E}\, ds \right.$$

$$+ \int_{S_{W,\alpha}} [D(\underline{r})] \frac{\left[\phi_{W,\alpha}^{i,j,k}\right] - \left[\phi_{L,\alpha}^{i,j,k}\right]}{h_W}\, ds + \int_{S_{T,\alpha}} [D(\underline{r})] \frac{\left[\phi_{T,\alpha}^{i,j,k}\right] - \left[\phi_{L,\alpha}^{i,j,k}\right]}{h_T}\, ds$$

$$\left. + \int_{S_{B,\alpha}} [D(\underline{r})] \frac{\left[\phi_{B,\alpha}^{i,j,k}\right] - \left[\phi_{L,\alpha}^{i,j,k}\right]}{h_B}\, ds \right\} - \int_{S_N} [D(\underline{r})] \frac{\left[\phi_c^{i,j,k}\right] - \left[\phi_{L,2}^{i,j,k}\right]}{h_N}\, ds$$

$$- \int_{S_S} [D(\underline{r})] \frac{\left[\phi_c^{i+1,j,k}\right] - \left[\phi_{L,p-1}^{i,j,k}\right]}{h_S}\, ds$$

$$\equiv \sum_{\alpha=2}^{p-1} \left\{ [R_{0,\alpha}^{i,j,k}][\phi_{L,\alpha}^{i,j,k}] + [R_{E,\alpha}^{i,j,k}][\phi_{E,\alpha}^{i,j,k}] + [R_{W,\alpha}^{i,j,k}][\phi_{W,\alpha}^{i,j,k}] \right.$$

(Continued)

$$+ [R_{T,\alpha}^{i,j,k}][\phi_{T,\alpha}^{i,j,k}] + [R_{B,\alpha}^{i,j,k}][\phi_{B,\alpha}^{i,j,k}]\Big\}$$

$$+ [R_{N}^{i,j,k}] \cdot \left([\phi_{c}^{i,j,k}] - [\phi_{L,2}^{i,j,k}]\right)$$

$$+ [R_{S}^{i,j,k}] \cdot \left([\phi_{c}^{i+1,j,k}] - [\phi_{L,p-1}^{i,j,k}]\right) \qquad \text{(C-2)}$$

where

α is a dummy index referring to the fine-mesh points on the node line and the four, parallel, nearest neighbor lines. (In this notation, $[\phi_{L,1}^{i,j,k}]$ and $[\phi_{L,p}^{i,j,k}]$ would be the corner point fluxes $[\phi_{c}^{i,j,k}]$ and $[\phi_{c}^{i+1,j,k}]$.)

$[\phi_{c}^{i,j,k}]$ is a column vector of length G containing the corner point fluxes at point (i,j,k).

$[\phi_{L,\alpha}^{i,j,k}]$, $[\phi_{E,\alpha}^{i,j,k}]$, $[\phi_{W,\alpha}^{i,j,k}]$, $[\phi_{T,\alpha}^{i,j,k}]$, $[\phi_{B,\alpha}^{i,j,k}]$ are column vectors of length G containing the neutron fluxes at fine-mesh points L_α, E_α, W_α, T_α and B_α which are shown in Fig. C-1.

S_L is the total line cell surface.

$S_{E,\alpha}$, $S_{W,\alpha}$, $S_{T,\alpha}$, $S_{B,\alpha}$ are the faces of the mesh cell about mesh point L_α corresponding to the east, west, top, and bottom directions.

S_N is the surface corresponding to the north face of the line cell.

S_S is the surface corresponding to the south face of the line cell.

h_E, h_W, h_T, h_B, h_N, h_S are mesh distances between neighboring fine-mesh points as shown in Fig. C-1.

The coefficients $[R^{i,j,k}]$ are $G \times G$ diagonal matrices defined by the following expressions:

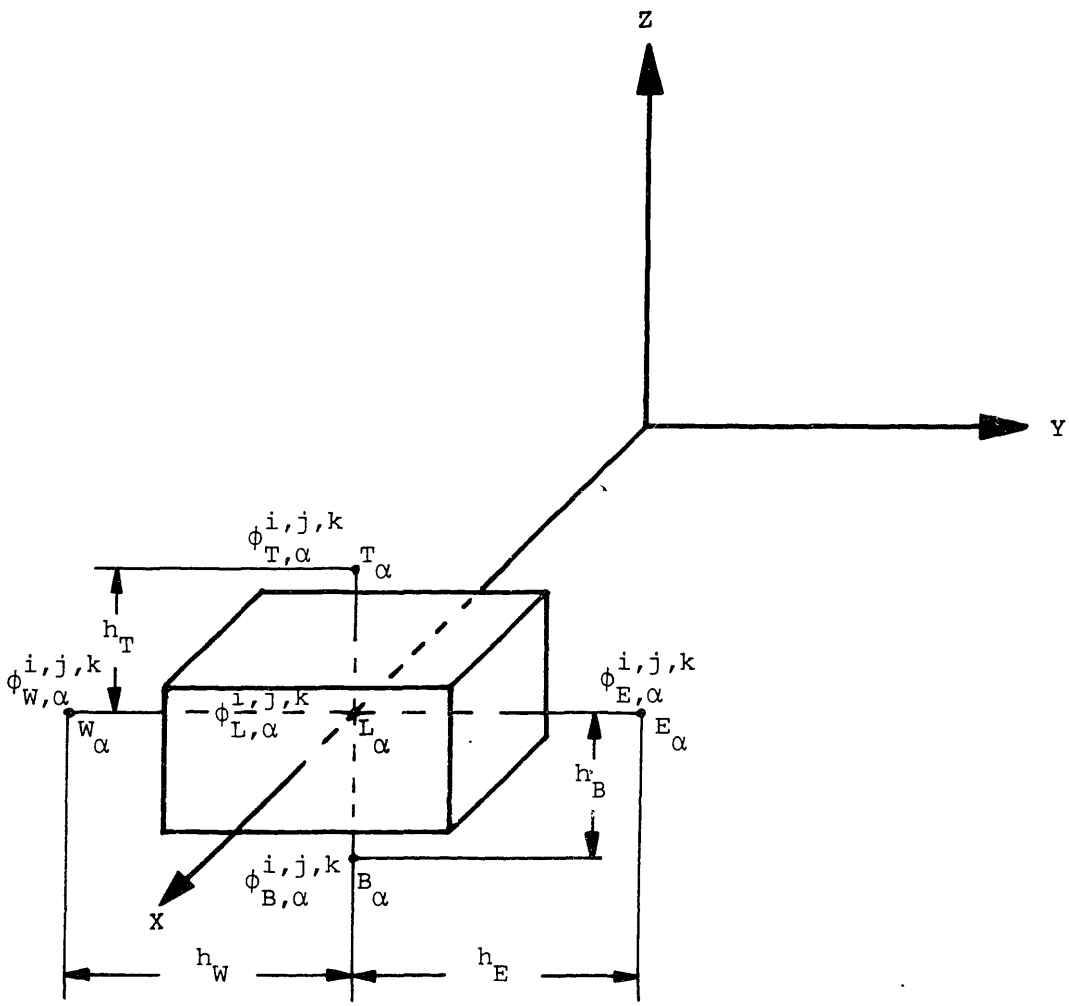

Fig. C-1. Geometry and nomenclature for the balance equation along node lines.

$$[R_{E,\alpha}^{i,j,k}] \equiv -\frac{1}{h_E}\int_{S_{E,\alpha}} [D(\underline{r})]\, ds$$

$$[R_{W,\alpha}^{k,j,k}] \equiv -\frac{1}{h_W}\int_{S_{W,\alpha}} [D(\underline{r})]\, ds$$

$$[R_{T,\alpha}^{i,j,k}] \equiv -\frac{1}{h_T}\int_{S_{T,\alpha}} [D(\underline{r})]\, ds$$

$$[R_{B,\alpha}^{i,j,k}] \equiv -\frac{1}{h_B}\int_{S_{B,\alpha}} [D(\underline{r})]\, ds$$

$$[R_{N}^{i,j,k}] \equiv -\frac{1}{h_N}\int_{S_{N}} [D(\underline{r})]\, ds$$

$$[R_{S}^{i,j,k}] \equiv -\frac{1}{h_S}\int_{S_{S}} [D(\underline{r})]\, ds$$

$$[R_{0}^{i,j,k}] \equiv -\left\{[R_{E,\alpha}^{i,j,k}] + [R_{W,\alpha}^{i,j,k}] + [R_{T,\alpha}^{i,j,k}] + [R_{B,\alpha}^{i,j,k}]\right\}$$

The second term in Eq. C-1 may be written as:

$$\sum_{\alpha=2}^{p-1}\int_{v_\alpha} [M(\underline{r})][\phi(\underline{r})]\, dv = \sum_{\alpha=2}^{p-1}\left(\int_{v_\alpha} [M(\underline{r})]\, dv\right)[\phi_{L,\alpha}^{i,j,k}]$$

$$\equiv \sum_{\alpha=2}^{p-1} V_\alpha [\bar{M}_\alpha^{i,j,k}][\phi_{L,\alpha}^{i,j,k}] \qquad \text{(C-3)}$$

where

V_α is the mesh cell volume corresponding to mesh point L_α

and

$$[\bar{M}_\alpha^{i,j,k}] \equiv \frac{1}{V_\alpha}\int_{v_\alpha} [M(\underline{r})]\, dv$$

Introducing expressions given by Eqs. C-2 and C-3 into Eq. C-1 leads to the balance condition:

$$\sum_{\alpha=2}^{p-1} \Big\{ [R_{L,\alpha}^{i,j,k}][\phi_{L,\alpha}^{i,j,k}] + [R_{E,\alpha}^{i,j,k}][\phi_{E,\alpha}^{i,j,k}] + [R_{W,\alpha}^{i,j,k}][\phi_{W,\alpha}^{i,j,k}] + [R_{T,\alpha}^{i,j,k}][\phi_{T,\alpha}^{i,j,k}] + [R_{B,\alpha}^{i,j,k}][\phi_{B,\alpha}^{i,j,k}] \Big\} + [R_{N}^{i,j,k}] \left([\phi_{c}^{i,j,k}] - [\phi_{L,2}^{i,j,k}] \right) + [R_{S}^{i,j,k}] \left([\phi_{c}^{i+1,j,k}] - [\phi_{L,p-1}^{i,j,k}] \right) = [0] \qquad \text{(C-4)}$$

where

$$[R_{L,\alpha}^{i,j,k}] \equiv [R_{0,\alpha}^{i,j,k}] + V_{\alpha}[\bar{M}_{\alpha}^{i,j,k}]$$

Equation C-4 is the mesh-point-centered, finite difference equation for a node line parallel to the X axis. This equation was directly derived from the multigroup neutron diffusion equation. In order to obtain an equation involving only node corner point fluxes and line averaged fluxes, it is necessary to eliminate from Eq. C-4 the fine-mesh point fluxes corresponding to points L_{α}, E_{α}, W_{α}, T_{α} and B_{α}. This can be achieved by means of Eq. 2-7.

For points along node faces, Eq. 2-7 simplifies; thus, fine-mesh point fluxes along node faces can be expressed as a linear function of the 4 corner point fluxes, the 4 line averaged fluxes and the face averaged flux corresponding to such node face. The result is:

$$[\phi_{E,\alpha}^{i,j,k}] = [C_{1,E,\alpha}^{i,j,k}][\phi_{c}^{i,j,k}] + [C_{2,E,\alpha}^{i,j,k}][\phi_{c}^{i+1,j,k}] + [C_{3,E,\alpha}^{i,j,k}][\phi_{c}^{i+1,j+1,k}] + [C_{4,E,\alpha}^{i,j,k}][\phi_{c}^{i,j+1,k}] + [S_{1,E,\alpha}^{i,j,k}][\bar{\phi}_{x}^{i,j,k}] + [S_{2,E,\alpha}^{i,j,k}][\bar{\phi}_{x}^{i,j+1,k}] + [S_{3,E,\alpha}^{i,j,k}][\bar{\phi}_{y}^{i+1,j,k}] + [S_{4,E,\alpha}^{i,j,k}][\bar{\phi}_{y}^{i,j,k}] + [V_{5,E,\alpha}^{i,j,k}][\bar{\phi}_{z}^{i,j,k}]$$

(Continued)

$$[\phi^{i,j,k}_{W,\alpha}] = [C^{i,j-1,k}_{1,W,\alpha}][\phi^{i,j-1,k}_{c}] + [C^{i,j-1,k}_{2,W,\alpha}][\phi^{i+1,j-1,k}_{c}] + [C^{i,j-1,k}_{3,W,\alpha}][\phi^{i+1,j,k}_{c}]$$
$$+ [C^{i,j-1,k}_{4,W,\alpha}][\phi^{i,j,k}_{c}] + [S^{i,j-1,k}_{1,W,\alpha}][\bar{\phi}^{i,j-1,k}_{x}] + [S^{i,j-1,k}_{2,W,\alpha}][\bar{\phi}^{i,j,k}_{x}]$$
$$+ [S^{i,j-1,k}_{3,W,\alpha}][\bar{\phi}^{i+1,j-1,k}_{y}] + [S^{i,j-1,k}_{4,W,\alpha}][\bar{\phi}^{i,j-1,k}_{y}] + [V^{i,j-1,k}_{5,W,\alpha}][\bar{\bar{\phi}}^{i,j-1,k}_{z}]$$

$$[\phi^{i,j,k}_{T,\alpha}] = [C^{i,j,k}_{1,T,\alpha}][\phi^{i,j,k}_{c}] + [C^{i,j,k}_{2,T,\alpha}][\phi^{i+1,j,k}_{c}] + [C^{i,j,k}_{5,T,\alpha}][\phi^{i,j,k+1}_{c}]$$
$$+ [C^{i,j,k}_{6,T,\alpha}][\phi^{i+1,j,k+1}_{c}] + [S^{i,j,k}_{1,T,\alpha}][\bar{\phi}^{i,j,k}_{x}] + [S^{i,j,k}_{5,T,\alpha}][\bar{\phi}^{i,j,k+1}_{x}]$$
$$+ [S^{i,j,k}_{9,T,\alpha}][\bar{\phi}^{i,j,k}_{z}] + [S^{i,j,k}_{10,T,\alpha}][\bar{\phi}^{i+1,j,k}_{z}] + [V^{i,j,k}_{1,T,\alpha}][\bar{\bar{\phi}}^{i,j,k}_{y}]$$

$$[\phi^{i,j,k}_{B,\alpha}] = [C^{i,j,k-1}_{1,B,\alpha}][\phi^{i,j,k-1}_{c}] + [C^{i,j,k-1}_{2,B,\alpha}][\phi^{i+1,j,k-1}_{c}] + [C^{i,j,k-1}_{5,B,\alpha}][\phi^{i,j,k}_{c}]$$
$$+ [C^{i,j,k-1}_{6,B,\alpha}][\phi^{i+1,j,k}_{c}] + [S^{i,j,k-1}_{1,B,\alpha}][\bar{\phi}^{i,j,k-1}_{x}] + [S^{i,j,k-1}_{5,B,\alpha}][\bar{\phi}^{i,j,k}_{x}]$$
$$+ [S^{i,j,k-1}_{9,B,\alpha}][\bar{\phi}^{i,j,k-1}_{z}] + [S^{i,j,k-1}_{10,B,\alpha}][\bar{\phi}^{i+1,j,k-1}_{z}] + [V^{i,j,k-1}_{1,B,\alpha}][\bar{\bar{\phi}}^{i,j,k-1}_{y}]$$

$$[\phi^{i,j,k}_{L,\alpha}] = [C^{i,j,k}_{1,L,\alpha}][\phi^{i,j,k}_{c}] + [C^{i,j,k}_{2,L,\alpha}][\phi^{i+1,j,k}_{c}] + [S^{i,j,k}_{1,L,\alpha}][\bar{\phi}^{i,j,k}_{x}]$$

(C-5)

The coefficients $[C_{n,p,\alpha}]$, $(n = 1, \ldots, 6)$, $[S_{m,p,\alpha}]$, $(m = 1, 2, 3, 4, 5, 9, 10)$, $[V_{\ell,p,\alpha}]$, $(\ell = 1, 5)$ are G × G diagonal matrices whose elements are the functions $C_n(x,y,z)$, $S_m(x,y,z)$, $V_\ell(x,y,z)$ defined in Appendix A and particularized for fine-mesh points P_α, ($P_\alpha = L_\alpha$, E_α, W_α, T_α, B_α). The coordinates of the points P_α with respect to a Cartesian coordinate system with its origin at the node center, are given by:

$$L_\alpha \equiv \left(x_\alpha, \frac{-h_y^j}{2}, \frac{-h_z^k}{2}\right)$$

$$E_\alpha \equiv \left(x_\alpha, \frac{-h_y^j}{2} + h_E, \frac{-h_z^k}{2}\right)$$

$$W_\alpha \equiv \left(x_\alpha, \frac{h_y^{j-1}}{2} - h_W, \frac{-h_z^k}{2}\right)$$

$$T_\alpha \equiv \left(x_\alpha, \frac{-h_y^j}{2}, \frac{-h_z^k}{2} + h_T\right)$$

$$B_\alpha \equiv \left(x_\alpha, \frac{-h_y^j}{2}, \frac{h_z^{k-1}}{2} - h_B\right)$$

where

x_α is the X coordinate of fine-mesh point L_α,

h_x^i, h_y^j, h_z^k are the lengths of node (i,j,k) in the X, Y and Z directions.

For example,

$$[C_{1,E,\alpha}^{i,j,k}] \equiv \left[C_1^{i,j,k}\left(x_\alpha, \frac{-h_y^j}{2} + h_E, \frac{-h_z^k}{2}\right)\right]$$

$$[V_{1,T,\alpha}^{i,j,k}] \equiv \left[V_1^{i,j,k}\left(x_\alpha, \frac{-h_y^j}{2}, \frac{-h_z^k}{2} + h_T\right)\right]$$

Introducing the relations given by Eq. C-5 into Eq. C-4, the following equation is obtained:

$$[A^{i,j,k}_{x,C}][\bar{\phi}^{i,j,k}_{x}] + [A^{i,j,k}_{x,T}][\bar{\phi}^{i,j,k+1}_{x}] + [A^{i,j,k}_{x,B}][\bar{\phi}^{i,j,k-1}_{x}]$$

$$+ [A^{i,j,k}_{x,E}][\bar{\phi}^{i,j+1,k}_{x}] + [A^{i,j,k}_{x,W}][\bar{\phi}^{i,j-1,k}_{x}] + [N^{i,j,k}_{x,C}][\phi^{i,j,k}_{c}]$$

$$+ [N^{i,j,k}_{x,T}][\phi^{i,j,k+1}_{c}] + [N^{i,j,k}_{x,B}][\phi^{i,j,k-1}_{c}] + [N^{i,j,k}_{x,E}][\phi^{i,j+1,k}_{c}]$$

$$+ [N^{i,j,k}_{x,W}][\phi^{i,j-1,k}_{c}] + [S^{i,j,k}_{x,C}][\phi^{i+1,j,k}_{c}] + [S^{i,j,k}_{x,T}][\phi^{i+1,j,k+1}_{c}]$$

$$+ [S^{i,j,k}_{x,B}][\phi^{i+1,j,k-1}_{c}] + [S^{i,j,k}_{x,E}][\phi^{i+1,j+1,k}_{c}] + [S^{i,j,k}_{x,W}][\phi^{i+1,j-1,k}_{c}]$$

$$+ [\bar{N}^{i,j,k}_{x,T}][\bar{\phi}^{i,j,k}_{z}] + [\bar{N}^{i,j,k}_{x,B}][\bar{\phi}^{i,j,k-1}_{z}] + [\bar{N}^{i,j,k}_{x,E}][\bar{\phi}^{i,j,k}_{y}]$$

$$+ [\bar{N}^{i,j,k}_{x,W}][\bar{\phi}^{i,j-1,k}_{y}] + [\bar{S}^{i,j,k}_{x,T}][\bar{\phi}^{i+1,j,k}_{z}] + [\bar{S}^{i,j,k}_{x,B}][\bar{\phi}^{i+1,j,k-1}_{z}]$$

$$+ [\bar{S}^{i,j,k}_{x,E}][\bar{\phi}^{i+1,j,k}_{y}] + [\bar{S}^{i,j,k}_{x,W}][\bar{\phi}^{i+1,j-1,k}_{y}] = [R^{i,j,k}_{x}] \qquad \text{(C-6)}$$

where

$$[A^{i,j,k}_{x,T}] \equiv \sum_{\alpha=2}^{p-1} [R^{i,j,k}_{T,\alpha}][S^{i,j,k}_{5,T,\alpha}]$$

$$[A^{i,j,k}_{x,B}] \equiv \sum_{\alpha=2}^{p-1} [R^{i,j,k}_{B,\alpha}][S^{i,j,k-1}_{1,B,\alpha}]$$

$$[A^{i,j,k}_{x,E}] \equiv \sum_{\alpha=2}^{p-1} [R^{i,j,k}_{E,\alpha}][S^{i,j,k}_{2,E,\alpha}]$$

$$[A^{i,j,k}_{x,W}] \equiv \sum_{\alpha=2}^{p-1} [P^{i,j,k}_{W,\alpha}][S^{i,j-1,k}_{1,W,\alpha}]$$

$$[A^{i,j,k}_{x,C}] \equiv \sum_{\alpha=2}^{p-1} \Big\{ [R^{i,j,k}_{L,\alpha}][S^{i,j,k}_{1,L,\alpha}] + [R^{i,j,k}_{E,\alpha}][S^{i,j,k}_{1,E,\alpha}] + [R^{i,j,k}_{W,\alpha}][S^{i,j-1,k}_{2,W,\alpha}] + [R^{i,j,k}_{T,\alpha}][S^{i,j,k}_{1,T,\alpha}] + [R^{i,j,k}_{B,\alpha}][S^{i,j,k-1}_{5,B,\alpha}] \Big\} - [R^{i,j,k}_{N}][S^{i,j,k}_{1,L,2}] - [R^{i,j,k}_{S}][S^{i,j,k}_{1,L,p-1}]$$

$$[N^{i,j,k}_{x,T}] \equiv \sum_{\alpha=2}^{p-1} [R^{i,j,k}_{T,\alpha}][C^{i,j,k}_{5,T,\alpha}]$$

$$[N^{i,j,k}_{x,B}] \equiv \sum_{\alpha=2}^{p-1} [R^{i,j,k}_{B,\alpha}][C^{i,j,k-1}_{1,B,\alpha}]$$

$$[N^{i,j,k}_{x,E}] \equiv \sum_{\alpha=2}^{p-1} [R^{i,j,k}_{E,\alpha}][C^{i,j,k}_{4,E,\alpha}]$$

$$[N^{i,j,k}_{x,W}] \equiv \sum_{\alpha=2}^{p-1} [R^{i,j,k}_{W,\alpha}][C^{i,j-1,k}_{1,W,\alpha}]$$

$$[N^{i,j,k}_{x,C}] \equiv \sum_{\alpha=2}^{p-1} \Big\{ [R^{i,j,k}_{L,\alpha}][C^{i,j,k}_{1,L,\alpha}] + [R^{i,j,k}_{E,\alpha}][C^{i,j,k}_{1,E,\alpha}] + [R^{i,j,k}_{W,\alpha}][C^{i,j-1,k}_{4,W,\alpha}] + [R^{i,j,k}_{T,\alpha}][C^{i,j,k}_{1,T,\alpha}] + [R^{i,j,k}_{B,\alpha}][C^{i,j,k-1}_{5,B,\alpha}] \Big\} + [R^{i,j,k}_{N}]\Big(1 - [C^{i,j,k}_{1,L,2}]\Big) - [R^{i,j,k}_{S}][C^{i,j,k}_{1,L,p-1}]$$

$$[S^{i,j,k}_{x,T}] \equiv \sum_{\alpha=2}^{p-1} [R^{i,j,k}_{T,\alpha}][C^{i,j,k}_{6,T,\alpha}]$$

$$[S^{i,j,k}_{x,B}] \equiv \sum_{\alpha=2}^{p-1} [R^{i,j,k}_{B,\alpha}][C^{i,j,k-1}_{2,B,\alpha}]$$

$$[S^{i,j,k}_{x,E}] \equiv \sum_{\alpha=2}^{p-1} [R^{i,j,k}_{E,\alpha}][C^{i,j,k}_{3,E,\alpha}]$$

$$[S^{i,j,k}_{x,W}] \equiv \sum_{\alpha=2}^{p-1} [R^{i,j,k}_{W,\alpha}][C^{i,j-1,k}_{2,W,\alpha}]$$

$$[S^{i,j,k}_{x,C}] \equiv \sum_{\alpha=2}^{p-1} \Big\{[R^{i,j,k}_{L,\alpha}][C^{i,j,k}_{2,L,\alpha}] + [R^{i,j,k}_{E,\alpha}][C^{i,j,k}_{2,E,\alpha}] + [R^{i,j,k}_{W,\alpha}][C^{i,j-1,k}_{3,W,\alpha}] + [R^{i,j,k}_{T,\alpha}][C^{i,j,k}_{2,T,\alpha}] + [R^{i,j,k}_{B,\alpha}][C^{i,j,k-1}_{6,B,\alpha}]\Big\} - [R^{i,j,k}_{N}][C^{i,j,k}_{2,L,2}] + [R^{i,j,k}_{S}]\left(1 - [C^{i,j,k}_{2,L,p-1}]\right)$$

$$[\bar{N}^{i,j,k}_{x,T}] \equiv \sum_{\alpha=2}^{p-1} [R^{i,j,k}_{T,\alpha}][S^{i,j,k}_{9,T,\alpha}]$$

$$[\bar{N}^{i,j,k}_{x,B}] \equiv \sum_{\alpha=2}^{p-1} [R^{i,j,k}_{B,\alpha}][S^{i,j,k-1}_{9,B,\alpha}]$$

$$[\bar{N}^{i,j,k}_{x,E}] \equiv \sum_{\alpha=2}^{p-1} [R^{i,j,k}_{E,\alpha}][S^{i,j,k}_{4,E,\alpha}]$$

$$[\bar{N}^{i,j,k}_{x,W}] \equiv \sum_{\alpha=2}^{p-1} [R^{i,j,k}_{W,\alpha}][S^{i,j-1,k}_{4,W,\alpha}]$$

$$[\bar{S}^{i,j,k}_{x,T}] \equiv \sum_{\alpha=2}^{p-1} [R^{i,j,k}_{T,\alpha}][S^{i,j,k}_{10,T,\alpha}]$$

$$[\bar{S}^{i,j,k}_{x,B}] \equiv \sum_{\alpha=2}^{p-1} [R^{i,j,k}_{B,\alpha}][S^{i,j,k-1}_{10,B,\alpha}]$$

$$[\bar{S}^{i,j,k}_{x,E}] \equiv \sum_{\alpha=2}^{p-1} [R^{i,j,k}_{E,\alpha}][S^{i,j,k}_{3,E,\alpha}]$$

$$[\bar{S}^{i,j,k}_{x,W}] \equiv \sum_{\alpha=2}^{p-1} [R^{i,j,k}_{W,\alpha}][S^{i,j-1,k}_{3,W,\alpha}]$$

$$[R^{i,j,k}_{x}] \equiv -\left\{ \sum_{\alpha=2}^{p-1} [R^{i,j,k}_{E,\alpha}][V^{i,j,k}_{5,E,\alpha}][\bar{\bar{\phi}}^{i,j,k}_{z}] \right.$$

$$+ \sum_{\alpha=2}^{p-1} [R^{i,j,k}_{W,\alpha}][V^{i,j-1,k}_{5,W,\alpha}][\bar{\bar{\phi}}^{i,j-1,k}_{z}]$$

$$+ \sum_{\alpha=2}^{p-1} [R^{i,j,k}_{T,\alpha}][V^{i,j,k}_{1,T,\alpha}][\bar{\bar{\phi}}^{i,j,k}_{y}]$$

$$\left. + \sum_{\alpha=2}^{p-1} [R^{i,j,k}_{B,\alpha}][V^{i,j,k-1}_{1,B,\alpha}][\bar{\bar{\phi}}^{i,j,k-1}_{y}] \right\}$$

Equation C-6 is the balance equation along a node line parallel to the X axis. This equation couples 10 corner point fluxes and 13 node line averaged fluxes.

A similar equation can be derived for the node lines parallel to the Y axis. Thus,

$$[A^{i,j,k}_{y,C}][\bar{\phi}^{i,j,k}_{y}] + [A^{i,j,k}_{y,N}][\bar{\phi}^{i-1,j,k}_{y}] + [A^{i,j,k}_{y,S}][\bar{\phi}^{i+1,j,k}_{y}]$$

$$+ [A^{i,j,k}_{y,T}][\bar{\phi}^{i,j,k+1}_{y}] + [A^{i,j,k}_{y,B}][\bar{\phi}^{i,j,k-1}_{y}] + [W^{i,j,k}_{y,C}][\phi^{i,j,k}_{c}]$$

$$+ [W^{i,j,k}_{y,T}][\phi^{i,j,k+1}_{c}] + [W^{i,j,k}_{y,B}][\phi^{i,j,k-1}_{c}] + [W^{i,j,k}_{y,N}][\phi^{i-1,j,k}_{c}]$$

$$+ [W^{i,j,k}_{y,S}][\phi^{i+1,j,k}_{c}] + [E^{i,j,k}_{y,C}][\phi^{i,j+1,k}_{c}] + [E^{i,j,k}_{y,T}][\phi^{i,j+1,k+1}_{c}]$$

$$+ [E^{i,j,k}_{y,B}][\phi^{i,j+1,k-1}_{c}] + [E^{i,j,k}_{y,N}][\phi^{i-1,j+1,k}_{c}] + [E^{i,j,k}_{y,S}][\phi^{i+1,j+1,k}_{c}]$$

$$+ [\bar{W}^{i,j,k}_{y,T}][\bar{\phi}^{i,j,k}_{z}] + [\bar{W}^{i,j,k}_{y,B}][\bar{\phi}^{i,j,k-1}_{z}] + [\bar{W}^{i,j,k}_{y,N}][\bar{\phi}^{i-1,j,k}_{x}]$$

$$+ [\bar{W}^{i,j,k}_{y,S}][\bar{\phi}^{i,j,k}_{x}] + [\bar{E}^{i,j,k}_{y,T}][\bar{\phi}^{i,j+1,k}_{z}] + [\bar{E}^{i,j,k}_{y,B}][\bar{\phi}^{i,j+1,k-1}_{z}]$$

$$+ [\bar{E}^{i,j,k}_{y,N}][\bar{\phi}^{i-1,j+1,k}_{y}] + [\bar{E}^{i,j,k}_{y,S}][\bar{\phi}^{i,j+1,k}_{y}] = [R^{i,j,k}_{y}] \qquad \text{(C-7)}$$

The equation for the node lines parallel to the Z axis can be written as:

$$[A_{z,C}^{i,j,k}][\bar{\phi}_z^{i,j,k}] + [A_{z,N}^{i,j,k}][\bar{\phi}_z^{i-1,j,k}] + [A_{z,S}^{i,j,k}][\bar{\phi}_z^{i+1,j,k}]$$
$$+ [A_{z,W}^{i,j,k}][\bar{\phi}_z^{i,j-1,k}] + [A_{z,E}^{i,j,k}][\bar{\phi}_z^{i,j+1,k}] + [T_{z,C}^{i,j,k}][\phi_c^{i,j,k+1}]$$
$$+ [T_{z,N}^{i,j,k}][\phi_c^{i-1,j,k+1}] + [T_{z,S}^{i,j,k}][\phi_c^{i+1,j,k+1}] + [T_{z,W}^{i,j,k}][\phi_c^{i,j-1,k+1}]$$
$$+ [T_{z,E}^{i,j,k}][\phi_c^{i,j+1,k+1}] + [B_{z,C}^{i,j,k}][\phi_c^{i,j,k}] + [B_{z,N}^{i,j,k}][\phi_c^{i-1,j,k}]$$
$$+ [B_{z,S}^{i,j,k}][\phi_c^{i+1,j,k}] + [B_{z,W}^{i,j,k}][\phi_c^{i,j-1,k}] + [B_{z,E}^{i,j,k}][\phi_c^{i,j+1,k}]$$
$$+ [\bar{T}_{z,N}^{i,j,k}][\bar{\phi}_x^{i-1,j,k+1}] + [\bar{T}_{z,S}^{i,j,k}][\bar{\phi}_x^{i,j,k+1}] + [\bar{T}_{z,W}^{i,j,k}][\bar{\phi}_y^{i,j-1,k+1}]$$
$$+ [\bar{T}_{z,E}^{i,j,k}][\bar{\phi}_y^{i,j,k+1}] + [\bar{B}_{z,N}^{i,j,k}][\bar{\phi}_x^{i-1,j,k}] + [\bar{B}_{z,S}^{i,j,k}][\bar{\phi}_x^{i,j,k}]$$
$$+ [\bar{B}_{z,W}^{i,j,k}][\bar{\phi}_y^{i,j-1,k}] + [\bar{B}_{z,E}^{i,j,k}][\bar{\phi}_y^{i,j,k}] = [R_z^{i,j,k}] \qquad \text{(C-8)}$$

where the coefficients for the balance equations along node lines parallel to the Y axis and Z axis, appearing in Eq. C-7 and Eq. C-8, can be obtained by the methods previously described in this appendix.

Appendix D

IMPLEMENTATION OF THE BOUNDARY CONDITIONS AT THE REACTOR SURFACES

The corner point fluxes and node line averaged fluxes required for computing the fine-mesh flux by means of Eq. 2-7 can be obtained by solving the corner point balance equation, Eq. 2-9, and the node line balance equations, Eqs. C-6, C-7 and C-8, in conjunction with the appropriate boundary conditions.

In this appendix, a simplified scheme for implementing the zero flux, zero current and albedo boundary conditions at the reactor surfaces will be discussed.

D.1 Zero Flux Boundary Condition

This boundary condition can be implemented by making $[\phi_c^{i,j,k}] = [0]$ and $[\bar{\phi}_u^{i,j,k}] = [0]$, $(u = x,y,z)$, for the corner points (i,j,k) and the node lines located in the reactor surfaces where the flux is zero.

D.2 Albedo Boundary Condition

The albedo boundary condition at the reactor surface s can be expressed as

$$[\phi_s] = [A_s][J_{u,s}]$$

or

$$[J_{u,s}] = [A_s]^{-1}[\phi_s] \qquad \text{(D-1)}$$

where

$[J_{u,s}]$ is a column vector of length G containing the u component, (u = x,y,z), of the neutron currents across surface s,

$[\phi_s]$ is a column vector of length G containing the neutron fluxes at surface s,

$[A_s]$ is a G × G matrix containing the albedo coefficients, α_{ij}, at surface s.

It is possible to treat all boundary corner points and node lines that have an albedo boundary condition as if they were interior points or interior lines by introducing an extra computational node beyond the physical limit of the reactor. The nuclear composition, C^*, of this extra node must be determined in a way such that the equation resulting from applying a neutron balance about mesh cell C_1 in Fig. D-1 with an albedo boundary condition will be equivalent to the equation obtained from a neutron balance about mesh cell C_2 in Fig. D-2 with a zero flux boundary condition.

The neutron balance equation about mesh cell C_1 in Fig. D-1 can be obtained by integrating the multigroup neutron diffusion equation over the volume, v_1, of mesh cell C_1. Thus,

$$\int_{v_1} \underline{\nabla} \cdot [\underline{J}(\underline{r})]dv + \int_{v_1} [M(\underline{r})][\phi(\underline{r})]dv = [0] \qquad \text{(D-2)}$$

Application of the Gauss theorem to the first term of Eq. D-1 yields:

$$\int_{v_1} \underline{\nabla} \cdot [\underline{J}(\underline{r})]dv = \int_{S_N} [J_{y,SN}]ds - \int_{S_S} [J_{y,SS}]ds + \int_{S_E} [J_{x,SE}]ds - \int_{S_W} [J_{x,SW}]ds$$

$$+ \int_{S_T} [J_{z,ST}]ds - \int_{S_B} [J_{z,SB}]ds \qquad \text{(D-3)}$$

$$[J_{y,SN}] = [A_{SN}]^{-1}[\phi_{SN}]$$

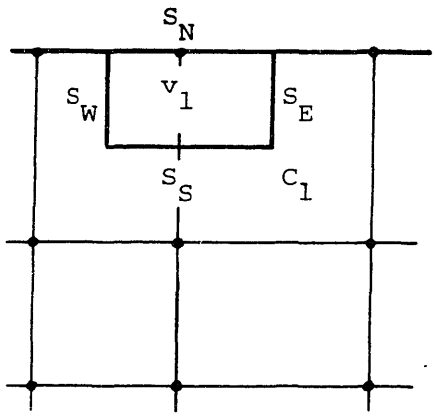

Fig. D-1. Geometry for mesh cell C_1 with an albedo boundary condition.

$$[\phi] = [0]$$

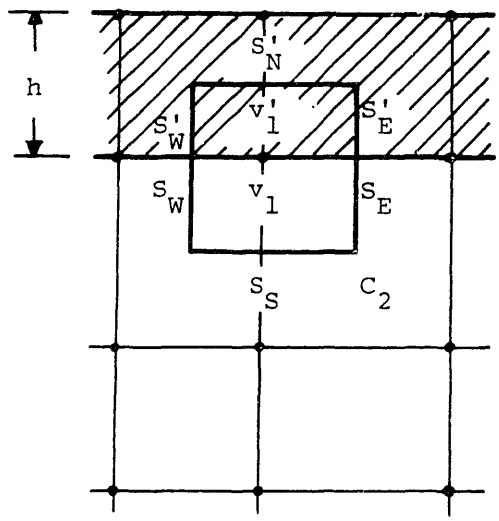

Fig. D-2. Geometry for mesh cell C_2 with a fake material and zero flux boundary condition.

where S_N, S_S, S_E, S_W, S_T, S_B are the mesh cell faces (see Fig. D-1). S_T and S_B correspond to the top and bottom faces and they are not shown in Fig. D-1. Application of Eq. D-1 to mesh cell face S_N yields:

$$[J_{y,SN}] = [A_{SN}]^{-1}[\phi_{SN}] \tag{D-4}$$

Thus,

$$\int_{S_N}[J_{y,SN}]ds = \int_{S_N}[A_{SN}]^{-1}[\phi_{SN}]ds = [A_{SN}]^{-1}[\phi_{SN}]S_1 \tag{D-5}$$

where S_1 is the area of the face S_N.

Introducing expressions given by Eqs. D-3 and D-5 into Eq. D-2, the balance equation about mesh cell C_1 becomes:

$$[A_{SN}]^{-1}[\phi_{SN}]S_1 - \int_{S_S}[J_{y,SS}]ds + \int_{S_E}[J_{x,SE}]ds - \int_{S_W}[J_{x,SW}]ds$$

$$+ \int_{S_T}[J_{z,ST}]ds - \int_{S_B}[J_{z,SB}]ds + \int_{v_1}[M(\underline{r})][\phi(\underline{r})]dv = [0] \tag{D-6}$$

Integration of the multigroup neutron diffusion equation over mesh cell C_2 yields:

$$\int_{v_2}\underline{\nabla}\cdot[\underline{J}(\underline{r})]dv + \int_{v_2}[M(\underline{r})][\phi(\underline{r})]dv = [0] \tag{D-7}$$

where v_2 is the cell volume.

Application of the Gauss theorem to the first term of Eq. D-7 gives:

$$\int_{S_N'}[J_{y,SN'}]ds + \int_{S_E'}[J_{x,SE'}]ds - \int_{S_W'}[J_{x,SW'}]ds + \int_{S_T'}[J_{z,ST'}]ds$$

$$- \int_{S_B'}[J_{z,SB'}]ds + \int_{S_E}[J_{x,SE}]ds - \int_{S_W}[J_{x,SW}]ds$$

$$- \int_{S_S}[J_{y,SS}]ds + \int_{S_T}[J_{z,ST}]ds - \int_{S_B}[J_{z,SB}]ds$$

$$+ \int_{v_1}[M(\underline{r})][\phi(\underline{r})]dv + \int_{v_1'}[M^*(\underline{r})][\phi(\underline{r})]dv = [0] \tag{D-8}$$

where S_N', S_E', S_W', S_T', S_B' are the mesh cell surfaces within the extra computational node. See Fig. D-2. v_1' is the mesh cell volume within this extra node. Application of Fick's Law to the first 5 terms of Eq. D-8 yields:

$$\int_{S_N'}[J_{y,SN'}]ds = -\int_{S_N'}[D^*(\underline{r})]\left.\frac{d[\phi(\underline{r})]}{dy}\right|_{S_N'} ds$$

$$\int_{S_E'}[J_{x,SE'}]ds = -\int_{S_E'}[D^*(\underline{r})]\left.\frac{d[\phi(\underline{r})]}{dx}\right|_{S_E'} ds$$

$$\int_{S_W'}[J_{x,SW'}]ds = -\int_{S_W'}[D^*(\underline{r})]\left.\frac{d[\phi(\underline{r})]}{dx}\right|_{S_W'} ds$$

$$\int_{S_T'}[J_{z,ST'}]ds = -\int_{S_T'}[D^*(\underline{r})]\left.\frac{d[\phi(\underline{r})]}{dz}\right|_{S_T'} ds$$

$$\int_{S_B'}[J_{z,SB'}]ds = -\int_{S_B'}[D^*(\underline{r})]\left.\frac{d[\phi(\underline{r})]}{dz}\right|_{S_B'} ds$$

By arbitrarily taking $[D^*(\underline{r})] = [0]$, Eq. D-8 simplifies to:

$$\int_{S_E}[J_{x,SE}]ds - \int_{S_W}[J_{x,SW}]ds - \int_{S_S}[J_{y,SS}]ds + \int_{S_T}[J_{z,ST}]ds$$

$$- \int_{S_B}[J_{z,SB}]ds + \int_{v_1}[M(\underline{r})][\phi(\underline{r})]dv + \int_{v_1'}[M^*(\underline{r})][\phi(\underline{r})]dv = [0] \qquad \text{(D-9)}$$

In order for Eq. D-9 to be equivalent to Eq. D-6, it is required that

$$[A_{SN}]^{-1}[\phi_{SN}]S_1 = \int_{v_1'}[M^*(\underline{r})][\phi(\underline{r})]\,dv$$

or

$$[A_{SN}]^{-1}[\phi_{SN}]S_1 = [\bar{M}^*][\phi_{SN}]S_1 \cdot \frac{h}{2} \qquad \text{(D-10)}$$

where

$$[\bar{M}^*] = \frac{1}{V_1'} \int_{V_1'} [M^*(\underline{r})]\, dv$$

and

V_1' is the mesh cell volume within the extra computational node.

$$V_1' = S_1 \cdot \frac{h}{2}$$

where h is the length of this extra node. Equation D-10 simplifies to:

$$[\bar{M}^*] = \frac{2}{h} [A_{SN}]^{-1}$$

Thus the nuclear composition, C^*, of this extra node is given by:

$$[D^*(\underline{r})] = [0]$$

$$[\bar{M}^*] = \frac{2}{h} [A_{SN}]^{-1} \qquad \text{(D-11)}$$

Application of the conditions given in Eq. D-11 to a two-group model with no up-scattering and $\alpha_{12} = 0$ gives

$$\begin{bmatrix} \Sigma_1^* - \frac{1}{\lambda}\nu\Sigma_{f1}^* & -\frac{1}{\lambda}\nu\Sigma_{f2}^* \\ -\Sigma_{21}^* & \Sigma \end{bmatrix} = \frac{2}{h \cdot \alpha_{11} \cdot \alpha_{22}} \begin{bmatrix} \alpha_{22} & 0 \\ -\alpha_{21} & \alpha_{11} \end{bmatrix} \qquad \text{(D-12)}$$

By arbitrarily making

$$\Sigma_{f1}^* = \Sigma_{f2}^* = 0$$

then, Eq. D-12 yields the following relations:

$$\Sigma_1^* = \frac{2\alpha_{11}}{h}$$

$$\Sigma_{21}^* = \frac{2\alpha_{21}}{h\alpha_{11}\alpha_{22}}$$

$$\Sigma_2^* = \frac{2}{h\alpha_{22}}$$

Thus, the nuclear composition, C^*, for this extra node which is equivalent to an albedo boundary condition at the reactor surface S_N is:

$$\begin{aligned} D_1^* &= 0 \\ D_2^* &= 0 \\ \Sigma_{f1}^* &= 0 \\ \Sigma_{f2}^* &= 0 \\ \Sigma_1^* &= \frac{2\alpha_{11}}{h} \\ \Sigma_{21}^* &= \frac{2\alpha_{21}}{h\alpha_{11}\alpha_{22}} \\ \Sigma_2^* &= \frac{2}{h\alpha_{22}} \end{aligned} \qquad \text{(D-13)}$$

The relations given by Eq. D-11 are also valid if the neutron balance is applied along node lines. This scheme permits the use of albedo boundary conditions for the code PDQ-7,[9] which ordinarily allows only zero flux and zero current conditions.

D.3 Zero Current Boundary Condition

This boundary condition is a particular case of the albedo boundary condition. In this case,

$$[J_{u,s}] = [0] ,$$

the condition is equivalent to setting $[A_s]^{-1}$, appearing in Eq. D-1, to zero. When this is done, Eq. D-11 becomes:

$$[D^*(\underline{r})] = [0]$$

$$[\bar{M}^*] = [0]$$

Thus, the fictitious nuclear composition, C^*, for the extra computational node should have all its cross sections and diffusion constants set equal to zero if a zero-current boundary condition is desired.

Appendix E

DESCRIPTION OF PWR BENCHMARK PROBLEMS

E.1 Introduction

This appendix contains a description of the PWR benchmark problems used for testing the fine-mesh flux reconstruction scheme derived in this thesis.

Section E.2 describes the geometry of the fuel assembly used for all the test problems. Section E.3 contains the nuclear cross sections for the different reactor materials. Section E.4 describes the two-dimensional EPRI-9 and EPRI-9R benchmark problems. Finally, Section E.5 presents the three-dimensional EPRI-9 benchmark problem with control rods partially inserted.

E.2 Assembly Geometry

All PWR benchmark problems considered in this thesis use the same assembly type. The radial section of this assembly is shown in Fig. E-1.

Each assembly (21.0 × 21.0 cm) consists of a 15 × 15 array of homogenized cells (1.4 cm × 1.4 cm). The assembly heterogeneities, control rods or water holes, are indicated in Fig. E-1 by a darkened cell. If an assembly is unrodded, then all the darkened cells contain water. If an assembly is rodded, then all darkened cells contain control rod material.

E.3 Nuclear Composition

The heterogeneous, two-group cross section values for the different materials used in the benchmark problems are given in Table E-1.

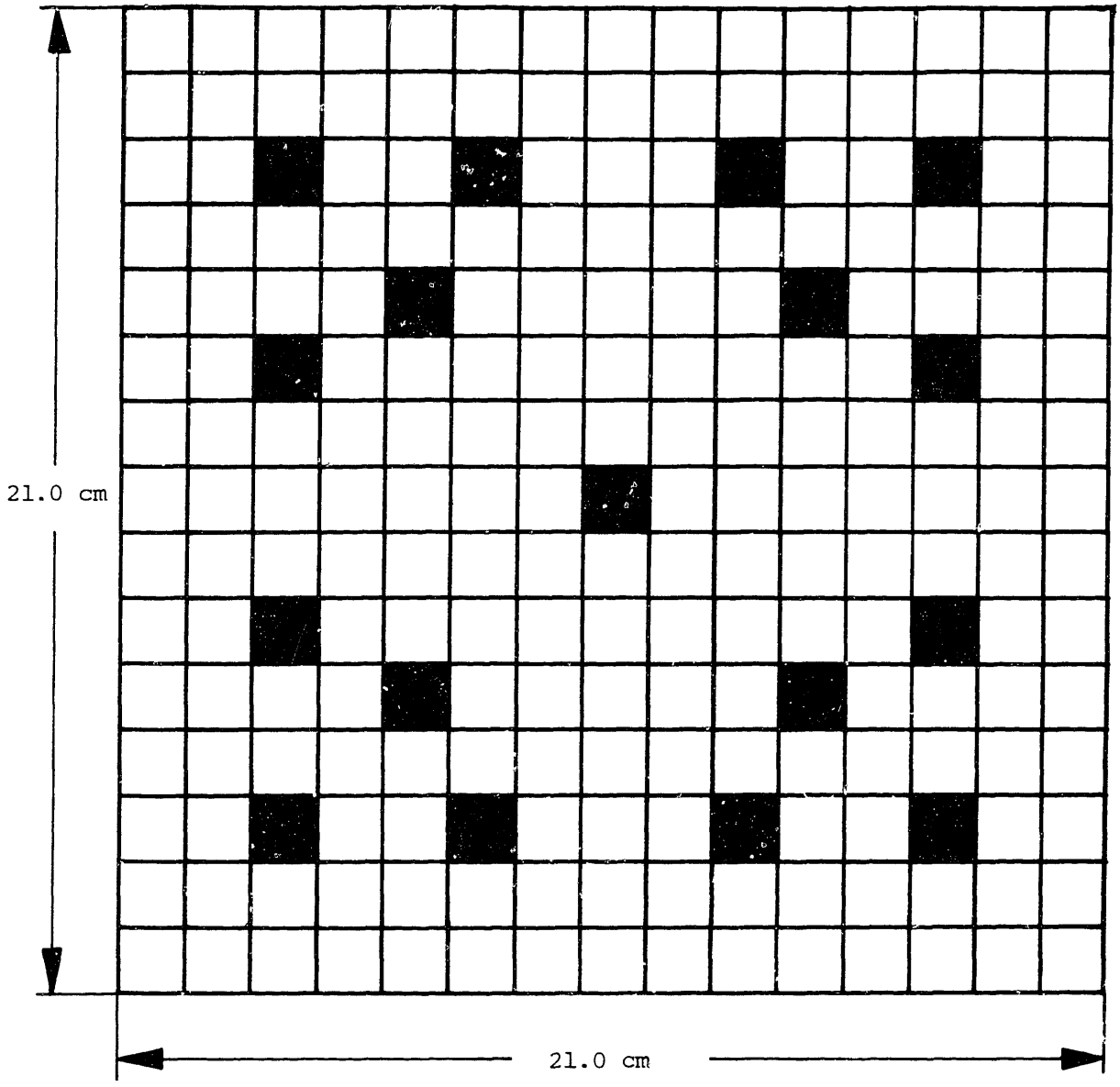

Fig. E-1. Radial section of fuel assembly. Assembly heterogeneities are indicated by darkened cells.

Table E-1. Heterogeneous, two-group cross sections.

Material	Group	D_g (cm)	Σ_{ag} (cm^{-1})	$\Sigma_{gg'}$ (cm^{-1})	$\nu\Sigma_{fg}$ (cm^{-1})
Fuel-1	1	1.500	0.0130	0.0200	0.0065
(F-1)	2	0.400	0.1800	0.0	0.2400
Fuel-2	1	1.500	0.0100	0.0200	0.0050
(F-2)	2	0.400	0.1500	0.0	0.1800
Water	1	1.700	0.0010	0.0350	0.0
(W)	2	0.350	0.0500	0.0	0.0
Baffle	1	1.020	0.0032	0.0	0.0
(B)	2	0.335	0.1460	0.0	0.0
C. Rod	1	1.113	0.0800	0.0038	0.0
(CR)	2	0.184	0.9600	0.0	0.0
Fake	1	0.0	0.3611	0.1337	0.0
Material	2	0.0	0.2646	0.0	0.0

E.4 The EPRI-9 and EPRI-9R Benchmark Problems

The EPRI-9 and EPRI-9R problems consist of 8 fuel assemblies separated from the water reflector by a baffle. The core configuration for the two problems, shown in Figs. E-2 and E-3, is identical except for the rodded cluster in the EPRI-9R reactor.

E.5 The Three-Dimensional EPRI-9 Benchmark Problem with Control Rods Partially Inserted

The radial and axial sections of the three-dimensional EPRI-9 problem, 3D-EPRI-9, are shown in Fig. E-4. The radial grid used to obtain the reference PDQ-7 solution was a uniform square fine-mesh grid with 1.4 cm mesh spacing. The axial mesh grid for the reference PDQ-7 solution is shown in Table E-2.

Albedo boundary conditions equivalent to an infinite water reflector were applied for the top and bottom reactor axial surfaces. The albedo matrix was calculated by applying the analytical formulas appearing in Ref. 8; thus, the matrix elements are

$$\alpha_{11} = \frac{1}{\sqrt{D_1 \Sigma_1}} = 4.042$$

$$\alpha_{22} \quad \frac{1}{\sqrt{D_2 \Sigma_2}} = 7.559$$

$$\alpha_{21} = \frac{\Sigma_{21}}{D_1 \Sigma_2 - D_2 \Sigma_1} = 2.043$$

$$\alpha_{12} = 0.0$$

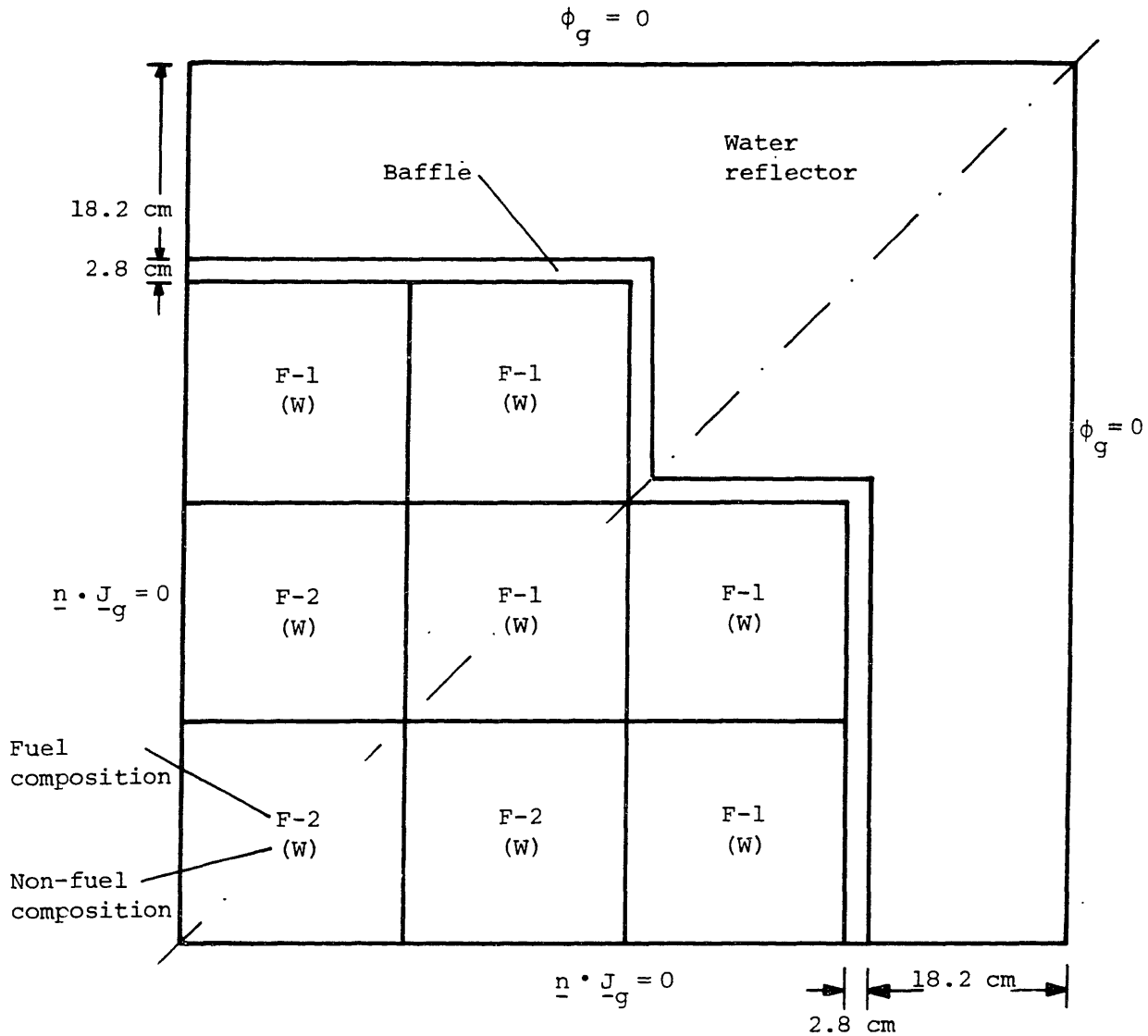

Fig. E-2. Geometry for the EPRI-9 benchmark problem.

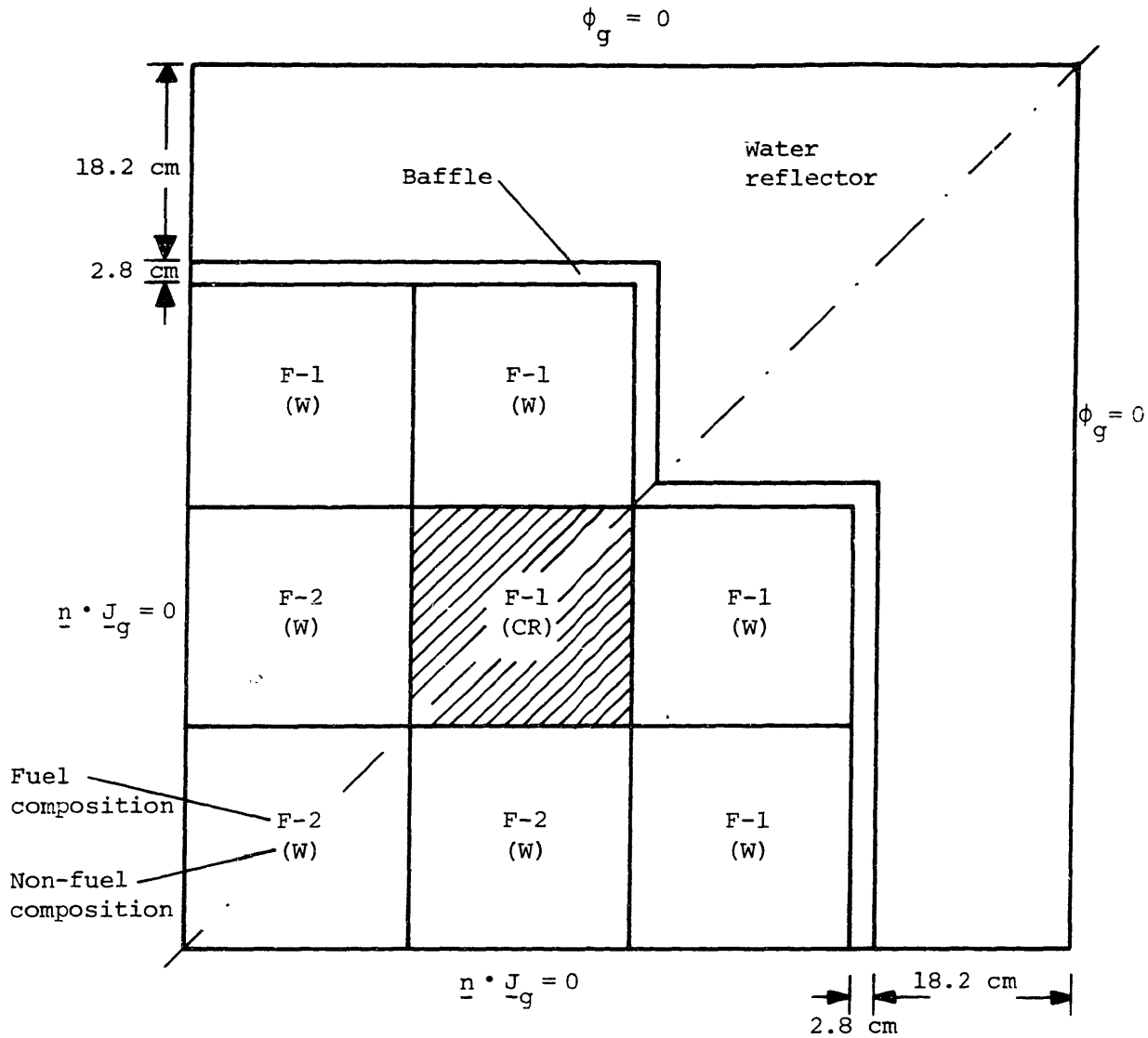

Fig. E-3. Geometry for the EPRI-9R benchmark problem. Shadowed node indicates control rod cluster.

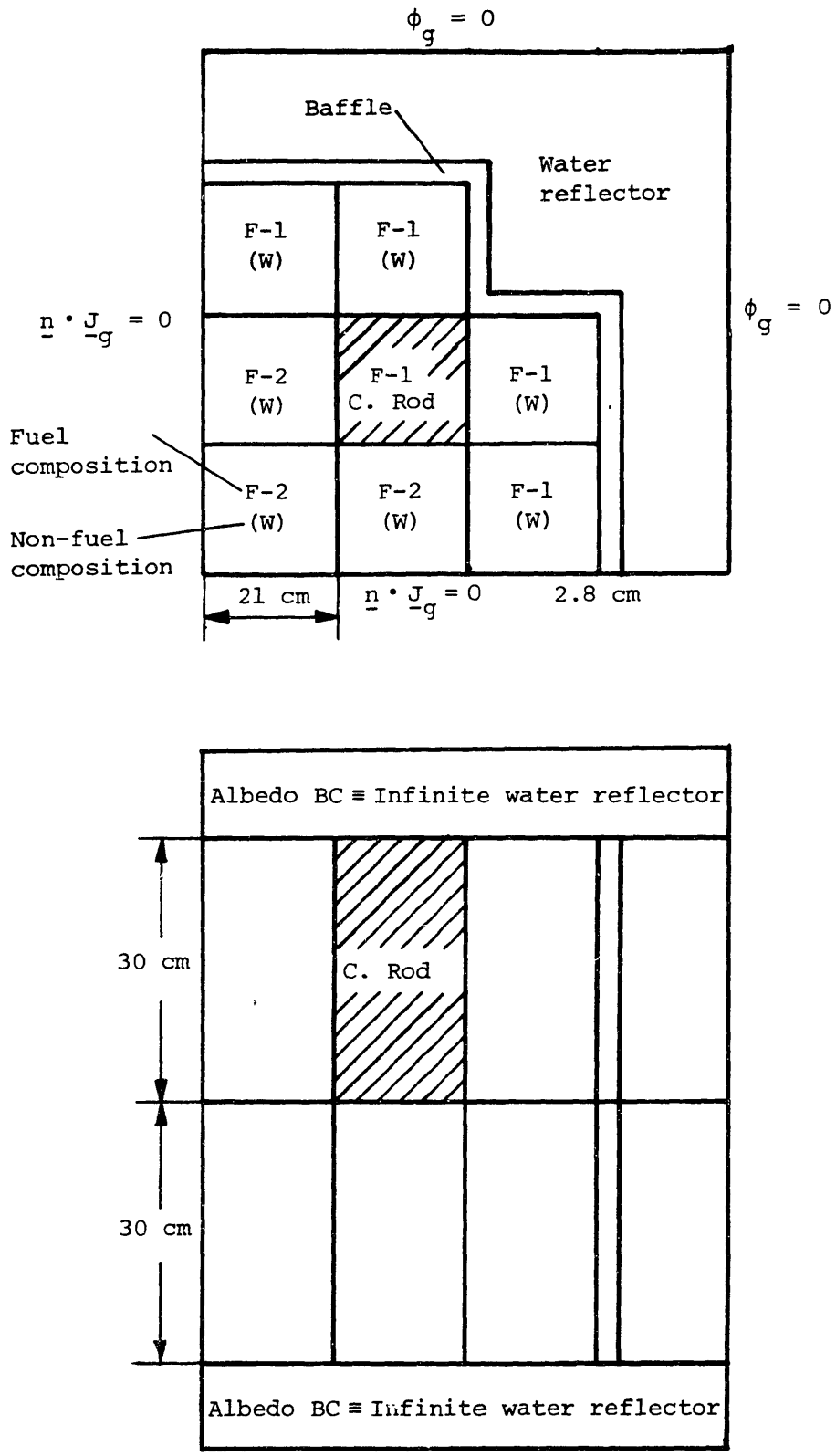

Fig. E-4. Geometry for the three-dimensional EPRI-9 benchmark problem. Shadowed area indicates control rod cluster.

Table E-2. Axial mesh layout used to obtain the reference PDQ solution of the 3D-EPRI-9 benchmark problem.

Total Length	Axial Int.		Mesh Spacings Number × Length	Plane #
60.7				34
60.0		Fake Material	1 × 0.7	33
			2 × 0.5	
58.0			1 × 1.0	30
			5 × 2.0	
45.0			1 × 3.0	24
			1 × 3.0	
			1 × 4.0	
			3 × 2.0	
30.0		Unrodded Region	2 × 1.0	17
		Rodded Region	2 × 1.0	
			3 × 2.0	
			1 × 4.0	
15.0			1 × 3.0	10
			1 × 3.0	
			5 × 2.0	
2.0				
			1 × 1.0	4
0.0			2 × 0.5	1
-0.7		Fake Material	1 × 0.7	0

In order to accommodate this albedo boundary condition in the PDQ-7 code, the scheme described in Appendix D was applied. Thus, an extra computational node, of axial width 0.7 cm, was considered beyond the physical limit of the reactor (see Table E-2). The nuclear composition of the fake material within this node was calculated using Eq. D-13; it is given in Table E-1.

Appendix F

RECONSTRUCTION OF POINTWISE AVERAGE POWERS ALONG AXIAL MESH LINES INSIDE CONTROL RODS PARTIALLY INSERTED

The reconstructed fine-mesh power, $f_{\ell,m}^{i,j,k+1}(z)$ along axial mesh line T, at radial mesh point (ℓ,m) inside node $(i,j,k+1)$, can be calculated from the reconstructed fine-mesh flux for node $(i,j,k+1)$. The reconstructed power therefore has a quadratic shape along line T that obeys the following equation:

$$f_{\ell,m}^{i,j,k+1}(z) = \left\{P_5^{k+1}\left[z^2 - \left(\frac{h_z^{k+1}}{2}\right)^2\right] - \frac{z}{h_z^{k+1}} + 0.5\right\} f_{\ell,m}^{i,j,k+1}\left(\frac{-h_z^{k+1}}{2}\right)$$

$$+ \left\{Q_5^{k+1}\left[z^2 - \left(\frac{h_z^{k+1}}{2}\right)^2\right] + \frac{z}{h_z^{k+1}} + 0.5\right\} f_{\ell,m}^{i,j,k+1}\left(\frac{h_z^{k+1}}{2}\right)$$

$$+ \frac{\left[z^2 - \left(\frac{h_z^{k+1}}{2}\right)^2\right]}{\int_{-h_z^{k+1}/2}^{h_z^{k+1}/2}\left[z^2 - \left(\frac{h_z^{k+1}}{2}\right)\right] dz} \bar{f}_{\ell,m}^{i,j,k+1} \qquad \text{(F-1)}$$

where

$$P_5^{k+1} \equiv \frac{\int_{-h_z^{k+1}/2}^{h_z^{k+1}/2}\left[z - \frac{h_z^{k+1}}{2}\right] dz}{h_z^{k+1}\int_{-h_z^{k+1}/2}^{h_z^{k+1}/2}\left[z^2 - \left(\frac{h_z^{k+1}}{2}\right)^2\right] dz}$$

$$Q_5^{k+1} \equiv \frac{\int_{-h_z^{k+1}/2}^{h_z^{k+1}/2} \left[z + \frac{h_z^{k+1}}{2} \right] dz}{h_z^{k+1} \int_{-h_z^{k+1}/2}^{h_z^{k+1}/2} \left[z^2 - \left(\frac{h_z^{k+1}}{2} \right)^2 \right] dz}$$

and

z ≡ axial coordinate of a generic mesh point on the axial mesh line T, with respect to a Cartesian coordinate system with its origin at the node center,

$f_{\ell,m}^{i,j,k+1}(z)$ ≡ pointwise average power along axial mesh line T,

h_z^{k+1} ≡ length of axial mesh line T (i.e., length of node (i,j,k+1) in the Z direction),

$\bar{f}_{\ell,m}^{i,j,k+1}$ ≡ axial mesh line average power.

Since all integrations are performed numerically, $\bar{f}_{\ell,m}^{i,j,k+1}$ can be written as:

$$\bar{f}_{\ell,m}^{i,j,k+1} = \frac{1}{h_z^{k+1}} \sum_{\alpha=1}^{n} f_{\ell,m}^{i,j,k+1}(z_\alpha) \, \Delta_\alpha \qquad \text{(F-2)}$$

where

α is a dummy index referring to mesh points on mesh line T,

Δ_α is the mesh cell interval associated with mesh point x_α on mesh line T.

Similarly, the reconstructed fine-mesh power, $f_{\ell,m}^{i,j,k}(z)$ along axial mesh line B, at radial mesh point (ℓ,m) inside node (i,j,k), can be calculated from the reconstructed fine-mesh flux for node (i,j,k) and therefore also has a quadratic shape along line B that can be expressed

by an equation similar to Eq. F-1.

Axial mesh lines T and B intersect at mesh point C. Point C, of radial coordinates (ℓ,m), is located at the node face common to nodes (i,j,k) and $(i,j,k+1)$. If node $(i,j,k+1)$ is part of a control rod and node (i,j,k) is not (or vice versa), two different values for the power at point C are available, since, in general

$$f_{\ell,m}^{i,j,k+1}\left(\frac{-h_z^{k+1}}{2}\right) \neq f_{\ell,m}^{i,j,k}\left(\frac{h_z^{k}}{2}\right)$$

This fact is a consequence of the assembly function being discontinuous in the z direction at the control rod radial surface

$$\psi^{i,j,k+1}(x,y) \neq \psi^{i,j,k}(x,y)$$

and thus, in general

$$\psi_{\ell,m}^{i,j,k+1} \neq \psi_{\ell,m}^{i,j,k}$$

A unique value for the pointwise average power at point C can be defined as the arithmetic average of the pointwise powers at point C corresponding to axial mesh lines T and B:

$$f_C \equiv \frac{f_{\ell,m}^{i,j,k+1}\left(-\frac{h_z^{k+1}}{2}\right) + f_{\ell,m}^{i,j,k}\left(\frac{h_z^{k}}{2}\right)}{2}$$

The new axial mesh line averaged power, $\bar{g}_{\ell,m}^{i,j,k+1}$, for line T, then, is found by replacing the pointwise average power $f_{\ell,m}^{i,j,k}(z_1)$, in the first term of Eq. F-2, by f_C. The new mesh line averaged power, $\bar{g}_{\ell,m}^{i,j,k+1}$, can be written in terms of the old line averaged power, $\bar{f}_{\ell,m}^{i,j,k+1}$, as:

$$\bar{g}^{i,j,k+1}_{\ell,m} = \bar{f}^{i,j,k+1}_{\ell,m} + \frac{1}{h_z^{k+1}} [f_C - f^{i,j,k+1}_{\ell,m}(z_1)]\Delta_1 \qquad \text{(F-3)}$$

where in this notation $z_1 = -h_z^{k+1}/2$ and Δ_1 is one half of the distance between mesh points z_1 and z_2.

Note that when the fine-mesh power $f^{i,j,k+1}_{\ell,m}(z_1)$ is replaced by f_C, the fine-mesh powers $\{f_C, f^{i,j,k+1}_{\ell,m}(z_2), f^{i,j,k+1}_{\ell,m}(z_3), \ldots, f^{i,j,k+1}_{\ell,m}(z_n)\}$ no longer fit a quadratic polynomial function, since, although the point-powers $f^{i,j,k+1}_{\ell,m}(z_\alpha)$, $(\alpha = 2,n)$ fit the quadratic function defined by Eq. F-1, f_C does not.

In order to be consistent with the overall reconstruction scheme, new pointwise average powers, $g^{i,j,k+1}_{\ell,m}$, can be obtained, for axial mesh line T, that have a quadratic shape, and that reproduce the pointwise average powers, f_C and $f^{i,j,k+1}_{\ell,m}(h_z^{k+1}/2)$, at the end points of the axial mesh line, and the mesh line averaged power $\bar{g}^{i,j,k+1}_{\ell,m}$ (defined by Eq. F-3). The function, $g^{i,j,k+1}_{\ell,m}$, that satisfies the conditions mentioned above, is given by the following equation:

$$g^{i,j,k+1}_{\ell,m}(z) = \left\{P_5^{k+1}\left[z^2 - \left(\frac{h_z^{k+1}}{2}\right)^2\right] - \frac{z}{h_z^{k+1}} + 0.5\right\} f_C$$

$$+ \left\{Q_5^{k+1}\left[z^2 - \left(\frac{h_z^{k+1}}{2}\right)^2\right] + \frac{z}{h_z^{k+1}} + 0.5\right\} f^{i,j,k+1}_{\ell,m}\left(\frac{h_z^{k+1}}{2}\right)$$

$$+ \frac{\left[z^2 - \left(\frac{h_z^{k+1}}{2}\right)^2\right]}{\int_{-h_z^{k+1}/2}^{h_z^{k+1}/2} \left[z^2 - \left(\frac{h_z^{k+1}}{2}\right)\right] dz} \bar{g}^{i,j,k+1}_{\ell,m} \qquad \text{(F-4)}$$

A similar equation can be obtained for axial mesh line B. Note that

$$g^{i,j,k+1}_{\ell,m}\left(-\frac{h_z^{k+1}}{2}\right) = g^{i,j,k}_{\ell,m}\left(\frac{h_z^{k}}{2}\right) = f_C$$

It is important to notice that Eq. F-4 is a generalization of Eq. F-1, since when the assembly function $\psi^{i,j,k}(x,y)$ is continuous in the Z direction at radial node faces,

$$f_C = f^{i,j,k+1}_{\ell,m}\left(-\frac{h_z^{k+1}}{2}\right)$$

and

$$\bar{g}^{i,j,k+1}_{\ell,m} = \bar{f}^{i,j,k+1}_{\ell,m}$$

Thus, Eqs. F-1 and F-4 become identical.